Damage Tolerance and Arrest Characteristics
of Pressurized Graphite/Epoxy Tape Cylinders

by

Claudia Ute Ranniger

B. S., Aeronautics and Astronautics
Massachusetts Institute of Technology
(1989)

Submitted to the Department of Aeronautics and Astronautics
in Partial Fulfillment of the Requirements for the Degree of

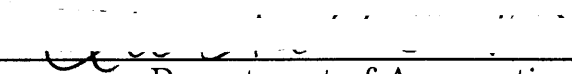MASTER OF SCIENCE

in

AERONAUTICS AND ASTRONAUTICS

at the

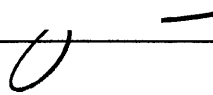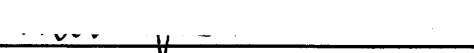MASSACHUSETTS INSTITUTE OF TECHNOLOGY
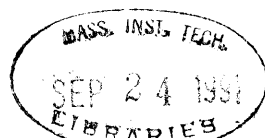
September 1991

Signature of Author _____
Department of Aeronautics and Astronautics
June 18, 1991

Certified by _____
Prof. Paul A. Lagace
Thesis Supervisor

Accepted by _____
Prof. Harold Y. Wachman
Chairman, Departmental Graduate Committee

Damage Tolerance and Arrest Characteristics of Pressurized Graphite/Epoxy Tape Cylinders

by

Claudia Ute Ranniger

Submitted to the Department of Aeronautics and Astronautics on June 19, 1991 in partial fulfillment of the requirements for the Degree of Master of Science.

ABSTRACT

An investigation of the damage tolerance and arrest characteristics of internally-pressurized graphite/epoxy tape cylinders with axial notches was conducted. The extension of an existing failure prediction methodology, developed for quasi-isotropic graphite/epoxy fabric cylinders, to quasi-isotropic and structurally anisotropic tape cylinders was investigated. The effect of external circumferential stiffening bands on the direction of fracture path propagation in structurally anisotropic tape cylinders was also examined. Quasi-isotropic $[90/0/\pm45]_S$ and structurally anisotropic $[\pm45/0]_S$ and $[\pm45/90]_S$ coupons and cylinders were constructed from AS4/3501-6 graphite/epoxy tape. Notched and unnotched coupons were tested in tension to determine the laminate properties. The Mar-Lin equation was used to correlate the fracture stresses of the transversely-slit coupons. Isotropic and specially orthotropic cylinder failure pressure predictions were formulated by applying geometry-dependent stress intensification factors to the coupon stress correlations. Graphite/epoxy cylinders 305 mm in diameter were slit axially and pressurized to failure under two-to-one biaxial loading. Experimental failure pressures of the $[90/0/\pm45]_S$ cylinders agreed with predicted values for all but the specimen with the smallest slit. However, the fracture mode of the cylinder with the 12.7 mm slit indicates that delamination and axial splitting of the 0° ply around the slit may mitigate stresses at the notch tip, resulting in a higher than expected failure load. Failure pressures of structurally anisotropic cylinders were above the values found by isotropic and specially orthotropic shell predictions, and failure pressures for cylinders with 12.7 mm slits were higher than comparable coupon data as well. Possible factors neglected by the predictive methodology include structural coupling in the laminates and axial loading of the cylindrical specimens. Furthermore, applicability of the predictive methodology depends on similarity of initial fracture modes in coupons and cylinders of the same laminate type. Examination of specimen damage indicates that cylinder fracture modes are different from coupon fracture modes in all structurally anisotropic specimens and in the quasi-isotropic tape cylinder with the 12.7 mm slit. Comparison of $[\pm45/0]_S$ and $[\pm45/90]_S$ cylinders with and without stiffening bands shows that stiffeners redirect fracture propagation to the circumferential direction, and can contain damage in the center section of the cylinder away from the endcaps. A quantitative assessment of stiffener effectiveness in containing fracture, based on cylinder radius, slit size, and bending stiffnesses of the laminates is proposed.

Thesis Supervisor: Paul A. Lagace

Title: Associate Professor, Department of Aeronautics and Astronautics, Massachusetts Institute of Technology

Acknowledgements

Although the name on the title page is mine, the final product is the sum of many people's contributions.

Thanks to my family, without whom I would not have come to M.I.T. Thanks, Mom, for caring. Many thanks to Anke as well, for making sure that her little sister was still alive every now and then.

Thanks to Juan R. Cruz, who told me what a composite was in the first place. What else is there to do at 3 AM when you're frantically laying up wing spars and listening to the Beatles? Thank you, Juan, for teaching me the how-to's of making tubes.

Thanks to everyone on the Daedalus team, who taught me how to work with my hands. Thanks to you folks for teaching me that if I really need a widget, I can probably figure out how to make it. What I gained from working with you is immeasurable.

Many thanks to all my fellow graduate students, who have always been ready with encouragement and cheers. Special thanks to Adam Sawicki for pointing out potential pitfalls before the big tubes got me. Thanks to Narendra Bhat, for telling me to get to work, and to Wilson Tsang, for answering all my questions. Thanks to Reese Guy and Mary Mahler for showing me that good women engineers do exist. Thanks to Ed Wolf for reminding me when the next chemistry test was coming up, and thanks to James Williamson for hounding me to finish already. I softened him up for you, James. Many thanks to my classmate Randy Notestine, whose academic fearlessness I admire. I still owe you $6, Randy; I'm just waiting until you least expect it.

Thanks as well to all the UROPpers who have helped me over the years. Thanks to Chantal, Arvind, and Simone for putting up with me even after I asked them to clean yet another set of endcaps. Special thanks go to Kerry Forbes, who has worked with me throughout the last two years. I'm grateful, Kerry, that you didn't put graphite splinters in my bed after I asked you to clean the blast chamber for the sixteenth time. Thanks as well for knowing that the only cure for that glazed look in my eye was yet another diet coke. After today, I'm quitting. Thanks, Matt, for the cookies when I needed them most.

Thanks to Al Supple for everything he has done. Without him, I'd still be trying to run the autoclave. Thank you, Al, for trusting all my harebrained schemes and finding all the thingamajiggies I needed. Thanks for successfully hiding your panic when I dumped all the (former) blast chamber electronics on your desk. Thanks most of all for telling me the things I needed to know, and for caring about my future.

The transformation of my graduate work into the thesis presented here is due mainly to the efforts of my advisor. Many thanks go to Paul Lagace for helping me to present a coherent and meaningful piece of work. Thanks also for giving me the chance to study here. Great M&M's, Pawl Lagaaasie -- thanks, Clawdierrr.

Thanks go to Michael Graves, for all of his invaluable information. Thank you for discussing problems and giving me ideas with which to work. Your concern about this work is greatly appreciated.

Most of all, I want to thank Craig Wanke, who has provided endless amounts of moral support in the past five years. He always believed that I was going to make it, even when I wasn't so sure myself. Thanks, love, for the votes of confidence.

Foreword

Table of Contents

List of Figures

<u>FIGURE</u>   <u>PAGE</u>

List of Tables

Nomenclature

a	Half-slit length
a_o	Characteristic length for use in the Whitney-Nuismer Average Stress Criterion
C	Containment ratio
d_o	Characteristic length for use in the Whitney-Nuismer Point Stress Criterion
D_s	Circumferential bending stiffness of stiffened region of cylinder
D_u	Circumferential bending stiffness of cylinder base laminate
E_L	Longitudinal modulus
E_T	Transverse modulus
H_c	Composite fracture parameter
K_i	Stress intensification factor for an isotropic shell containing a slit
K_{Ic}	Critical stress intensity factor
K_o	Stress intensification factor for an orthotropic shell containing a slit
m	Value of the stress singularity at a notch tip in a bimaterial interface, and parameter in the Mar-Lin equation
p	Far-field stress in notched coupon, expressed in terms of applied internal cylinder pressure
p_{cyl}	Internal cylinder pressure
r	Cylinder radius
t	Laminate thickness
d	Orthotropy parameter for use in orthotropic shell parameter
λ_i	Isotropic shell parameter
λ_o	Orthotropic shell parameter

ν Poisson's ratio

ν_{LT} Major Poisson's ratio

ν_{TL} Minor Poisson's ratio

σ_{cyl} Circumferential far-field stress in a cylinder

σ_f Far-field fracture stress of notched coupon

σ_o Unnotched coupon fracture stress

ζ Nondimensionalized notch length for use in the Whitney-Nuismer Stress Criterion

CHAPTER 1

Introduction

The use of graphite/epoxy as a structural material has increased for a number of reasons including the material's great versatility. As the number of applications grow, the demand for a better and more complete understanding of graphite/epoxy structures grows as well. Because knowledge of composite structural behavior is still limited, much of the commercially-oriented work depends on testing to define needed properties. To avoid these time-consuming and costly testing procedures to determine the optimal configuration for any structure, better analytic tools need to be developed to describe a structure's properties. These tools, based on material behavior, require a better understanding of the basic phenomena of damage tolerance and arrest. It is necessary for the expanded use of composite structures, therefore, that the material's behavior be understood so that the proper analytic tools can be developed.

Both the complexity of a structure and the possibility of damage must be considered in the design process. Structures may include cutouts or manufactured notches, and in the course of normal operations, damage may occur. It is important to quantify the resulting structural properties so that behavioral predictions can be developed. Quantification of material properties should include both normal structural behavior as well as damage resistance and tolerance parameters.

One structure of interest to engineers is the internally-pressurized, thin-walled cylinder. Examples of structures of this general shape include airplane fuselages, rocket motor casings, fuel tanks, and oil pipelines.

Each of these structures contains notches which are integral to its function. Fuselages contain cutouts for windows and doors; fuel tanks and oil pipelines contain similar notches for valves or pressure gages. Failure of the cylinder due to internal pressure loading is most likely to occur in these areas. It is important, therefore, that an accurate quantitative measure of the cylinder's behavior include the notches so that failure criteria and predictive methodologies can be developed.

A method to predict the fracture pressure of notched internally-pressurized composite cylinders has been developed [1]. The prediction, based on the assumption that the local stress state near the end of a slit governs fracture, uses notched coupon fracture data and material properties to determine the fracture pressure of cylindrical specimens. While the testing of tensile coupons is a largely routine, low-cost effort, the testing of full-size cylindrical structures is not. By using coupons to predict cylinder failure, much of the preliminary cylinder testing can be replaced with simple coupon tests and analysis. However, this methodology was developed for the case of quasi-isotropic fabric cylinders. It is important to examine the extent to which this methodology is applicable to composite cylinders of general configuration.

In the current work, the fracture of notched pressurized cylinders and the limits of using tensile coupon data to predict the failure pressures are thus investigated. The ability to use notched coupon data to predict cylinder fracture has been demonstrated for a quasi-isotropic $[0_f/45_f]_s$ fabric layup[1] [1-7]. In the current investigation, the applicability of this fracture prediction methodology to quasi-isotropic and structurally anisotropic

---

[1]the subscript f indicates a fabric ply

AS4/3501-6 graphite/epoxy tape cylinders is examined by experimentally finding the fracture pressures and modes of such specimens. Cylinder fracture data, including failure pressures and studies of fracture paths, is used to aid in determining fracture mechanisms and the applicability of the predictive methodology to these cylinders.

Implementation of the experimental work includes coupon and cylinder tests. The notch sensitivity of tensile coupons with slits is determined experimentally, and the results are used to predict the fracture of cylinders with through-the-thickness axial slits. Axially-slit cylinders are subsequently pressurized to failure, and the results compared with the predicted fracture pressures. Both the ability of the methodology to predict fracture and the basic phenomena involved in cylinder fracture are investigated.

Another engineering concern with the fracture of notched graphite/epoxy cylinders is the issue of fracture propagation. As failure occurs, the fracture paths can propagate axially and circumferentially, causing widespread damage to the cylinder. It is desireable to contain the resulting damage in a small region so that overall structural integrity is retained despite local fracture.

One approach to this problem involves the use of stiffening bands. Stiffeners are present in many structures to help carry loads both axially and in hoop directions. The placement and thickness of stiffeners can also be used to isolate the notched regions from the rest of the structure. The increased local stiffnesses and material strength can hinder the propagation of a failed notch through the stiffener, helping to contain failure.

Quantitative evaluations of failure containment for graphite/epoxy notched cylinders with stiffeners have not been made due to the complexity of the problem. It is more simple to evaluate hoop and axial stiffeners separately. Work has been conducted on quasi-isotropic fabric cylinders with circumferential stiffeners. [1, 7] Although the direction of the failure path has been correlated with finite element analysis of the loaded cylinder's strain state, all of the individual parameters governing flaw propagation have not been identified.

The second purpose of this investigation is, thus, to both determine the effects of circumferential stiffening bands on the failure propagation of notches in structurally anisotropic cylinders, and further to identify the parameters governing fracture path redirection. Different stiffener configurations are layed up on the outside of the cylinders, and fracture paths are examined after failure. Qualitative as well as quantitative evaluations of the failure path are made.

Previous work used to pose the questions for this investigation is discussed in Chapter 2 of this report. Discussion includes failure prediction methodologies as well as previous investigations into the use of stiffeners. Experimental procedures for all coupons and cylinders tested in the course of this work are given in Chapter 3. Analytic and experimental results are given in Chapter 4. Further discussion and possible explanations of these results are presented in Chapter 5. Conclusions and recommendations for subsequent investigations are outlined in Chapter 6.

CHAPTER 2

Background

A literature review was conducted to determine current fracture prediction methodologies and fracture path studies for pressurized cylinders. Fracture prediction methodologies were assessed according to three criteria: correlation with experimental data, ease of application, and limitations of the predictive methodology. Fracture path studies including both crack propagation predictions as well as arrest criteria were examined.

2.1 Fracture Prediction Methodologies

The fracture prediction methodologies discussed here may be divided into two categories; those which directly characterize cylinder fracture, and those which extrapolate the cylinder fracture load from flat plate fracture data. While the former approach seems more straightforward conceptually, the latter is, in general, much more easy to implement. The fracture of notched flat plates under tensile loads is investigated as a precursor to the prediction of cylinder fracture. Factors accounting for cylinder curvature and notch geometry are introduced and the development of a fracture prediction based on flat plates is then presented. Finally, a direct method for the prediction of notched cylinder fracture is shown.

2.1.1 Notched Flat Plates in Tension

Various methods have been used to predict and correlate the fracture of notched plates in tension. Failures of notched homogeneous materials can generally be predicted via linear elastic fracture mechanics (LEFM), where the catastrophic fracture of a notched plate under uniaxial tension depends on notch geometry and stress intensity at the notch tip. The far-field fracture stress can be expressed as

$$\sigma_f = K_{Ic}(\pi a)^{-0.5} \qquad (2.1)$$

where K_{Ic} is the fracture toughness of the homogeneous material, a is the half-crack length, and the exponent 0.5 is the stress singularity at a crack tip. Linear elastic fracture mechanics, however, is not sufficient for the fracture prediction of composite materials such as graphite/epoxy, whose fiber and matrix portions do not comprise a homogeneous material, and whose fracture modes are consequently much different. Therefore, new approaches must be considered.

An overview of notched composite laminate analyses and experimental work has been compiled by Awerbach and Madhukar [8]. They found that the two major areas of analytic work are either based on extended linear elastic fracture mechanics concepts, or based on the stress distribution and damage zone 'ahead' of a notch. While the first approach does not incorporate the micro- or macro-mechanical processes involved in laminate fracture, it has been pursued for the purpose of providing simple and straightforward predictive/correlative methods. The second approach, although not including exact stress and damage states around the notch, has been used to quantify the damage ahead of the notch tip in terms of an

effective crack length and approximate stress distributions. Here the mechanical fracture processes of fiber and matrix are considered in the development of fracture prediction methodologies. It should be noted that all fracture prediction methodologies presented in this compendium are semi-empirical, requiring notched and/or unnotched coupon data for correlative purposes.

Three methods for the prediction of notched coupon fracture stresses are presented here. The methods described below were chosen because they are representative of the different approaches to notched coupon fracture prediction/correlation, and because they have been shown to be good correlative models for coupon fracture stresses. The first method presented, developed by Mar and Lin [9], is similar in expression to linear elastic fracture mechanics but includes a factor accounting for the inhomogeneity of the material. The second, proposed by Whitney and Nuismer [10,11], is used to correlate fracture stresses by quantifying the local stress state surrounding the notch tip. The third, developed by Waddoups, Eisenmann and Kaminski [12] and modified by Cruse [13], is used to determine fracture stresses by incorporating an effective crack length, determined from the notch and its surrounding stress state, into linear elastic fracture mechanics.

Mar and Lin describe the fracture stress of a notched coupon under uniaxial tension in a manner analagous to linear elastic fracture mechanics [9]. They proposed that the far-field fracture stress can be expressed in the form

$$\sigma_f = H_c(2a)^{-m} \tag{2.2}$$

where 2a is the length of the notch transverse to the loading direction, H_c is defined as the laminate fracture parameter [14], and m is the value of the stress singularity at a notch tip at the fiber-matrix interface. It should be noted that the fracture stress is not dependent on notch geometry, but only on the length of the notch measured in the direction perpendicular to that in which the tensile load is applied. The composite fracture parameter, H_c, somewhat analagous to the linear elastic fracture mechanics fracture toughness parameter, K_{Ic}, is determined experimentally and has been found to be a function of layup [14,15,16]. The exponent m, which has been determined analytically to be 0.28 for graphite/epoxy, is a function of the shear moduli and Poisson's ratios of the fiber and matrix [17].

The Mar-Lin equation has been found to be a good correlative model for the fracture of composite laminates with through-the-thickness notches [14,15,16,18,19]. Experimental work has indicated that the correlation is applicable to both tape and fabric graphite/epoxy laminates containing holes or slits oriented arbitrarily relative to the loading axes. It has been found that while H_c is laminate and stacking-sequence dependent, it is invariant for different notch geometries. Thus, the fracture parameter, H_c, of a laminate can be determined from a single notch geometry without limiting the applicability of the correlation within that laminate type.

An alternative approach to predicting the fracture of notched composites is similar to the fracture predictions of homogeneous metals based on the plastic behavior at the notch tips. Whitney and Nuismer [10,11] have developed two separate criteria for the fracture of a notched laminate which depend on semi-empirical knowledge of the stress state surrounding the notch. Both criteria are dependent upon prior knowledge

of the unnotched fracture stress as well as the notched behavior of the laminate.

Whitney and Nuismer proposed an average stress criterion in which they predicted that fracture occurs when the stress in the laminate averaged over some length, a_0, from the edge of the notch reaches the unnotched fracture stress of the laminate. The prediction is dependent on the notch geometry. The form for the far-field fracture stress of a laminate with a transverse through-the-thickness slit is

$$\sigma_f = \sigma_0 \left[\frac{1-\zeta}{1+\zeta}\right]^{0.5} \qquad (2.3)$$

where σ_0 is the unnotched fracture stress and ζ is the ratio of slit length $2a$ to the extended slit length $2(a + a_0)$. Both the unnotched fracture stress and the length a_0 are determined experimentally from unnotched and notched coupons respectively. The length a_0 may be physically interpreted as a rough approximation of the distance ahead of the hole in which some damage has already occured.

They also postulated, in the point stress criterion, that fracture occurs when the stress at some distance, d_0, from the notch tip reaches the unnotched fracture stress of the laminate. The fracture stress of the notched specimen again depends on unnotched fracture stress and notch geometry and size. For the stress concentration due to a transverse slit, the far-field fracture stress is

$$\sigma_f = \sigma_0 \left[1-\zeta^2\right]^{0.5} \qquad (2.4)$$

where σ_o is the unnotched strength and ζ is the ratio of the slit length 2a to effective slit length $2(a + d_o)$. The dimension, d_o, analagous to the length of the 'plastic zone' found ahead of a crack in ductile materials, represents the length over which the laminate must be critically stressed for fracture to occur. Both the unnotched strength and the length d_o are determined experimentally to yield a correlation for coupon fracture strengths.

The basis for these fracture prediction methodologies is the assumption that the material can redistribute the local stress concentrations via microcracking and other micromechanical failures. This indicates that both a_o and d_o should be functions of the material and its fiber/matrix interactions alone. Experimental work and the application of these correlations, however, indicates that these crack extension parameters are dependent upon layup as well [11, 14].

A third approach to fracture prediction of notched laminates incorporates an 'effective' crack length into linear elastic fracture mechanics [12, 13]. The effective crack length is a sum of the actual notch length and the length of a region of high stress concentration adjacent to the notch. The length of this high-stress region is analagous to the variable d_o proposed in the point stress criterion, and again depends upon the micromechanical material properties. The far-field fracture stress correlation can be written as in equation 2.1, where the length a is now defined as the 'effective' crack half-length. Again, the values for material fracture toughness and effective crack length must be determined experimentally. It should be noted that this approach approximates the material as homogeneous, and does not explicitly include micromechanical properties of the material.

All three fracture stress prediction methodologies presented herein are semi-empirical. All three are relatively easy to apply, and have been proven to be good correlative models. The Mar-Lin equation is applicable to all notch geometries in a single laminate type, while the methods presented by Whitney-Nuismer require new expressions for each notch and laminate type. The predictive methodologies proposed by Cruse and Waddoups, et al, have been applied only to circular notches.

2.1.2 Stress Intensification Factors for Notched Pressurized Shells

The stress state of a pressurized cylinder with an axial notch is different from that of the flat plates described in the preceding section. This is due not only to the difference in applied loading, but also to the geometry of the problem. The internal pressure, leading to a 2:1 radial to axial state of stress in the cylinder, causes the cylinder to expand in both of these directions. The cylinder also bulges, or deflects outward radially and circumferentially to open the slit, in the local area around the precut slit. These deformations, which result in extensional and bending stresses at the slit ends and edges, as well as the bending-extensional stress coupling introduced by the curved shell geometry, contribute to cylinder fracture.

Folias [20,21,22] used eighth order shell theory to determine the stress field at slit ends in isotropic shells. He utilized stress and displacement equations governing shell behavior to develop closed-form solutions for the stresses due to bending and extension at the slit tip for various specimen geometries and loading conditions. These stress distributions are functions of position relative to the slit as well as bending and extensional stress intensification factors. The stress intensity factors,

depending on shell geometry, slit size, material properties, and applied loading, represent the increase in local stresses at the slit tip in a loaded shell over those found for a similarly-notched plate. The factors account primarily for stress intensifications due to specimen geometry.

For an axial slit in a cylindrical shell loaded via internal pressure, the extensional stress intensification factor, representing the increase in local extensional stresses at the slit tip in a shell, can be approximated as

$$K_i = (1 + 0.317\lambda_i^2)^{0.5} \qquad (2.5)$$

The isotropic shell parameter $\lambda_i 2$ is a function of laminate properties and specimen geometry.

$$\lambda_i^2 = \frac{a^2[12(1 - v^2)]^{0.5}}{rt} \qquad (2.6)$$

where t is the thickness and r the radius of the cylinder, the half-slit length is a, and the Poisson's ratio of the laminate is v. The subscripts i indicate that the stress intensification factor and the shell parameter are derived for isotropic materials. The stress intensification factor for bending, and consequently the components of stress due to local bending at the slit tip, are small compared to the extensional factor and stresses, and are thus neglected. A similar set of equations has been developed for circumferential slits and holes in cylinders under axial tension and biaxial and uniaxial pressure, and for slits in pressurized spherical caps [23,24]. It should be noted that the derived stress state is limited to thin, shallow, isotropic shells only.

Krenk [25] further generalized the equations determined by Folias by using tenth order shell theory to include transverse shear deformation and specially orthotropic materials, which are defined as orthotropic materials whose principal axes coincide with the loading axes. The stresses derived for an axial slit in a cylindrical shell under tension and internal pressure include intensity factors accounting for bending, stretching, stretching-bending coupling, and bending-stretching coupling. As in the isotropic case previously presented, the stress intensity factors are functions of an orthotropic shell parameter λ_o, which can be expressed for a cylindrical specimen as

$$\lambda_o^4 = \frac{a^4[12(1 - v^2)]}{\delta^2 t^2 r^2} \tag{2.7}$$

where the subscript o denotes the special orthotropy of the material. In this equation, a is the half-slit length, r and t are the cylinder radius and thickness, v^2 is the product of the major and minor Poisson's ratios, and the orthotropy parameter δ is defined as

$$\delta^4 = \frac{E_L}{E_T} = \frac{v_{LT}}{v_{TL}} \tag{2.8}$$

where E_L and E_T are the longitudinal and transverse moduli, and v_{LT} and v_{TL} the major and minor Poisson's ratios. Note that the orthotropy of the material is incorporated into the stress intensity factors by expressing both v and δ as functions of both longitudinal and transverse laminate properties. Unfortunately, closed-form solutions for the stresses are not available and consequently stress intensity factors must be determined

numerically for each individual case. Krenk presents numerical results for the stress intensity factors as a function of cylinder radius and thickness. As in the isotropic case, the stress intensification factor due to stretching is dominant.

2.1.3 Pressurized Cylinders

A large amount of analytic and experimental work has been conducted on the failure of notched pressurized cylinders. Rogers [26] used the Mar-Lin equation to correlate the circumferential fracture stresses of $[\pm 45/90]_s$ tape cylinders[2] with axial slits ranging from 6 to 51 mm in length. By using equation 2.1 to determine a best fit to the data, he found values for the fracture parameter H_c and the power m. He was thus able to project a best fit Mar-Lin curve which matched the data quite well. This correlation does not incorporate the stress intensity factors developed for shells, nor does it use the theoretical value for the parameter m. Thus, in this case, m is no longer a function of the material alone, but is also a function of layup and specimen geometry. This severely limits the applicability of the correlation to more general cases.

Graves [1,3] postulated that the local stress state at the end of an axial slit in a biaxially-loaded cylinder could be compared to the stress state in a uniaxial tensile coupon with a similar notch configuration. As previously discussed for the case of a shallow shell under biaxial loading, the extensional stress intensity factor dominates over the bending and coupling terms. By neglecting the bending terms, the pressure loading can be approximated as the biaxial tensile loading of a curved coupon.

---

[2] the 0° ply direction is the hoop direction of the cylinder

However, Graves included only uniaxial tensile specimens in his predictive methodology. The reasons for this are threefold. First, although experimental work investigating the fracture of notched laminates under biaxial tension has been conducted, e.g. [27], the results have not been adequately explained by any proposed fracture prediction methodology. Second, the manufacturing and testing procedures are substantially more complex and time-consuming for biaxial specimens, again limiting the ease with which a fracture prediction methodology of this type could be applied. Third, the notches used in Graves' investigation are all narrow axial slits. The 'length' of the slit perpendicular to the direction of axial loading is very small. It has been shown that the tensile fracture stress of coupons with narrow slits precut parallel to the loading axis is not lower than the unnotched value [1,19]. This indicates that the component of load parallel to a slit of small width may not significantly affect the fracture of a notched cylinder. The problem of the fracture of a cylinder with a narrow axial slit can then be reduced to the uniaxial loading problem where fracture is induced by radial pressure alone. Thus, the use of uniaxial coupon experimental results and fracture prediction methodologies can be justified for this application.

The stress intensity factors presented by Folias and Krenk can be used to account for the stress intensification at the end of a slit due to the geometry of the specimen. Graves therefore postulated that, given the same far-field applied loads, the stress intensity at the notch tip in a cylinder could be approximated as the product of the stress intensity at the notch tip in a plate and the extensional stress intensity factor.

Assuming that both the coupon and cylinder will fail when the local stresses reach some critical value dependent on material and layup, the

fracture stress relation between axially-slit cylinder and notched coupon can be rewritten as a function of far-field stresses:

$$\sigma_{cyl} = \frac{\sigma_f}{K} \qquad (2.7)$$

wher σ_{cyl} is the far-field circumferential stress of a cylinder at fracture, σ_f is the far-field fracture stress in a plate under uniaxial tension, and K is the extensional stress intensification factor. It should be noted that this relationship is limited to axial slits in pressurized cylinders; however, a similar equation relating plate stress to the far-field axial stress in a circumferentially-slitted cylinder can be written as well.

Graves [1,3] used this relation to predict the fracture of quasi-isotropic fabric cylinders with axial slits. Both $[0_f/45_f]_s$ and $[45_f/0_f]_s$ 152 mm radius cylinders containing axial slits were tested. Cylinders were sealed at both ends and pressurized to preset values. A guillotine of specific dimensions was dropped onto the cylinder to make a through-the-thickness cut. Cylinders were resealed and the tests repeated with larger guillotine knives if no catastrophic fracture resulted from the cut. Fracture prediction was conducted using the semi-empirical Mar-Lin curve and the isotropic stress correction factor. The prediction agreed well with all of the experimental data for the slit lengths, which ranged from 38 to 69 mm.

Chang and Mar [2,4] investigated the fracture of $[0_f/45_f]_s$ cylinders with angled slits, holes, and ellipses. Notches ranging in length from 51-102 mm were precut into the cylinders, and both the notch and the cylinder ends were sealed before pressurization. This procedure yields a more exact relation between notch size and fracture pressure than does Graves' fail/no fail data. Fracture pressures were predicted from flat plate data via the

Mar-Lin equation and stress intensification factors developed by Folias for the appropriate notch geometries. The analytic and experimental results correlate well.

Kageyama [28] worked with axially-slit $[0_f/45_f]_s$ cylinders containing implanted delaminations around the slits. Surprisingly, the data compared well with Graves' correction via the Mar-Lin equation, indicating that the implanted delaminations had no effect on the fracture pressure. He hypothesized that the bending stiffness of the delaminated zone was not reduced because the friction between the graphite and the implanted delamination was high when the cylinder was pressurized internally.

Sawicki [7] extended Graves' investigation to include axial slits ranging from 52-178 mm for the $[0_f/45_f]_s$ cylinder configuration. Slits were precut into the 152 mm radius cylinders and a bladder system was used to seal the cylinder prior to pressurization. Again, data and prediction agreed well.

Ranniger [29] investigated the fracture pressure of 76 mm radius cylinders with axial slits. Precut axial slits ranging from 38 to 76 mm in length were cut in $[0_f/45_f]_s$ cylinders, and pressurization was conducted as by Sawicki. Predicted fracture pressures, calculated via the Mar-Lin equation and Folias' isotropic shell correction factor, compared well with the experimental data. The results indicate that the shell correction factor and, therefore, the prediction methodology as well, scale well with cylinder radius. This is important for the application of this methodology to larger cylinders such as aircraft fuselages.

Saeger and Lagace [6] investigated the fracture of graphite/epoxy cylinders with a 'tough', or high strain-to-failure CYCOM 907 resin

system. Axial slits of sizes 51-152 mm were precut into the 152 mm radius cylinders, and the cylinders were tested according to established procedures. The results were adequately correlated via the methodology described above, but the agreement was not as good as that found for the Hercules 3501 resins used in previous research. The point stress criterion described previously was also used to predict fracture pressures. A finite difference routine was developed to calculate values for the deflection and stress functions governing the cylinder behavior at the slit end. The results were used to determine the stresses around the notch tip, which in turn were used to predict the cylinder fracture. The data compared well with the results of this predictive methodology. It should be noted, however, that the finite difference solution is unique not only for each cylinder configuration but for each slit size as well. The application of this method to predict fracture pressures for a series of slit sizes is computationally expensive in comparison to Graves' relation.

Two methodologies to predict fracture pressures of notched cylinders have been presented here. The first utilizes the known fracture stresses of notched coupons under uniaxial tension and calculates the cylinder fracture pressure via stress intensity factors dependent upon specimen geometry. This methodology has been proven effective for cylinders which are made of a homogeneous metal, or of a quasi-isotropic graphite/epoxy fabric laminate. The methodology has been shown to scale well with cylinder and notch size. The second fracture prediction method is laminate and notch specific, and requires significantly more computation. Although predicting the fracture of 'tough' material somewhat more accurately than did the first method, this procedure is more cumbersome to implement.

Previous work has focused mainly on quasi-isotropic fabric laminates with an assortment of damage states and notches. Fracture prediction methodology has provided accurate results and good agreement with experimental data. However, a significant subset of composite laminates have been excluded from these investigations. Little work has been conducted on cylinders made of graphite/epoxy unidirectional tape. No comparisons of fabric and tape cylinders of comparable layups have been conducted to determine the effect of the different materials on cylinder fracture. Almost no work has investigated the fracture of laminated cylinders which are not quasi-isotropic. The effects of structural anisotropy, including laminates which exhibit bending-twist coupling, have not been investigated.

2.2 Fracture Path Studies

There are essentially three stages to the propagation of damage in a pressurized vessel; fracture initiation, damage propagation, and damage arrest. The initiation, or onset, of cylinder fracture due to a notch has been discussed in the previous sections. The studies of damage propagation and arrest are closely related, since it is necessary to know the parameters governing the first to achieve the second.

2.2.1 Damage Propagation

Most damage propagation studies in cylinders which are of interest to this work have used homogeneous metals as the medium of choice. Although the results of these investigations do not necessarily apply to

damage propagation in a composite cylinder, the underlying principles are important.

Emery et al [30] calculated the dynamic behavior of a crack in a pressurized pipe via a finite difference code. They postulated that crack propagation is governed by a maximum stress criterion at the notch tip. Numerical results were obtained for the crack propagation velocities due to different critical stresses and different rates of pressure loss through the notch. Results correlated well with several other predictive methods; however experimental comparisons were not conducted.

McGuire et al [31] extensively studied the axial propagation of cracks in pressurized pipelines. They state that a crack will propagate if the dynamic energy release rate, G, is greater than the energy dissipation requirement of the crack tip. The quantity G, which represents the 'energy made available by the structure to support crack growth,' is a function of the externally applied work, the kinetic and elastic strain energies of the structure, the wall thickness and the crack length. The energy dissipation requirement, a function of material properties and crack propagation speed, represents the amount of energy needed for the crack to grow.

This relation can be used as a tool for the design of pressurized cylinder/stiffener configurations. Given the operating conditions and dimensions of a pressurized pipe, the minimum fracture toughness which will prohibit crack growth in the pipe material can be predicted. If the dimensions and operating conditions of a pipe are known, and if the fracture toughness of the pipe material is less than the minimum required value mentioned above, the crack propagation speed can be estimated. The optimal configuration and material properties of the pipe/stiffener system

which will minimize catastrophic damage due to a notch can then be determined.

Little work has been conducted on damage propagation in graphite/epoxy cylinders or pipelines, since the commercial use of composites for these applications is just beginning. Sawicki [7], however, has shown that the strain in a composite cylinder can be related to the direction of fracture propagation through the specimen. He postulated that fracture will propagate in the direction perpendicular to the orientation of the maximum tensile strain. Finite element models of both $[0_f/45_f]_s$ plates and cylinders with slits were developed to calculate the magnitudes and directions of principal strains in these specimens. Experimental work was conducted on plates and cylinders with several types of stiffening bands to determine the directions of fracture path propagation for different strain states. Results of the finite element models correlated well with experimental data. Both experimental work and the finite element model indicated that the stiffening bands did not alter the direction of maximum strain, or, therefore, the direction of notch propagation in the plates. In the cylinders, however, the addition of stiffening bands was found to reduce circumferential strains due to the bending-stretching coupling inherent to the cylindrical specimens. The reduction of circumferential strain caused a change in the direction of maximum tensile strain, and of the fracture path as well.

2.2.2 Damage Arrest

After the notch in a pressurized cylinder begins to propagate through the material, catastrophic fracture will occur unless the damage is contained, or arrested. It is vital, therefore, to institute measures which

will minimize the distance of notch propagation, and, consequently, the damage caused by the fracture. Jozavi, Dupuis, and Sancaktar [32] state that "the function of a gas pipeline crack arrestor should be: 1) to take load from the cracked pipe, 2) to constrain the opening of crack boundaries, and 3) to dissipate kinetic energy input from the cracking pipe." These rules can be extended to other pressurized vessels as well.

Damage arrestment can be initiated by a number of factors. Most commonly, however, it is induced through the use of strips or rings of material whose material properties differ from the material in which the crack originated.

Crack arrestment systems have been extensively studied by the navy for use in ship hulls, which are typically made of brittle metals [33]. Crack arrestors identified for ships include riveted, instead of welded, seams, arrestor strakes of a different material inserted between hull sections, compression patches designed to unload tensioned sections of the hull, riveted and continuously attached stiffeners which change bending stiffness and cross-sectional area, and ditches which turn cracks by providing a lower-energy path for notch propagation. Few of these methods are appropriate for composite materials; however, the basic methodologies of crack arrest, including changes in strain states and material properties of the structure, may have applications.

Damage arrestment in composite materials has been studied both in plates and shell structures. Bhatia and Verette [34] have studied the use of implanted buffer strips, similar to the arrestor strakes used in metallic structures, to arrest propagating cracks in plates. Testing of $[0/\pm45/90]$s plates made of T300/SP286 has indicated that this method of changing material properties to alter stress intensity factors and strain energy

release rates at the crack tips is promising. Experimental work involved replacing 25 mm wide strips of the 0° and 90° plies with ±45° sections. These buffer strips were located 50 mm apart on either side of a precut notch. Tensile tests showed that fracture paths originating at notches 19.1 and 25 mm in size propagated to the buffer strips and were turned to ±45° before stopping within the strip. Further tensile testing of the same specimens was used to show that the load-carrying capability of the laminates was increased by 20% over the value at which initial notch propagation occurred. Sendeckyj [35] was able to predict both the fracture initiation load and the residual strength of these laminates based on the fracture behavior of the primary and buffer strip materials.

Jozavi, Dupuis, and Sancaktar [32] have investigated the fracture behavior of a filament-wound unidirectional fiberglass/epoxy composite crack arrestor designed for use on a commercial metallic pipeline. Experimental results indicate that the fracture energy required for a crack to propagate across the fibers is forty times higher than that needed for propagation along the fiber direction. The use of a stiffener composed of circumferential fibers will therefore provide a lower-energy path for notch propagation in the hoop direction than it will in the axial direction. An approaching crack may then follow the path of least resistance and turn, dissipating its energy by travelling circumferentially. Thus, the axial propagation of the notch is arrested.

Although the work described above has been conducted primarily for pipelines carrying pressurized gases, the basic principles governing crack propagation are the same for other pressurized structures as well. It should be noted, however, that pipeline work considers mainly axial propagation of slits. In a long, narrow structure like a pressurized gas

pipeline, it is reasonable to consider flaw propagation in the axial direction as the major form of critical damage. In wider shells such as fuselages, however, damage propagating both axially and circumferentially must be considered since the ability of the craft to remain whole is severely affected by both.

It is of interest, therefore, to examine the damage propagation of a slit in a composite cylinder, and to evaluate the effects of stiffening bands on both the distance and direction of the flaw's propagation. Ideally, both axial and circumferential stiffeners would be used to contain any damage and subsequent flaw propagation to a small enough region that catastrophic fracture of the structure would not occur. In the interest of keeping the problem tractable, however, the stiffening bands must be considered individually.

Much of the work conducted on stiffened cylinders has focused on circumferential stiffeners. Graves [1,3] added stiffeners in the form of co-cured unidirectional bands to $[0_f/45_f]_s$ cylinders with axial slits. Although the presence of these stiffening bands had no effect on fracture initiation, it did, in some cases, influence the direction of fracture propagation. In each case, two sets of four unidirectional bands 76 mm wide were incorporated into the cylinder layup on either side of the region where the slit was to be cut. A range of bending stiffnesses was provided by varying the stiffener layup between cylinders. In the unstiffened cylinders, Graves found that the flaw propagated axially towards the endcap before bifurcating, or branching at ±45° and continuing around the cylinder at the endcaps. Addition of stiffeners which were interleaved between the plies of the base cylinder did little to change the fracture mode. Addition of stiffeners to the exterior of the cylinder, however, did produce different results. The

fracture path propagated axially and bifurcated at the same point (inboard of the stiffeners) as did the unstiffened cylinder. However, the path turned sharply and travelled around the circumference of the cylinder at the stiffeners. Similar results were found for cylinders with two interior and two exterior stiffeners. The results showed that higher bending stiffnesses of the reinforced regions are related to redirection of the fracture path.

Sawicki [7] repeated this work with identical quasi-isotropic fabric cylinders containing precut flaws, and found that in all cases damage was redirected. It is possible that the kinetic energy effects induced when Graves' cylinders were punctured with a guillotine contributed to difference in the damage propagation modes. Sawicki was able to correlate the damage redirection in his experimental specimens with a finite element model of strains in the cylinder. The model indicated that the fracture propagated through the cylinder to relieve the maximum strains. He found that the geometry and loading conditions of the cylinder produced lower stresses and strains in the stiffened regions than in the unstiffened areas.

Despite the mixed results from previous work, it is clear that circumferential stiffeners have a constraining effect on the direction of damage propagation in quasi-isotropic graphite/epoxy fabric cylinders. Analytical work has supported this conclusion, and has indicated that fracture tends to propagate so as to relieve maximum strains in the quasi-isotropic specimens. However, no investigations have determined the effect of such stiffeners on structurally anisotropic or tape cylinders. It is not known how the coupling of bending-twist deformation or the use of a graphite/epoxy tape will affect fracture propagation in the cylinder.

CHAPTER 3

Experimental Procedure

The experimental portion of this investigation was designed to provide data on fracture and damage propagation for the specimens and laminates in question. Test matrices as well as specimen geometries are presented and the rationale for their selection explained. Detailed manufacturing, instrumentation, and testing procedures are described for both coupon and cylinder specimens.

3.1 Experimental Approach

The purpose of the experimental portion of this investigation is to determine the failure pressures and characteristics of quasi-isotropic and structurally anisotropic graphite/epoxy tape cylinders. A quasi-isotropic $[90/0/\pm45]_s$ laminate was chosen in order to compare results with previous work conducted on quasi-isotropic $[0_f/45_f]_s$ cylinders. Structurally anisotropic layups of $[\pm45/90]_s$ and $[\pm45/0]_s$ were chosen for several reasons. These are relatively simple layups which are easy to manufacture, and for which much coupon fracture data already exists [14]. The two layups are complementary; the $[\pm45/0]_s$ has fibers in the direction of circumferential stress and the $[\pm45/90]_s$ has fibers along the axial loading and slit axes. Thus the effects of having fibers along either of the two directions of principal loading can be examined. The use of these two layups also helps to determine which failure characteristics are laminate-specific and which are due to the structural anisotropy of the laminates. All specimens were

made of Hercules AS4 fibers in a 3501-6 resin. The material properties and calculated laminate properties are given in Table 3.1.

All fracture prediction methodolgies described in Chapter 2 require a knowledge of specimen fracture properties to predict the failure pressures of similar cylinders. Tests were thus conducted on notched and unnotched $[90/0/\pm45]_s$, $[\pm45/90]_s$, and $[\pm45/0]_s$ coupons to obtain values for the composite fracture parameter, H_c, for use in the Mar-Lin failure stress correlation. The test matrix for the tensile coupons is shown in Table 3.2. Although notch geometry has been shown to have no effect on coupon fracture stresses, slits were chosen as the notch types so that fracture of the coupons and cylinders could be directly compared. Slit sizes of 9.5, 12.7, 15.9, and 19.1 mm were used, and a coupon width of 70 mm was chosen to avoid finite width influences on coupon failure. The tensile coupon is shown in Figure 3.1. The actual test section is 200 by 70 mm, and the slits are centered in this region and are perpendicular to the loading axis. The specimens are defined by a right-handed coordinate system with loading applied along the 0° axis.

Cylinders of the same layups were manufactured and tested. A test matrix for all cylindrical specimens is shown in Table 3.3. A cylinder radius of 152 mm was chosen to match the experimental work done in previous investigations [1-7]. A cylinder length of 760 mm was selected to assure that initial failure at the slit and damage arrest by the stiffeners did not interfere with one another. Slit lengths were chosen after the coupon data had been collected and the cylinder failure predictions had been calculated. Slit sizes are bounded on the lower side both by manufacturing limits and by a maximum failure pressure imposed by current testing procedures. For the purposes of this investigation, slit sizes ranged from

Table 3.1 Material and Calculated Laminate Properties

Material or Laminate	E_L [GPa]	E_T [GPa]	ν_{LT}	G_{LT} [GPa]
AS4/3501-6	142	9.8	0.3	6.0
[±45/90]$_s$	26.7	61.8	0.3	26.5
[±45/0]$_s$	61.8	26.7	0.7	26.5
[90/0/±45]$_s$	55.5	55.5	0.3	21.4
AW370-5H/3501-6S	74.1	73.1	0.06	6.45
[0$_f$/45$_f$]$_s$	54.2	53.7	0.3	20.6

Table 3.2 Test Matrix for Tensile Coupons

Laminate	Slit Length (mm)				
	Unnotched	9.5	12.7	15.9	19.1
[±45/90]$_s$	8[a]	4	4	4	3[b]
[±45/0]$_s$	8	4	4	4	4
[90/0/±45]$_s$	3[b]	4	4	4	4

[a] indicates number of specimens tested

[b] one specimen damaged prior to testing

Top View   **Side View**
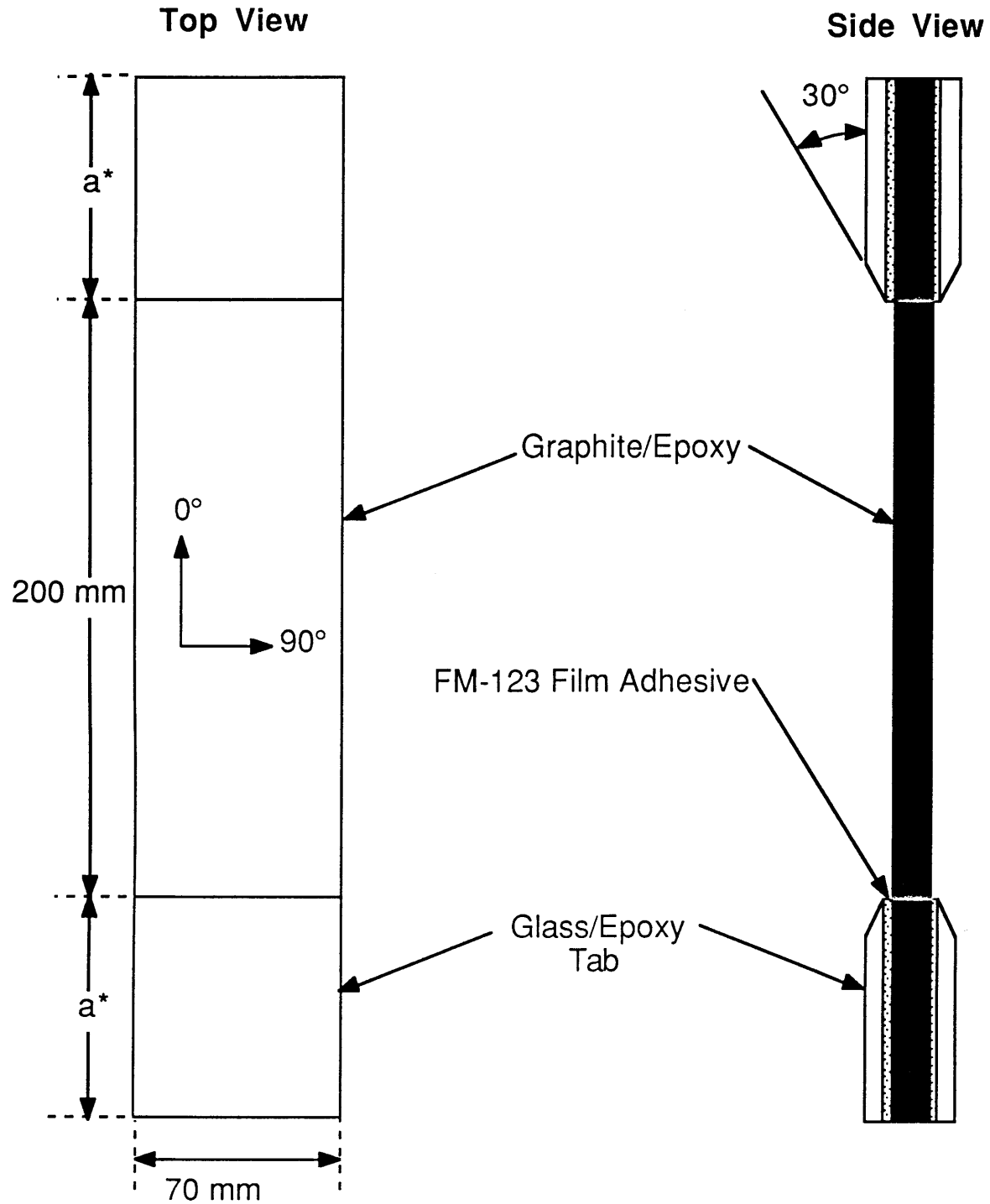
* for [±45/90]s and [±45/0]s coupons, a = 75 mm
  for [90/0/±45]s coupons, a = 50 mm (due to manufacturing error)

Figure 3.1 Tensile Coupon Configuration.

Table 3.3 Test Matrix for Cylindrical Specimens

Slit Size	Laminate[a]			
[mm]	$[90/0/\pm45]_s$	$[\pm45/0]_s$	$[\pm45/90]_s$	$[0_f/45_f]_s$
12.7	0[b]	4	4	0
25.4	0	0	0	--
38.1	0	4	0	--
50.8	0	2	4	--
63.5	--	2	2	--

[a] one specimen tested for each entry

[b] indicates number of stiffener plies for each cylinder tested

12.7 to 63.5 mm. The cylinder configuration is shown in Figure 3.2. Note that the 0° axis is along the circumferential direction. As in the coupons, the slit is parallel to the 90° axis and is centered on the specimen.

Stiffeners, which are placed symmetrically about the longitudinal center of the cylinder, cause local non-uniformities in the displacement and stress fields when the cylinder is pressurized. It is important that these fields do not exert influence at the slit tips, since initial failure predictions are based on the effects of the slit alone. In order to minimize stiffener influence on the stress field surrounding the slit, the circumferential stiffeners were placed at least one slit length from either end of the slit in all cases. Stiffeners were separated by 230 mm, leaving a minimum of 83 mm, or 1.3 times the length of the largest slit, between the slit tip and the edge of the stiffener. The stiffeners themselves are 76 mm wide as in previous work [1,3,7]. Stiffeners were placed only on the [±45/90]$_s$ and [±45/0]$_s$ cylinders; however, the unstiffened cylinders were made the same length for purposes of comparison. This length is determined from several considerations as subsequently discussed.

Like the stiffeners, the aluminum endcaps which seal the ends of the cylinder for pressurization locally affect the deflection and stresses in the cylinder. The radial deflection of an unflawed, internally-pressurized cylinder can be determined in the closed form [1]. A graph of radial deflection versus length for an unflawed, unstiffened [±45/90]$_s$ cylinder is presented in Figure 3.3. The radial deflection of the cylinder is constant in the center of the cylinder; this is the test section of the specimen. Towards the edges of the cylinder, the radial deflection increases dramatically before falling to zero at the endcaps. This edge zone, due to the constraints that the endcaps impose on the cylinder ends, is a region in which laminate
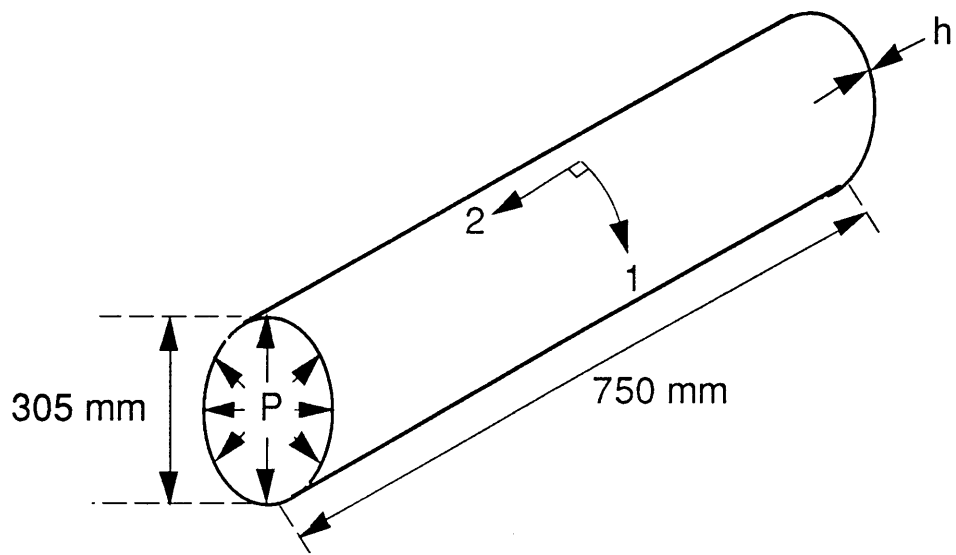
P = Internal Pressure

NOTE: Not to Scale

Figure 3.2 Cylinder Configuration.
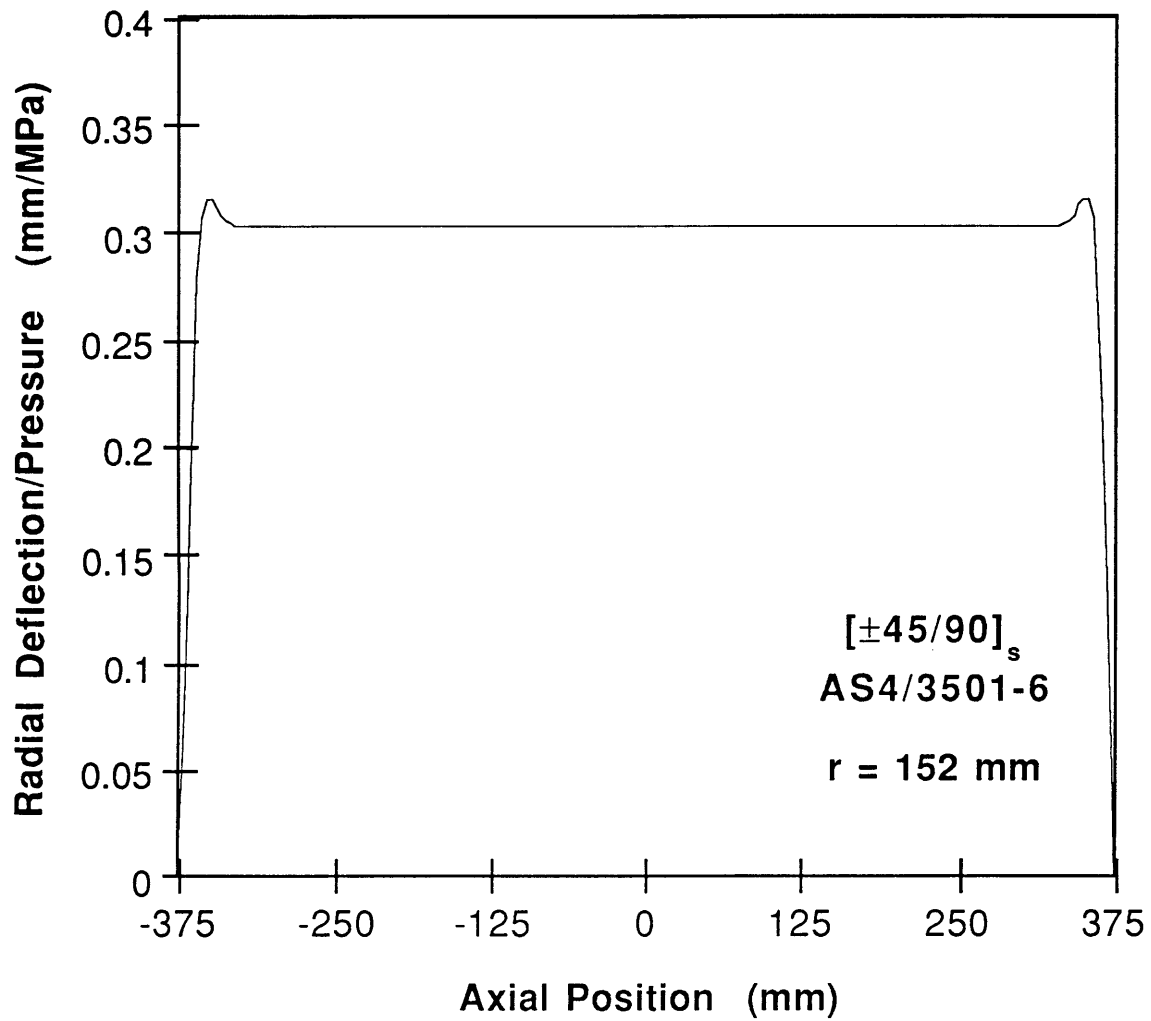
Figure 3.3 Plot of Radial Deflection versus Axial Position for an Unflawed,
Unstiffened [±45/90]s Cylinder.

strains change significantly over short distances. For all cylinders presented here, this edge zone is roughly 75 mm long at each endcap. In order that the local stress fields of the stiffeners and slit are not affected by these edge zones, the endcaps must be far enough from the stiffeners that no interaction occurs.

In order to evaluate how the stiffeners alone affect the direction of propagation of the slit, it is important that the endcaps and associated edge zones do not interfere with the stiffener's local bending and stresses. For these reasons, a length of 150 mm is left between each endcap and the outside edge of the stiffeners. The total length of the cylinder, 760 mm, may thus be determined as a sum of the maximum slit length, stiffener safety zones, stiffener widths, and cylinder edge zones. An additional 50 mm of length is added to allow for attachment of the endcaps at either end of the cylinder.

The stiffeners were laid up on the external surface of $[\pm45/90]_s$ and $[\pm45/0]_s$ cylinders as shown in Figure 3.4. The number of stiffeners was chosen so that the effect of a range of bending stiffnesses could be examined. The number of stiffener layers varied from zero to four, increasing the bending stiffness of the region up to 20 times that of the base laminate. At least one specimen of each layup has no stiffeners so that the unstiffened fracture path can be determined. It should be noted that two individual tests, determination of both fracture initiation load and fracture propagation characteristics, are being conducted with each specimen. The stiffeners are located far enough from the slit so that the initial fracture pressure of the cylinder is not affected by it. Thus, no attempt to correlate slit sizes and number of stiffener layers was made in selecting the test matrix since these are two different phenomena.
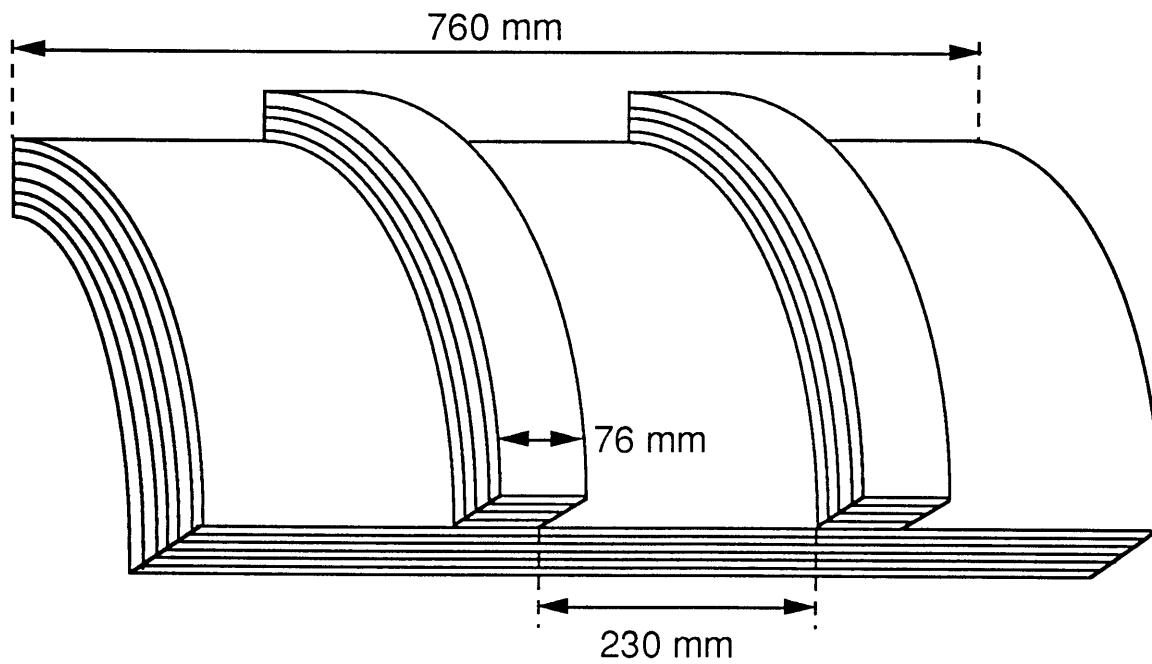
Figure 3.4 Schematic of Cylinder with Four Layers of External Stiffeners.

Due to unexpectedly high failure pressures obtained for the cylinders with 12.7 mm long slits, a $[0_f/45_f]_s$ quasi-isotropic fabric cylinder with the same slit size was manufactured and tested for comparison. A cylinder radius of 152 mm and length of 760 mm were chosen to match the other specimens used in this investigation. No stiffeners were added. Because the fracture parameters of the AW370-5H/3501-6S system in this laminate configuration has been determined in previous work [29], no additional coupon testing was conducted. Material and laminate properties can be found in Table 3.1.

3.2 Manufacturing Procedure

All experimental work was conducted in the Technology Laboratory for Advanced Composites. Manufacturing and testing of tensile coupons and cylinders were performed according to the procedures developed in the laboratory and outlined in the TELAC Manufacturing Class Notes [36]. Additional experimental methodology was developed as required in the course of the investigation.

3.2.1 Tensile Coupons

Tensile coupons were manufactured according to the standard techniques outlined in the TELAC Manufacturing Class Notes [36]. Six 355 by 305 mm laminates were manufactured for each layup. Laminates were cut into four coupons 70 mm wide. Fiberglass loading tabs were bonded to the ends of all coupons, and slits were cut in some specimens as previously indicated in Table 3.2.

Individual plies were cut from a 305 mm wide roll of unidirectional AS4/3501-6 tape material. Razor knives and angle templates were used to cut out both parts of each ply as shown in Figure 3.5. Plies were spliced along fibers so that only matrix joints were formed. Plies were laid up by hand against a 90° angle iron to minimize angle deviations from the nominal. The corner of the laminate against the angle iron was marked as the 'good' corner for reference. Completed laminates were covered on both sides with 330 mm by 420 mm pieces of peel-ply and trimmed on three sides to exactly 305 by 355 mm, and the 'good' corner of each marked.

Laminates were cured according to standard TELAC manufacturing procedures. Three aluminum t-dams were placed on a 1.4 m by 0.8 m by 9.5 mm thick aluminum baseplate covered with guaranteed nonporous teflon (GNPT). Two layers of cork dam were placed adjacent to the aluminum t-dams to form six 305 by 355 mm rectangles. Pieces of GNPT 355 by 405 mm were centered in the bays formed by the cork and aluminum dams, and the laminates were placed on top. The laminates were covered with sheets of porous teflon to keep the subsequent layer of paper bleeder from sticking to them during the cure cycle. To soak up excess epoxy, one sheet of paper bleeder was laid on top of the laminates for every two plies of graphite/epoxy. Another piece of GNPT was used to separate the laminates from the 9.5 mm thick aluminum top plates, which fit directly into the individual bays. These top plates were used to apply equal pressure to all parts of the laminate during the curing process. The layup assembly was covered with two layers of fiberglass airbreather. The airbreather not only protects the external vacuum bagging from being punctured by the metal corners of the top plates and t-dams, but it also aids the flow of air and other volatiles from the center of the plate to the vacuum ports located at either

ply cut

355 mm

prepreg
material
direction

305 mm

matrix joint

laid-up ply

355 mm

305 mm
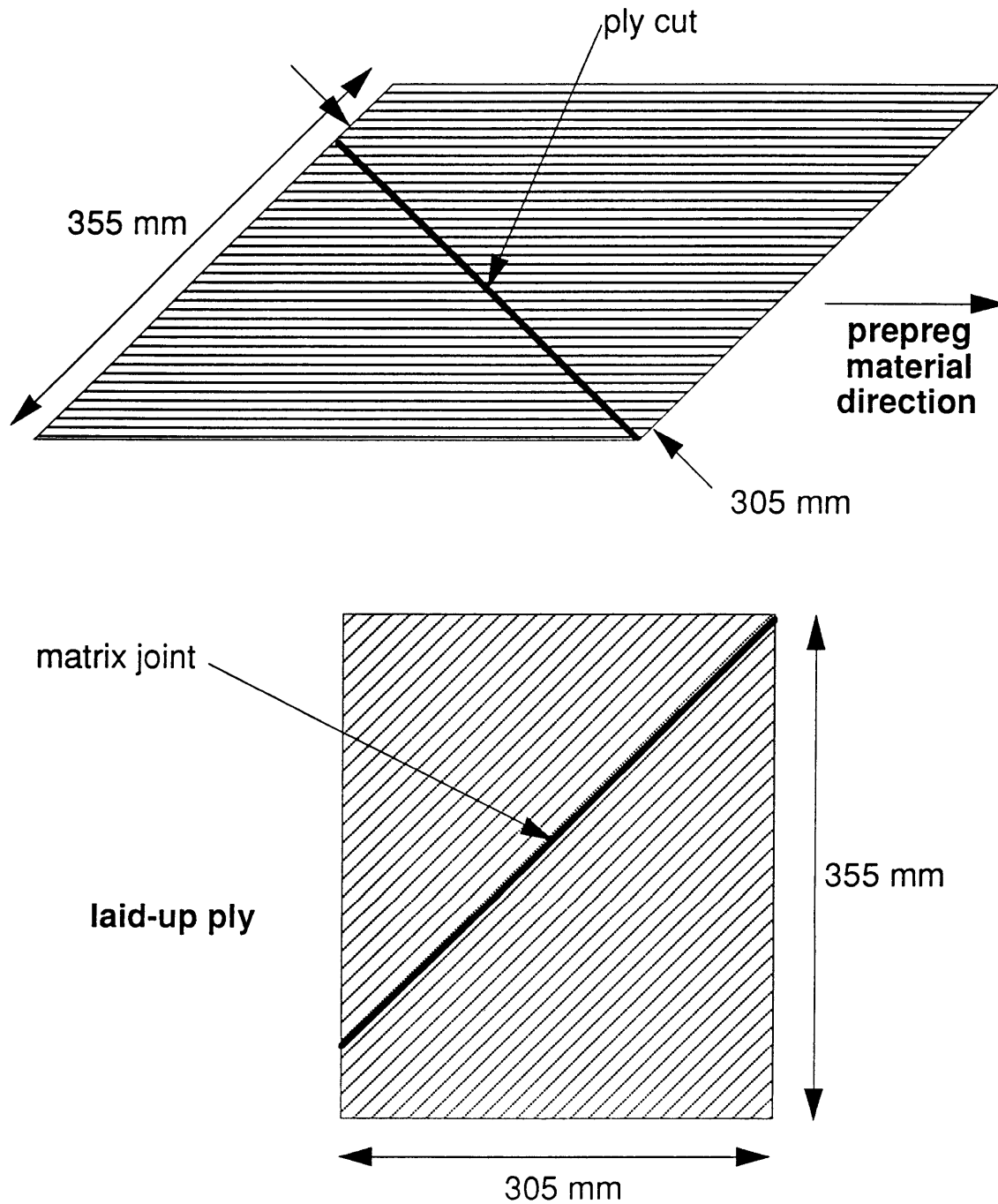
Figure 3.5 Schematic of Angle Ply Cuts and Matrix Joints in Laid-Up 45°
Ply.

end. The entire assembly was covered with vacuum bagging which was sealed to the edges of the baseplate with vacuum tape. A schematic of the cure layup is shown in Figure 3.6

The laminates were cured in an autoclave under vacuum and an additional 0.59 MPa of applied pressure. Before initiating the cure cycle, it was necessary to check the integrity of the plate's vacuum seal by performing a vacuum leak test. Vacuum was pulled and shut off, and the plate was left untouched for 5 minutes. If the strength of the vacuum dropped more than 75 mm Hg in this time, the plate was rebagged and the test repeated. Upon sucessful completion of the vacuum test, the plate was placed in the autoclave and the laminates were cured according to the manufacturer's instructions. Graphs of the temperature, vacuum and pressure applied during the cure cycle are shown in Figure 3.7. An atmospheric vacuum of 760 mm Hg was pulled and 0.59 MPa of pressure were applied in the autoclave to ensure proper consolidation of the laminates. The temperature was raised to 115°C at a rate of 3°C per minute. After a one hour hold at 115°C, the temperature was raised to 177°C at the same rate. The laminates were cured at 177°C for two hours, and were then slowly cooled at 3°C/minute to minimize any thermal stress effects. Laminates were removed from the cure plate and were post cured in their peel-ply coverings for an additional eight hours at 177°C. Postcuring was accomplished in an oven without pressure or vacuum capabilities.

The edges of the laminates were trimmed and four coupons 70 mm wide were cut from each laminate. Cutting was accomplished on a milling table with a 155 mm diameter diamond-grit cutting wheel rotating at 1100 rpm. The 'good' corner, marked prior to the curing process, was used to

Vacuum Bag   Fiberglass Cloth

Al Top
Plate

Porous
Teflon

Peel-Ply

Nonporous Teflon

Bleeder Material

Laminate

Nonporous Teflon

Vacuum Tape

**Cross-
Section**   Cork Dams   Al

Al Caul Plate

Top View

Laminate

Vacuum
Tape
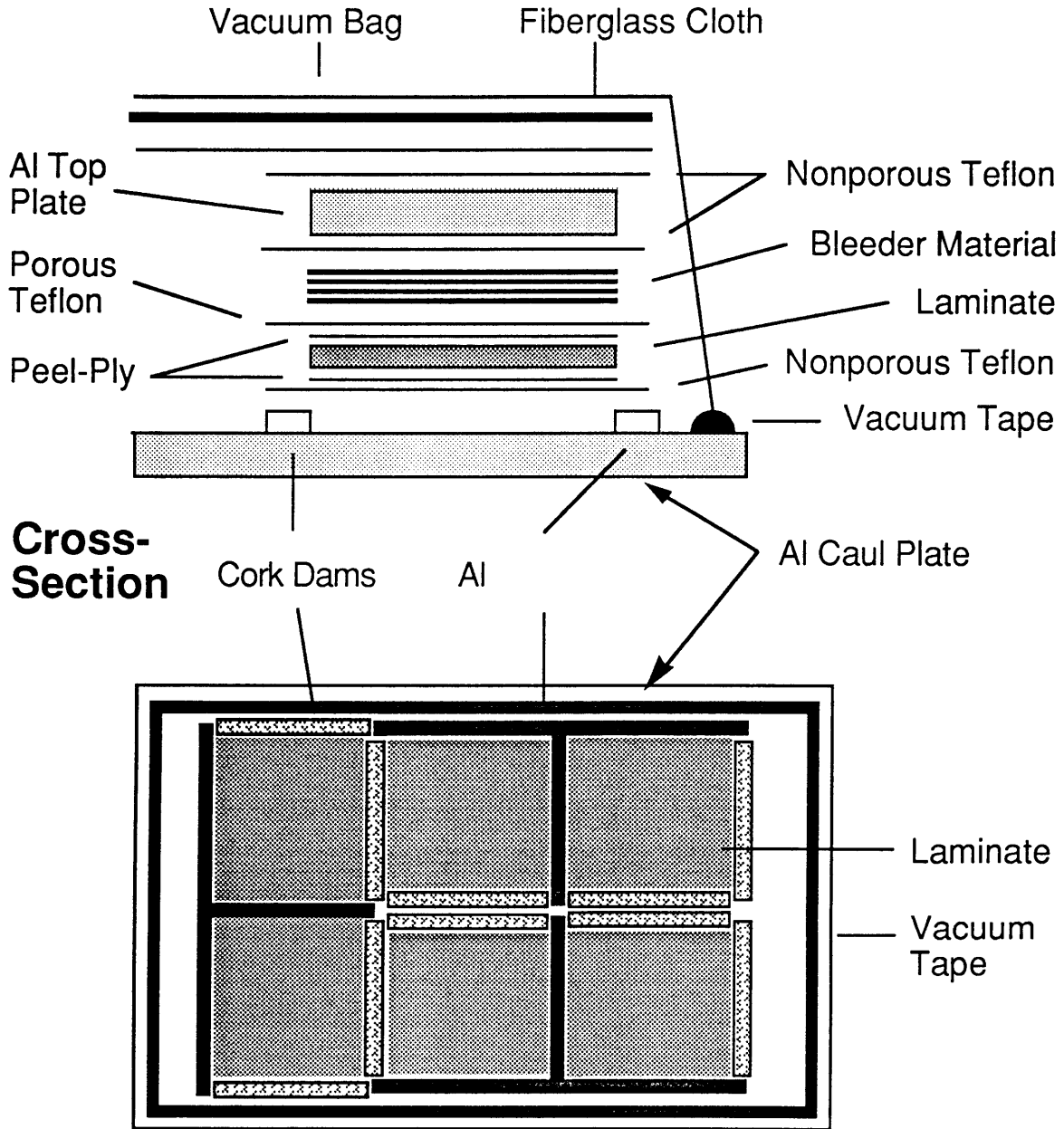
Figure 3.6 Illustration of Cure Assembly for Laminates.
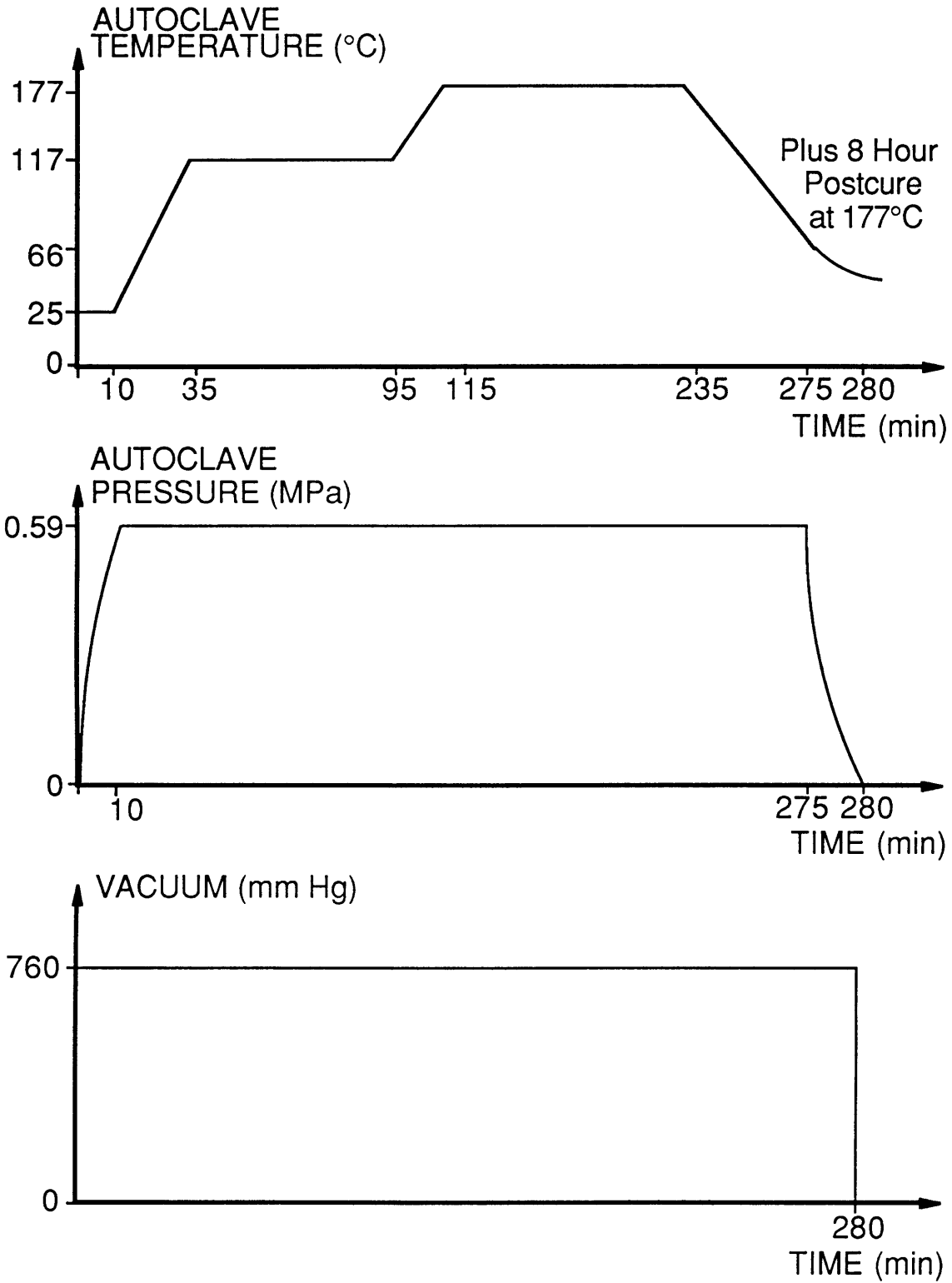
Figure 3.7 Standard Cure Cycle for AS4/3501-6 Graphite/Epoxy Laminates.

aid in the alignment of the laminate with respect to the cutting wheel. Care was taken to cut along the 0° axis of the laminate so that the coupon plies would have the same angles as those in the parent laminate. Three width and nine thickness measurements were taken in the center of each specimen's test section to assure specimen uniformity and to compare actual laminate thickness with the nominal values supplied by the manufacturer. A schematic of the specimen with measuring points is shown in Figure 3.8. Average ply thickness for all coupons was 0.140 mm, compared to the nominal value of 0.134 mm, indicating that the laminates were slightly thicker than expected. The width of all coupons averaged to 70.2 mm. Thickness and width values for individual coupons are presented in Appendix A. Nominal values for both width and thickness were used for all subsequent calculations.

Fiberglass tabs 1.5 mm thick, manufactured in a 0/90 configuration, were bonded to both ends of each coupon to provide a reinforced gripping section through which the tensile load could be applied. The tabs, which were 70 mm wide and 75 mm long[3], were placed on both sides of each end of a coupon to leave a 200 mm long test section in the center of the coupon. The ends of the tabs nearest the test section were bevelled to 30° so that the applied load was transferred smoothly from the tabs to the laminate. Tabs were cut from 380 by 600 mm sheets of precured fiberglass/epoxy on a bandsaw. The bonding surface of the tabs was roughened with a belt sander for good adhesion, and the bevelled edges were formed in the same way.

---

[3] tabs for [90/0/±45]$_s$ coupons are 50 mm long
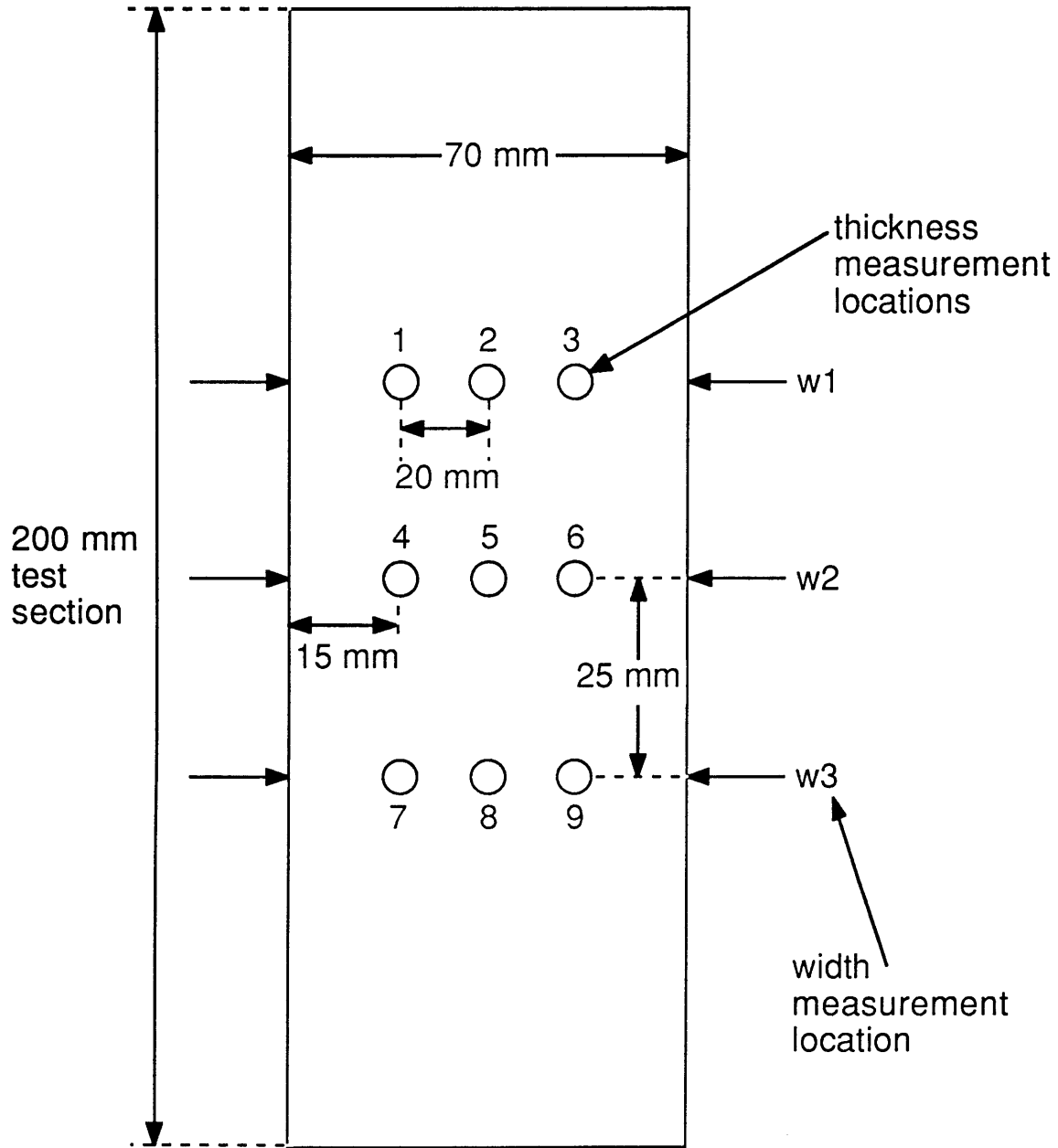
Figure 3.8 Schematic of Coupon Measurement Locations.

The tabs, as well as the coupons, were cleaned with cheesecloth and methanol to remove any dirt which could weaken the bond. The tabs were placed on a sheet of American Cyanamid FM-123 film adhesive, and a razor knife was used to cut around the edges of each. The film adhesive was warmed with a heat gun to increase its tackiness, and the tab was then positioned at the end of the specimen so that the inside (bevelled) edge of the tab was exactly four inches from the specimen centerline. This procedure was repeated until all four tabs were in place on each coupon.

The coupons, complete with tabs, were placed on an aluminum baseplate covered with GNPT. A layer of teflon was placed over the coupons to separate them from the steel top plates, used to distribute load during the cure. Since little epoxy flow was expected from the film adhesive, porous teflon was used. The assembly was covered with 4 layers of fiberglass and the plate was sealed with vacuum bagging as in the curing process. The tabs were bonded in an autoclave under atmospheric vacuum and 0.07 MPa of pressure. Once pressure was applied, the temperature was raised 3°C/minute to 107°C, where it remained for two hours. Cooling was done at the same rate to minimize thermal shock.

Slits were cut into the center of sixteen coupons of each laminate type, and were oriented perpendicular to the loading direction. Slit sizes of 9.5, 12.7, 15.9, and 19.1 mm were cut into four coupons each. Cutting was done with a diamond grit end mill 0.74 mm in diameter mounted on a rotary tool with a speed of 30,000 rpm. The rotary tool was fixed vertically to the arm of a milling machine and the coupons were clamped horizontally onto the milling table so that the bit was perpendicular to the specimen surface. The incidence angle of the bit on the coupon was checked with a master square, and adjustments were made by changing the angle of the

milling machine arm. The table was raised until the bit cut through the coupon near one end of the desired slit. The table was then moved sideways to cut the body of the slit. Several drops of water were carefully placed along the cut to cool and clean the bit during the cutting procedure. A schematic of this setup is shown in Figure 3.9. Slits were finished and their ends notched with a jeweler's saw whose teeth were filed to a point. Exact slit lengths, tabulated in Appendix A, were measured with a ruler and magnifying lens after the cutting procedure was complete.

3.2.2 Cylinders

Cylinders were manufactured according to standard TELAC procedures. Five cylinders each of the $[\pm 45/90]_s$ and $[\pm 45/0]_s$ layup, four of the $\{90/0/\pm 45]_s$ laminate, and one of the $[0_f/45_f]_s$ layup were made in the course of this investigation. A new procedure was developed to cut the slits in the cylinders.

An aluminum cylinder 1.2 m in length was used as the mandrel for the graphite/epoxy cylinders. The mandrel has an outside diameter of 305 mm and a wall thickness of 6.4 mm. During the layup procedure, the mandrel was mounted on a motorized tubewinder shown in Figure 3.10. The footpedal-operated tubewinder can rotate the mandrel in either direction at a speed of 3 rpm. Prior to the layup, a sheet of GNPT was wrapped around the mandrel and secured on the underside with transferrable adhesive tape.

A description of ply dimensions and layup procedures differs slightly for fabric and tape cylinders. Individual off-axis ply dimensions can be calculated for all cylinders from the diagram in Figure 3.11. The circumference of the cylinder, P, and the length, L, of the graphite cylinder

rotary tool

milling arm

milling machine

coupon

diamond grit
end mill

milling
table
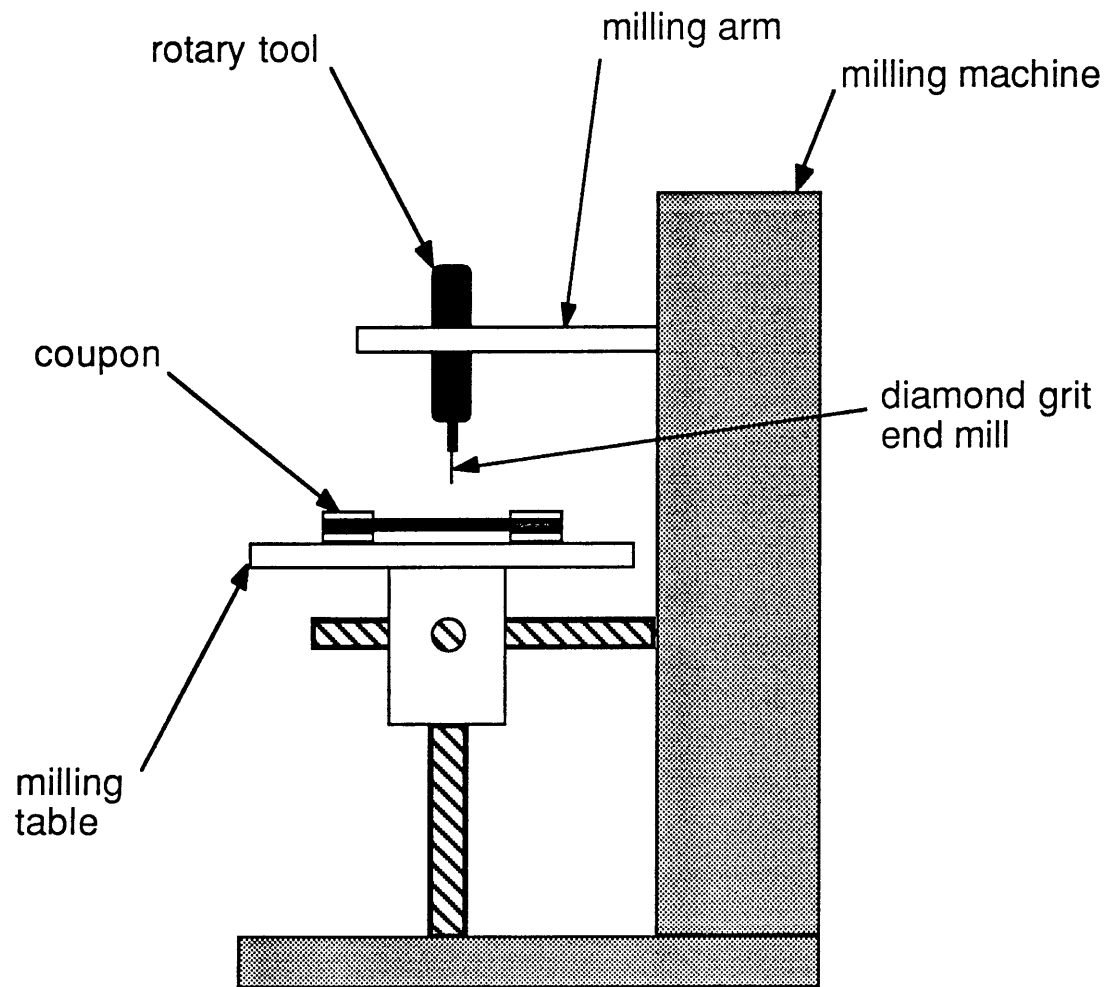
NOTE: Not to Scale

Figure 3.9 Schematic of Slit-Cutting Setup for Coupons.
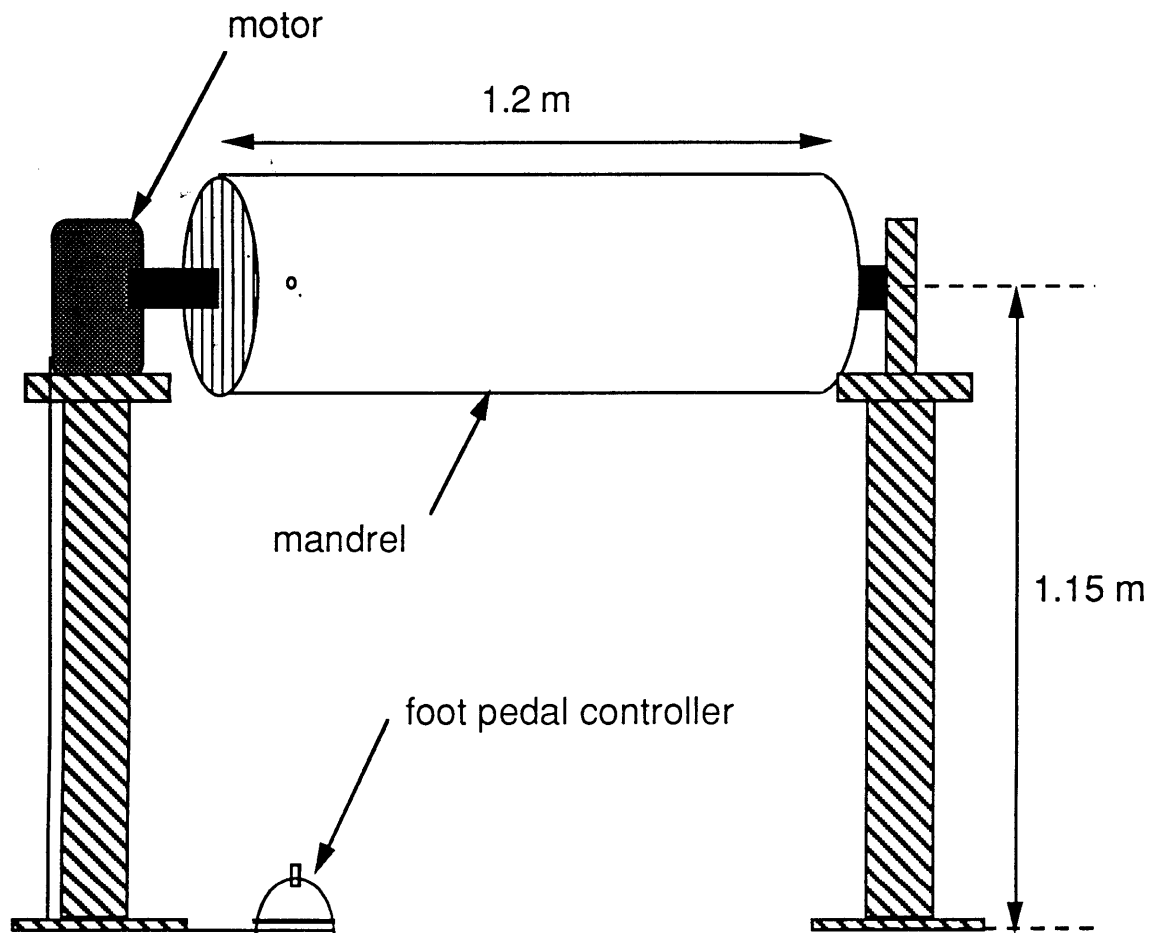
Figure 3.10 Schematic of Motorized Tubewinder.
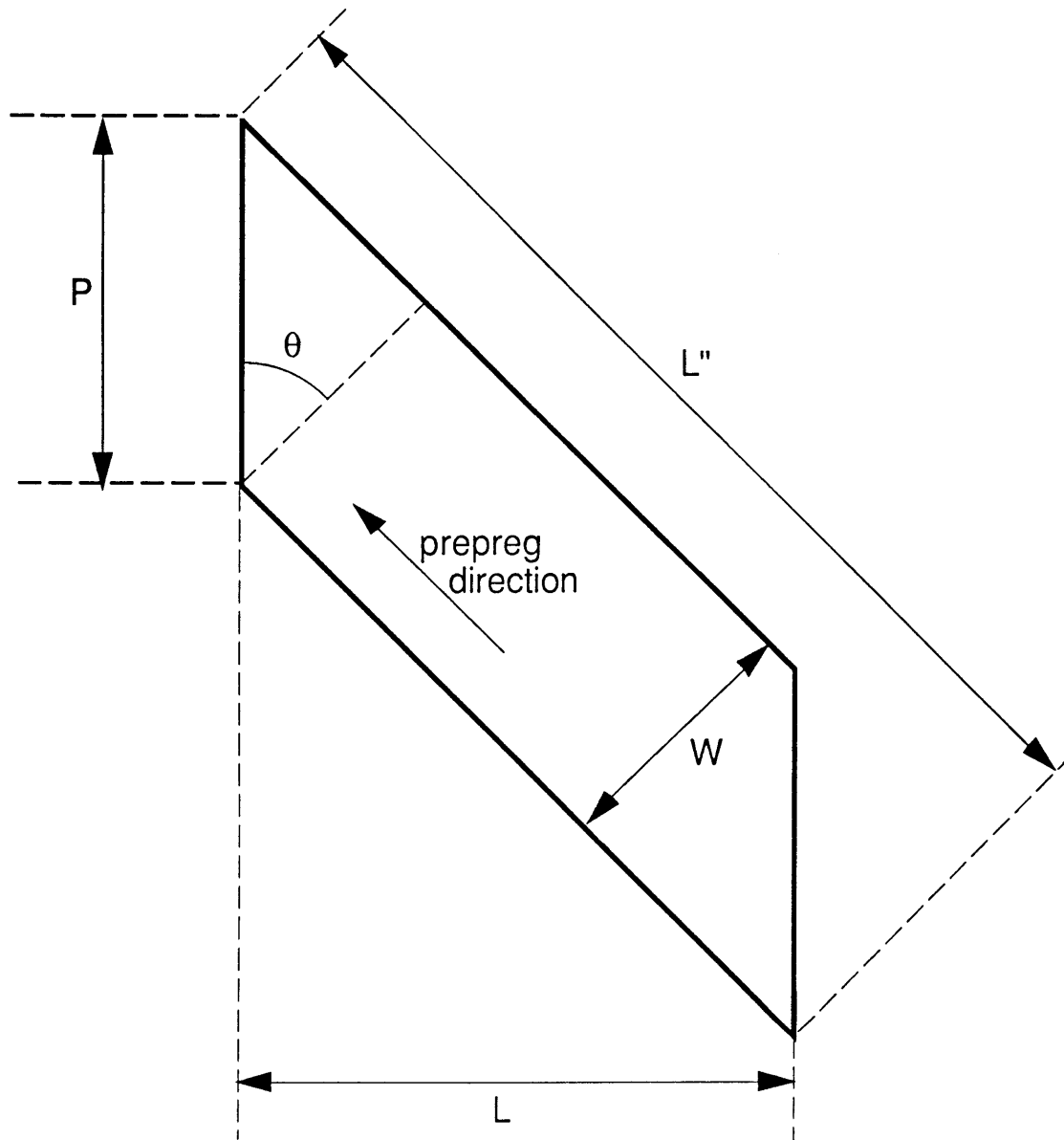
θ = ply angle
P = cylinder circumference
W = width of ply = P*cos(θ)
L = cylinder length
L" = length to cut = L/cos(θ) + P*sin(θ)

Figure 3.11 Illustration of Angle Ply Dimension Calculations.

are fixed values. Changes in angle of the ply, θ, and width, W, of the prepreg material can affect the overall ply length L".

Fabric plies were cut in one piece from a roll 1.5 m wide using a razor knife and angle templates. The plies were wrapped around the teflon-covered mandrel and were oriented so that the largest possible seam-free test area was formed. The seams of a ply overlapped by 12.7 mm so that there would be no butted fiber joints in the structure. Actual ply configurations for the $[0_f/45_f]_s$ cylinder are shown in Figure 3.12. Note that both +45° and -45° plies were cut to balance the layup and to avoid double seam overlaps at the back of the cylinder.

Plies for the tape cylinders were cut from a 305 mm wide roll of unidirectional material. Since the individual plies are wider than the roll of material, it was necessary to make a ply out of several 305 mm wide strips. With the exception of the 0° ply, ply splices were always made along the fibers so that only matrix joints were formed. The ply configuration, complete with ply splices, is shown in Figure 3.13 for a $[90/0/\pm45]_s$ cylinder. Note that the $[\pm45/90]_s$ and $[\pm45/0]_s$ cylinders simply include subsets of these plies.

The strips comprising the tape plies were applied to the mandrel one strip at a time, and were laid up side by side. Gaps between splices due to inaccurate calculations of ply width or sloppy layup were filled with thin strips of prepreg after the whole ply was down. The circumferential 0° plies were cut 12.7 mm longer than the cylinder circumference so that the ends could be overlapped at the back of the tube, away from the region where the slit was to be cut. No other plies had overlapping seams since all other splices were matrix joints.

Ply 1 (0°)
(interior)

760 mm

978 mm

Ply 2 (-45°)

760 mm

980 mm

Ply 3 (+45°)

760 mm

982 mm

Ply 4 (0°)
(exterior)

760 mm

984 mm
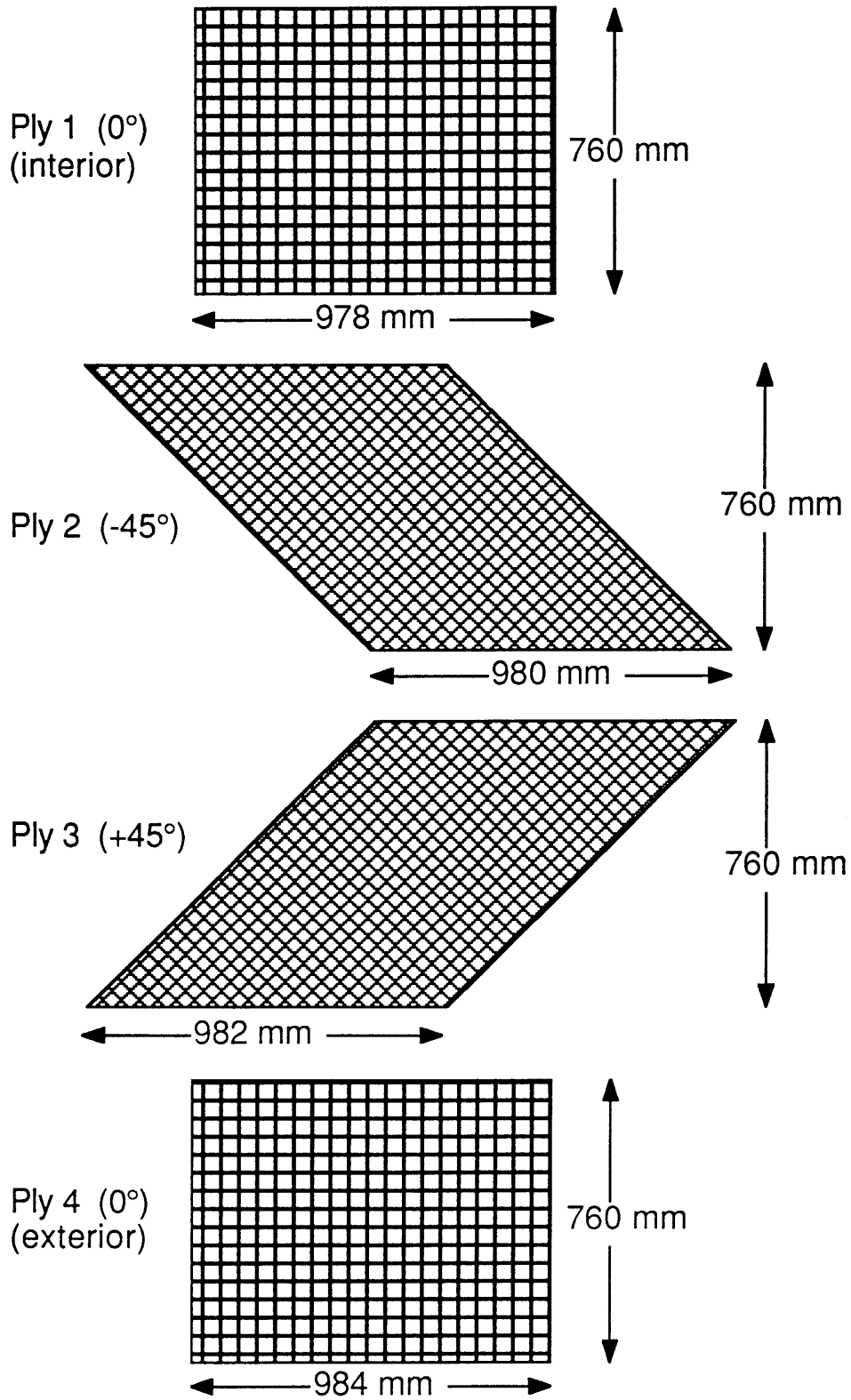
Figure 3.12 Illustration of $[0_f/45_f]_s$ Cylinder Ply Dimensions and Orientations.

90°

0° (circumferential)

90° (axial)

0°

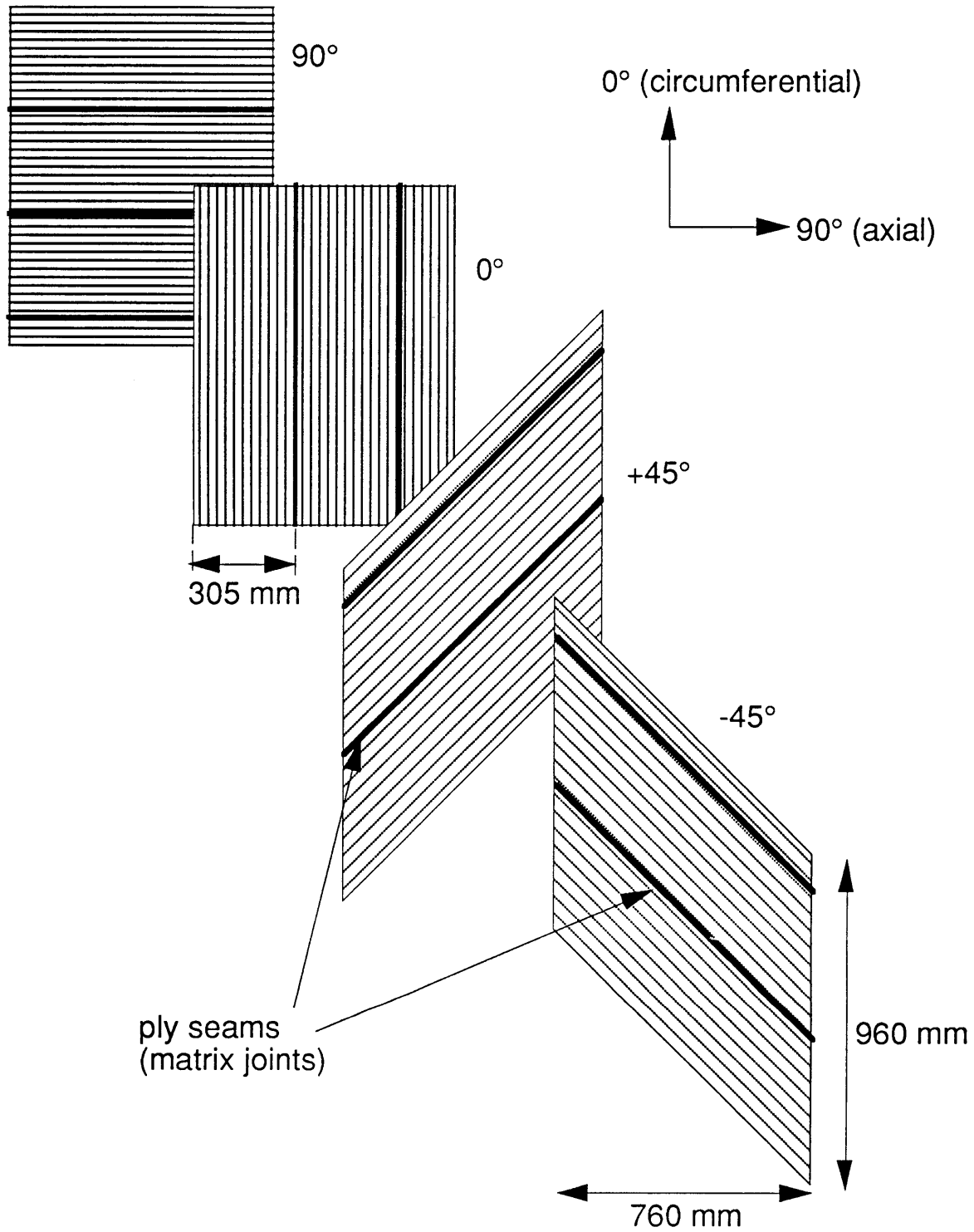305 mm

+45°

-45°

ply seams
(matrix joints)

960 mm

760 mm

Figure 3.13 Illustration of [90/0/±45]$_s$ Cylinder Ply Dimensions and
Orientations

As indicated in Table 3.3, groups of one, two, or four stiffeners were added to the external surface of some cylinders. The 76 mm wide 0° stiffening bands were laid circumferentially around the cylinder, and were 305 mm apart from center to center. The ends of each stiffener were overlapped 12.7 mm to avoid weak butt joints, and the seams of the individual stiffeners were staggered to minimize overlapping joints.

The cure material layup for the cylinders is analagous to that used for the coupons. When all plies are laid up, the cylinder is covered with one sheet each of peel-ply and porous teflon. A continuous sheet of paper bleeder is wrapped around the cylinder to soak up any excess epoxy flowing out of the laminate during the cure. Three layers of bleeder were used for the $[\pm45/90]_s$ and $[\pm45/0]_s$ laminates, four for the $[90/0/\pm45]_s$ laminate, and six for the $[0_f/45_f]_s$ fabric layup. Care was taken to wrap the bleeder tightly so that wrinkles would not form in the bleeder and graphite/epoxy during the cure cycle. Four layers of fiberglass air breather were wrapped around the mandrel from the vacuum port to the nearest edge of the graphite. This allowed air and volatiles liberated during the cure to be removed from the graphite/epoxy via the airbreather through the vacuum port. The entire assembly was sealed in vacuum bagging with vacuum tape.

The cure cycle for the cylinders is identical to that used for the coupons shown in Figure 3.6. Vacuum was drawn on the cylinder and 0.59 MPa of overpressure were applied in the autoclave. The temperature was raised to 115°C at a rate of 3°C/minute. After a one-hour hold, the temperature was raised to 177°C at the same rate. Upon completion of the curing process, the cylinder was cooled to room temperature, and the external cure materials including vacuum bagging, bleeder, porous teflon, peel-ply, and fiberglass were removed with a metal spatula. The cylinder

was pulled off the mandrel manually, and was postcured in a conventional oven for 8 hours at 177°C.

The ends of the cylinder, ragged from uneven layup and epoxy bleedout, were cut square to facilitate attachment of the endcaps. A straight-edged piece of teflon was wrapped tightly around the cylinder to denote the end of a right cylinder. The cylinder was trimmed to the edge of the teflon using a hand-held rotary tool fitted with a composite blade. Finer adjustments were made using a rough file. Squareness of the cylinder was determined by setting it on a horizontal surface and checking the proximity of the walls to vertical with a master square.

Due to the destructive nature of the tests, a 50 by 50 mm grid was drawn on the entire exterior surface of each cylinder with white paint. The grid squares were individually labelled to facilitate post-test reassembly of the remaining fragments. Cylinder thickness was measured at 90° intervals 50 mm in from each end of the cylinder. Average per-ply thicknesses of 0.143 mm for the $[\pm 45/90]_s$ and $[\pm 45/0]_s$ cylinders and 0.136 mm for the $[90/0/\pm 45]_s$ specimens, were slightly larger than the nominal value of 0.134. Nominal thicknesses are used in all failure prediction calculations.

An even and smooth area away from the ply seams was chosen for the location of the slit. Ply seams and occasional wrinkles, caused when friction between the graphite/epoxy plies did not allow them to slip over one another during the consolidation process, were avoided when choosing the slit location because the laminate was not uniform in these areas. A vertical line was drawn the length of the cylinder in the chosen location using a master square, and the center was found with a ruler. The slit

location and ends were clearly marked with a pencil line to facilitate cutting.

A new procedure for cutting longitudinal slits in the cylinders was developed for this investigation. Complementary convex and concave wooden holders were placed at each end of the cylinders to provide firm support for the clamps which held the cylinders to the milling table. The wooden holders not only provided a flat clamping surface but also prevented deformation of the cylinder at the clamping points. The cylinder was oriented so that the proposed slit location was 90° from the point where the cylinder rested on the table. A 30,000 rpm rotary tool with a 25 mm diameter composite blade was mounted vertically on the milling machine arm as shown in Figure 3.14. The height and sideways position of the milling table were adjusted until the blade was at the level center of the slit. The tool was turned on and the table, with the cylinder attached, was slowly moved towards the blade. Once the blade had cut through the laminate, the table was moved first in one direction and then in the other to cut the body of the slit. The table and cylinder were pulled back to free the blade when the cutting procedure was complete. Slits were cut to the correct length and notched at the tips by hand. A small jeweler's saw with pointed teeth was used to cut the ends of the slits to a sharp v-shape. Because the composite wheel used to cut the slits is 25 mm in diameter, it was not used to cut the 12.7 mm slits. These slits were cut by hand using first the rotary tool and then a jeweler's saw. A small 'starter' hole was drilled into the cylinder at the center of the slit using a diamond-grit drilling bit 0.74 mm in diameter mounted in a hand-held rotary tool. The length of the slit as well as the angled tips were then cut with the jeweler's saw.

rotary tool   milling arm

milling machine

cylinder

wooden
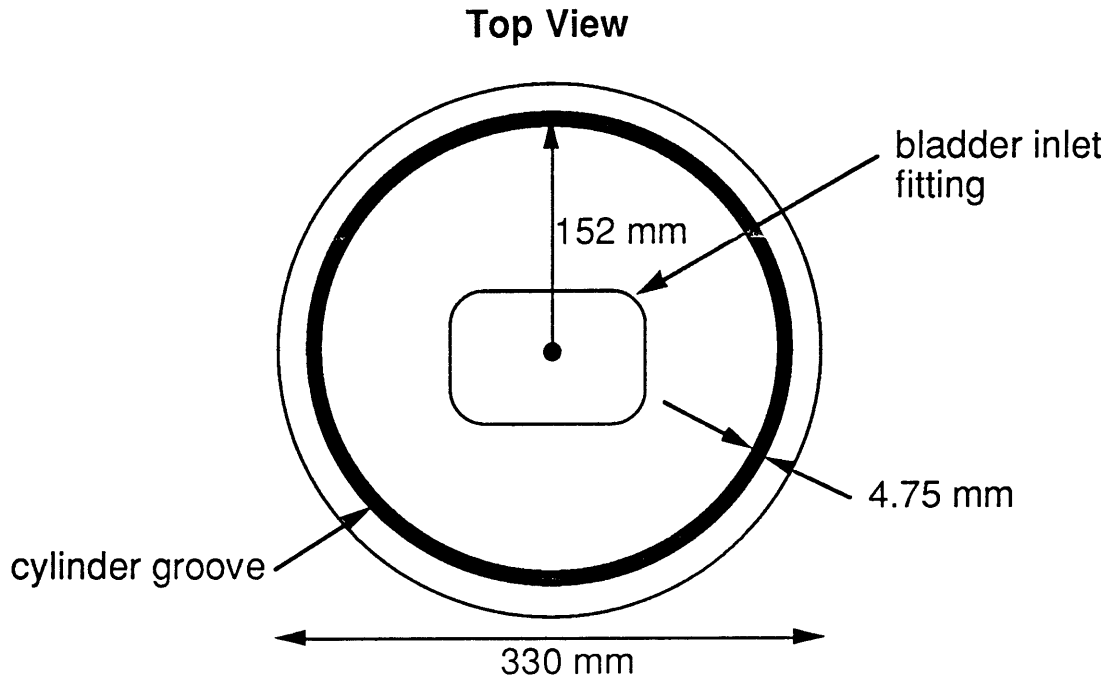support

milling
table

clamp
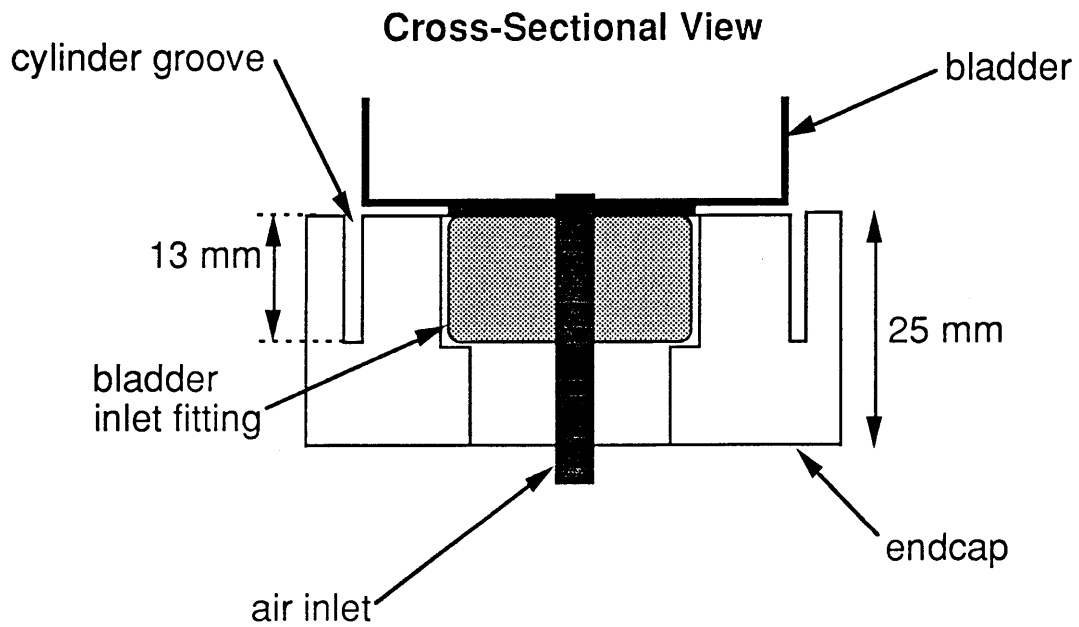
composite
wheel
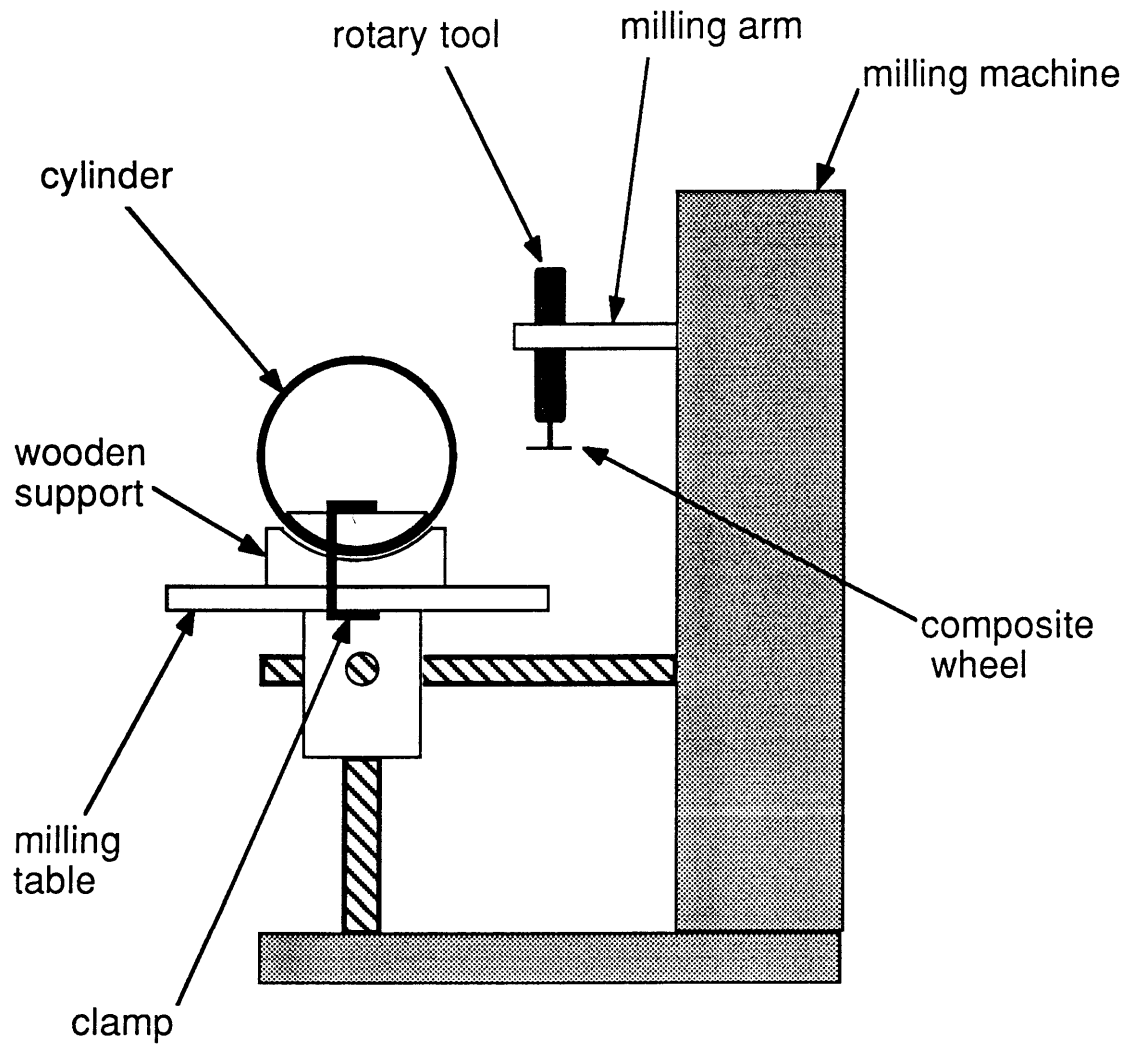
NOTE: Not to Scale

Figure 3.14 Schematic of Slit Cutting Setup for Cylinders.

The cylinders were sealed at both ends so that they could be internally pressurized. Aluminum endcaps 25 mm thick and 330 mm in diameter were used for this purpose. Each endcap has a circular groove 12.7 mm deep and 4.8 mm wide cut into it at a radius of 152 mm. The cylinder was bonded into this groove with a flexible structural adhesive. A pressure fitting was attached to one endcap to allow the pressurizing gas to enter. A schematic of the endcaps is shown in Figure 3.15.

The cylinders were potted into the endcaps one at a time. The endcap, especially the groove into which the cylinders fit, were cleaned thoroughly with methylethylketone (MEK) to remove any grit or dirt which might interfere with the bond. The endcap was heated to 80°C to make sure that all surfaces were dry in preparation for bonding. The inside edge of the cylinder was lightly sanded with 220 grit sandpaper to provide a rough surface to which the epoxy could adhere. The inside and outside ends of the cylinder were cleaned with methanol and cheesecloth to remove any residual dust remaining on the surface. Scotch-Weld Type 2216 B/A Gray Epoxy Adhesive manufactured by 3M was mixed in a ratio of 115 grams resin to 75 grams hardener, yielding a total of 180 grams of adhesive. Wooden tongue depressors were used to mix the epoxy in hexagonal plastic boats until the color was a uniform gray. The epoxy was poured into the groove of the heated endcap until the groove overflowed slightly. A layer of epoxy was painted on the inside and outside edges of the cylinder to a depth of 25 mm. The cylinder was then seated securely in the groove, and toothpicks were inserted around the outer edge of the cylinder to center it in the groove. Fillets of epoxy were formed around the inside and outside of the joint with a wooden stick so that the transfer of axial load to the cylinder during pressurization would be gradual. After all fillets were made, the

Top View

152 mm

bladder inlet
fitting

4.75 mm

cylinder groove

330 mm

NOTE: Bladder Fitting is in One of Two Endcaps Only

Cross-Sectional View

cylinder groove

bladder

13 mm

25 mm

bladder
inlet fitting

endcap

air inlet

NOTE: Not to Scale

Figure 3.15 Schematic of Endcaps and Bladder Fitting.

toothpicks were removed and any remaining holes were filled. The cylinder and endcap were then cured for one hour at 80°C to accelerate the hardening of the epoxy. The second endcap was potted in the same manner after the cylinder had cooled. A photograph of a potted cylinder is shown in Figure 3.16.

After a test, the endcaps were cleaned so that they could be reused for the next cylinder. Any graphite/epoxy remaining in the endcaps was trimmed with sheet metal cutters to a height of 25 mm above the surface of the endcaps. The endcaps were then heated to 260°C to denature the potting epoxy. The graphite/epoxy could then easily be pulled from the groove with vice grips. Thin metal scribes were used to scrape any remaining potting epoxy out of the grooves, and sandpaper was used to remove the epoxy from the top and side surfaces of the endcaps. The endcaps were reheated as necessary during the cleanup procedure to keep the potting epoxy flexible. Residual grit was removed from the surfaces and grooves with MEK and cotton swabs prior to endcap reuse.

Internal rubber bladders were made for each cylinder to contain the pressurizing gas. The bladders, made of gum rubber 0.8 mm (1/32 in) thick, were constructed from four pieces of rubber sealed together with vacuum tape and rubber cement. Two circular pieces of rubber 460 mm in diameter and two rectangular pieces measuring 1.1 m by 810 mm and 180 by 230 mm were cut from a 915 mm wide roll. Triangles 50 mm long and 25 mm wide were cut out of the circumference of the round pieces, leaving two toothed circles as shown in Figure 3.17. A 25 mm diameter hole was cut into the center of one circle, and the bladder inlet fitting, shown in Figure 3.15, was attached first to the smaller rectangle and then to the circle with Utility Industrial Adhesive Number 503 manufactured by Globe Rubber
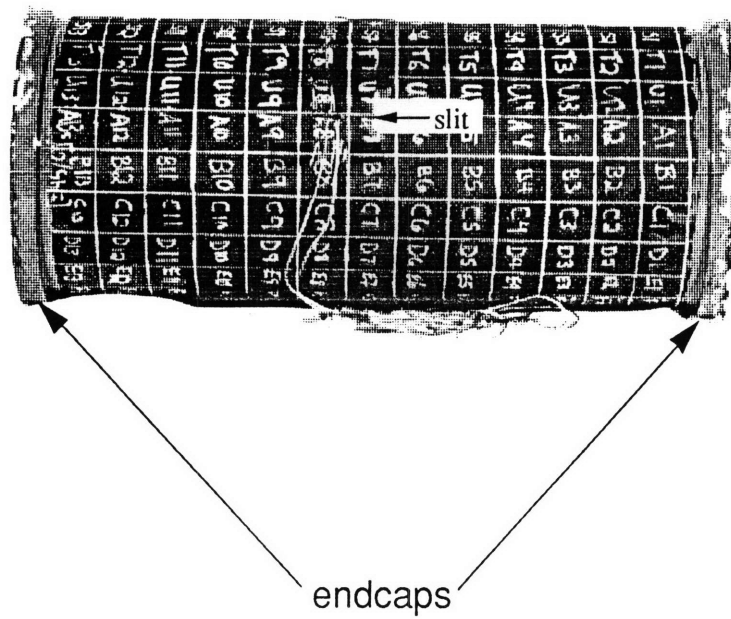
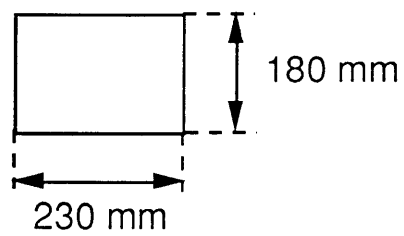Figure 3.16 Photograph of Cylinder with Endcaps.
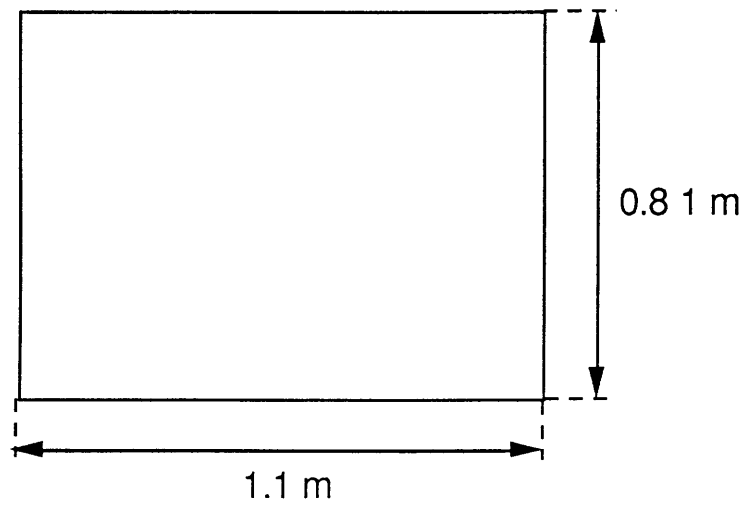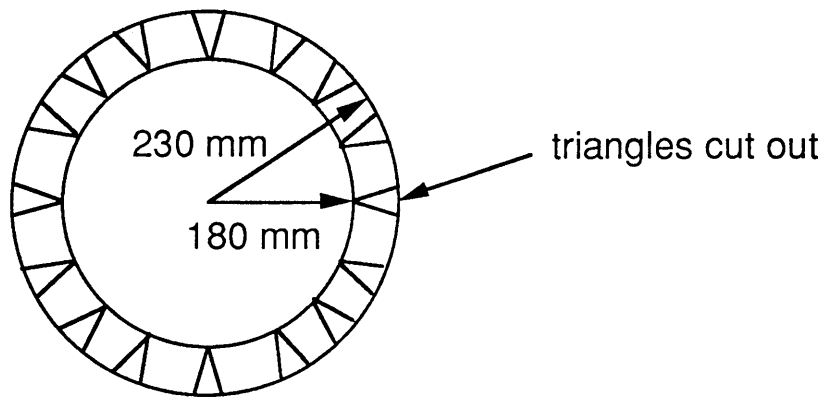
Figure 3.17 Schematic of Rubber Bladder Sections.

Works. The 810 mm long, 320 mm diameter cylindrical body of the bladder was formed by overlapping the ends of the larger rectangular piece and sealing them together with two strips of 13 mm wide vacuum tape #213-3 manufactured by General Sealants. The circumference of the body piece was made slightly larger than that of the cylinder so that pressurization would not force the bladder to stretch and rupture. The circular ends of the bladder were attached tooth by tooth to the ends of the rubber cylinder with strips of vacuum tape. Cylinders were filled with air and pressurized slightly to test for leaks in the vacuum tape seams. Leaks were identified by spreading a soapy film along the seams and searching for bubbles, which indicate escaping air. Utility Industrial adhesive was painted on leaky areas after the bladder was deflated, and the leak-checking procedure was repeated until the integrity of the bladder was established. A complete description of the bladder manufacturing process is given in reference [38].

Due to their poor load-carrying capabilities, the bladders did not measurably increase the cylinders' strength under pressure loading. The bladders, complete with bladder inlet fitting, were placed inside the cylinders prior to testing. Additional pieces of bladder material were taped over the slit from the inside of the cylinder so that the bladder would not be pushed through the opening during pressurization.

3.3 Instrumentation

Both coupons and cylinders were equipped with strain gages made by the Micromeasurements Company. The EA-06-125-AD-120 gages were used mainly to monitor the tests and check for any abnormalities. The

cylinders were attached to pressure sensing devices so that internal pressure at failure could be recorded as well.

3.3.1 Tensile Coupons

Strain gages were applied to both notched and unnotched coupons to check the quality of the manufactured laminates via determination of the laminate elastic constants. One longitudinal and one transverse gage were bonded onto each unnotched coupon. Gages were aligned along the vertical axis of the coupon, and were located 13 mm from the horizontal centerline as shown in Figure 3.18. These were used in determining the longitudinal modulus and Poisson's ratio of the laminate. Comparisons of calculated and experimentally-determined values were used to check the quality of the coupons.

Only one strain gage was placed on the notched coupons. This longitudinal gage was located at the quarter-width point of the specimen halfway between the slit and the loading tabs as shown in Figure 3.19. Strains and stress-strain relationships of the notched specimens were compared to unnotched coupon results to ascertain that laminate behavior was similar.

3.3.2 Cylinders

Cylinders were instrumented with strain gages as well as a pressure transducer and dial gage. Strain gage location varied from cylinder to cylinder. All cylinders were equipped with far-field axial and circumferential strain gages, located 120° from the slit in the circumferential direction. Data from these and additional strain gages was taken to help indicate cylinder behavior in case of unusual fracture results.
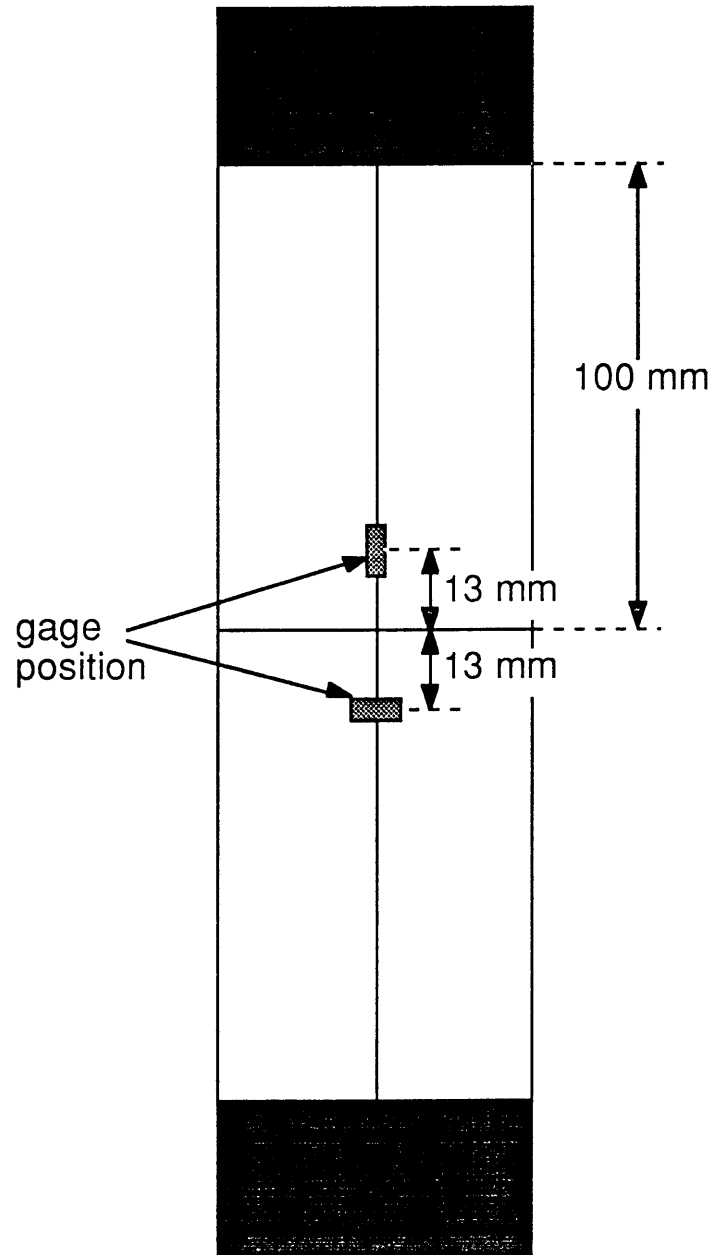
NOTE: Not to Scale

Figure 3.18 Illustration of Strain Gage Placement for Unnotched Coupons.
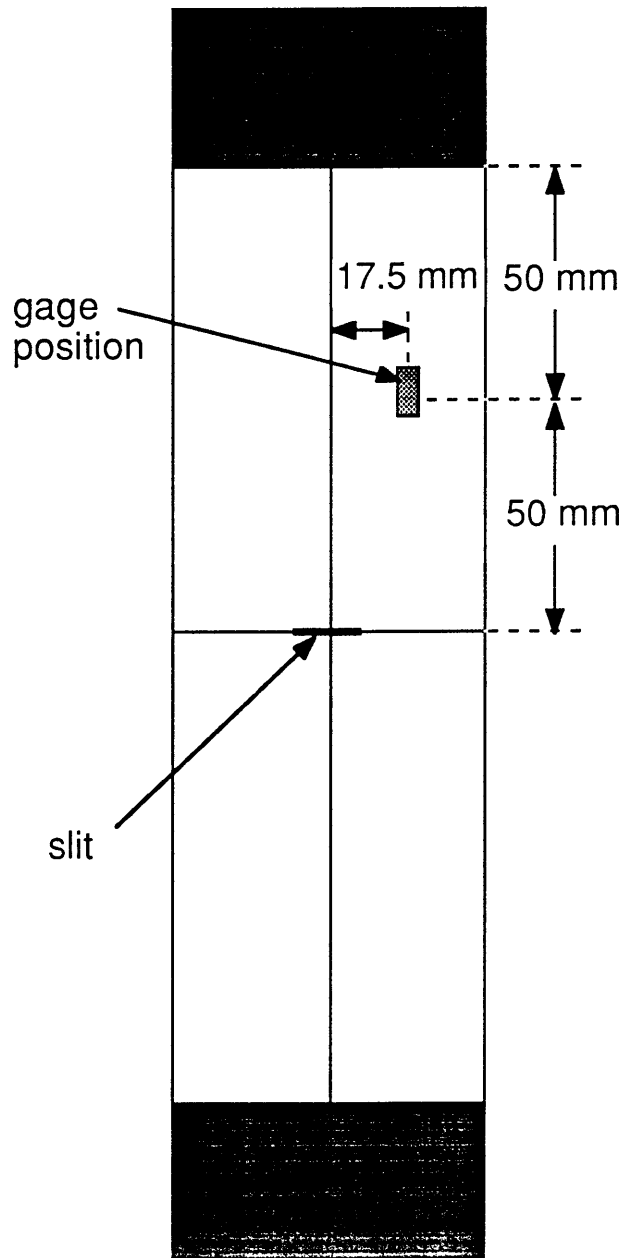
NOTE: Not to Scale

Figure 3.19 Illustration of Strain Gage Placement for Notched Coupons.

The pressurizing line leading to the cylinders was attached to a pressure transducer and an analog pressure gage. The pressure transducer was used to record cylinder pressure throughout the test, and the dial gage served as a real-time pressure monitor during the testing procedure.

3.4 Testing Procedures

All coupon and cylinder testing was conducted according to standard TELAC procedures developed by previous investigators.

3.4.1 Tensile Coupons

Tensile coupon testing was conducted using an MTS 810 testing machine. Coupons were inserted into the upper hydraulic grip of the testing machine first. A square was used to align the coupon along the loading direction, and the upper grips were closed to hold the coupon securely in place. The upper crosshead of the testing machine was lowered until the fiberglass loading tabs at the bottom of the specimen were squarely between the lower grip's jaws. Strain gages were calibrated and zeroed before the lower grip was closed.

Uniaxial tensile tests were conducted under stroke control at a rate of 0.018 mm/second, which corresponds to a strain rate of 90 μstrain/second in the test section. All coupons were tested monotonically to failure. Stroke, load, and strain data were recorded at a rate of 2 Hz until coupon failure occurred. Data for the $[\pm45/90]_s$ and $[\pm45/0]_s$ coupons was collected using a Digital PDP-11/34 computer. A Macintosh IIX equipped with the

Labviewdata acquisition package was used to collect [90/0/±45]$_s$ coupon data. In all cases, the data was transferred to a Macintosh system for reduction.

3.4.2 Cylinders

Cylinder testing was conducted in a blast chamber. A cylinder was placed horizontally on an iron channel in the center of the blast chamber. The cylinder, which rested on its endcaps, was oriented slit up so that the failure path would not be constrained by the channel. The ends of the cylinder were not fixed to the channel, and no restrictions were made on axial movement or expansion of the cylinder. Sandbags were stacked around the cylinder to protect the data-taking devices and to contain the endcaps when the cylinder failed. Pressure was fed into the blast chamber from an externally-located nitrogen tank through 9.5 meters of copper tubing and flexible hose. Pressure was fed to the cylinder via a 2 meter long, 6.5 mm inside diameter copper tube. A pressure transducer and a pressure dial gage were located 2 m along the line from the cylinder. The pressure transducer was used to collect accurate pressure information, and the dial gage was used to visually monitor pressure during the testing procedure. A schematic of the blast chamber setup is shown in Figure 3.20.

Cylinder pressurization was controlled manually with the use of a pressure regulator attached directly to the nitrogen tank. Cylinders werepressurized at an approximate rate of 0.4 MPa/minute, and the pressurization rate was monitored during the test via a dial gage and a chart recording of the pressure transducer output. Data, including strain gage readings and internal cylinder pressure, was collected at 0.5 second intervals. Data for the [±45/90]$_s$ and [±45/0]$_s$ cylinders with slit lengths 25.4, 38.1, and 50.8 mm, and that for the [±45/90]$_s$ specimen with slit length 63.5
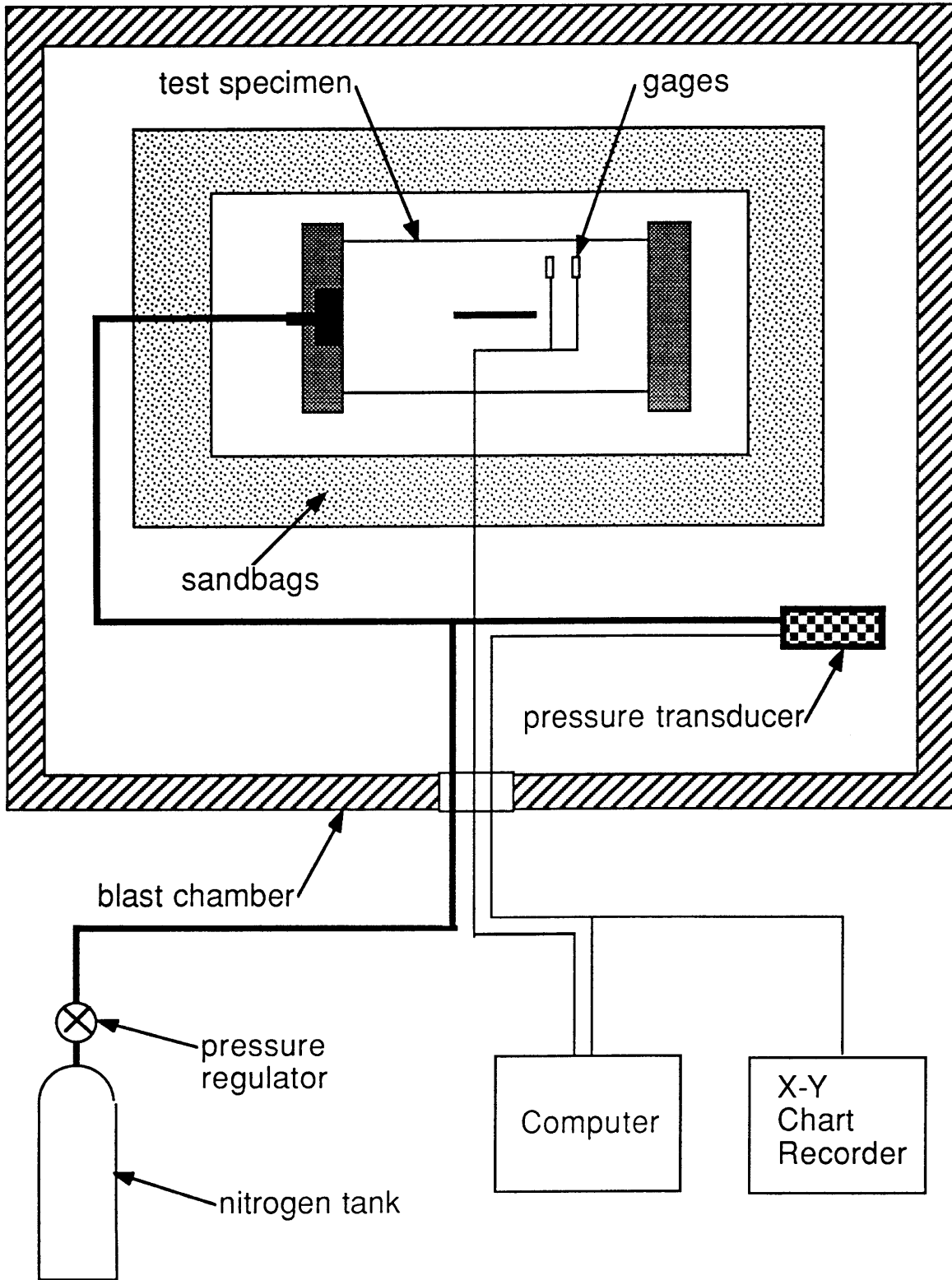
Figure 3.20 Schematic of Cylinder Testing Setup.

mm was collected via a PDP-11/34 Digital computer. The data for the remaining [±45/90]$_s$ and [±45/0]$_s$ cylinders as well as that for all [90/0/±45]$_s$ and [0$_f$/45$_f$]$_s$ cylinders was collected using the Labview package on a Macintosh IIX.

3.5 Post-Test Documentation

Photographs were taken of all coupons after testing to record failure modes. Comparisons of failure modes as well as examinations of strain gage data were used to monitor coupon quality and consistency of testing procedures as described above. Drawings of typical fracture patterns were made for each coupon type.

After a cylinder test, fragments of the specimen were collected from the blast chamber and pieced together to determine the fracture path. Photographs as well as drawings were made of each cylinder. These were used to identify the primary fracture path as well as determine stiffening band effects on the failure. Strain gage data, used primarily for quality-control, was compared for similar specimens to ascertain specimen consistency.

CHAPTER 4

Results

Experimental results are presented herein along with predictions and correlations. The methodology developed by Graves [1,3], described in Chapter 2, was chosen to estimate cylinder failure stresses for this investigation. Previous work has proven that this semi-empirical method can be used to accurately predict the fracture pressures of quasi-isotropic $[0_f/45_f]_s$ fabric cylinders with slits. Unnotched coupons were used to determine tensile properties of the $[90/0/\pm45]_s$, $[\pm45/90]_s$, and $[\pm45/0]_s$ laminates. Notched coupon data was used to determine the fracture parameters H_c and the corresponding Mar-Lin correlations for each laminate type. The Mar-Lin correlations were combined with the proper curvature correction terms to yield failure pressure predictions for all cylinder types. Cylinder failure data was collected and fracture paths were recorded.

This predictive methodology was applied to the quasi-isotropic $[90/0/\pm45]_s$ cylinders to determine whether it could be extended to encompass tape cylinders as well. Application of the predictive methodology to the structurally anisotropic tape cylinders was not expected to yield accurate results, due to the bending-twisting coupling inherent to the laminates. The methodology was used here mainly to estimate failure pressures; agreement of the results with the predicted values was not anticipated. The relationship between the experimental data with the isotropic and orthotropic analytic predictions was used as a basis for comparison of quasi-isotropic and anisotropic laminates.

4.1 Coupon Results

Notched and unnotched coupon data is presented for $[90/0/\pm45]_s$, $[\pm45/90]_s$, and $[\pm45/0]_s$ laminates. Data includes failure loads, strain gage results, fracture modes and fracture paths, fracture parameters and failure stress correlations.

Fracture stresses of the notched coupons were correlated via the Mar-Lin equation. The Mar-Lin equation is restated below.

$$\sigma_f = H_c(2a)^{-m} \qquad\qquad (4.1)$$

where the variables are defined in the following manner:

σ_f = far-field failure stress of the coupon (MPa)

H_c = composite fracture parameter (MPa * $(mm)^m$),

$2a$ = length of the notch perpendicular to the loading direction (mm)

m = value of the stress singularity at the bimaterial interface

As stated in Chapter 2, the value of m has been calculated to be 0.28 for graphite/epoxy. The fracture parameter, H_c, was calculated individually for each coupon, and the average value for the laminate was used to determine the Mar-Lin curve relating failure stress to slit length.

4.1.1 $[90/0/\pm45]_s$ Coupons

Unnotched $[90/0/\pm45]_s$ coupon data was acquired to determine the tensile properties as well as the unnotched failure stress of the laminate. Average unnotched failure stress, determined from three specimens, is 621 MPa with a coefficient of variation of 10.6 %. Individual failure stresses are tabulated in Appendix A.

The fracture path in the unnotched coupons extends across the specimens in a relatively straight line. The clean fracture of the ±45° and 0° plies transverse to the loading direction indicates that the primary failure mode was fiber-dominated. Some delamination and splitting of the outer 90° plies is apparent, extending up to 25 mm towards either end of the specimen from the main fracture path. In addition, splitting of the laminate along the ±45° interface can be seen in the fracture region for some specimens. A post-test photograph of a representative unnotched [90/0/±45]$_s$ coupons is shown in Figure 4.1.

Examination of longitudinal and transverse strain gage data shows that stress-strain and strain-strain curves are linear for at least the first third of each test. The linear region of the curve was determined visually from a graph of the data. Strain gage data from this region was used to determine the experimental longitudinal modulus and major Poisson's ratio of the laminate. Laminate properties were calculated using a least squares linear curve fitting program. The longitudinal modulus, E_L, was determined from the initial slope of the stress/longitudinal strain curve shown in Figure 4.2. The average longitudinal modulus, determined from two specimens, is 52.3 GPa. The value calculated from the material properties shown in Table 3.1 is 55.5 GPa, only slightly higher than the experimental result. The longitudinal/transverse strain curve shown in Figure 4.3 was used to determine the Poisson's ratio of the laminate. The experimental data yielded a value of 0.29, while the value calculated from the material properties is 0.30. All values for individual coupons are presented in Appendix A. Good agreement between calculated and experimentally-determined laminate properties indicates that the laminate quality was good.
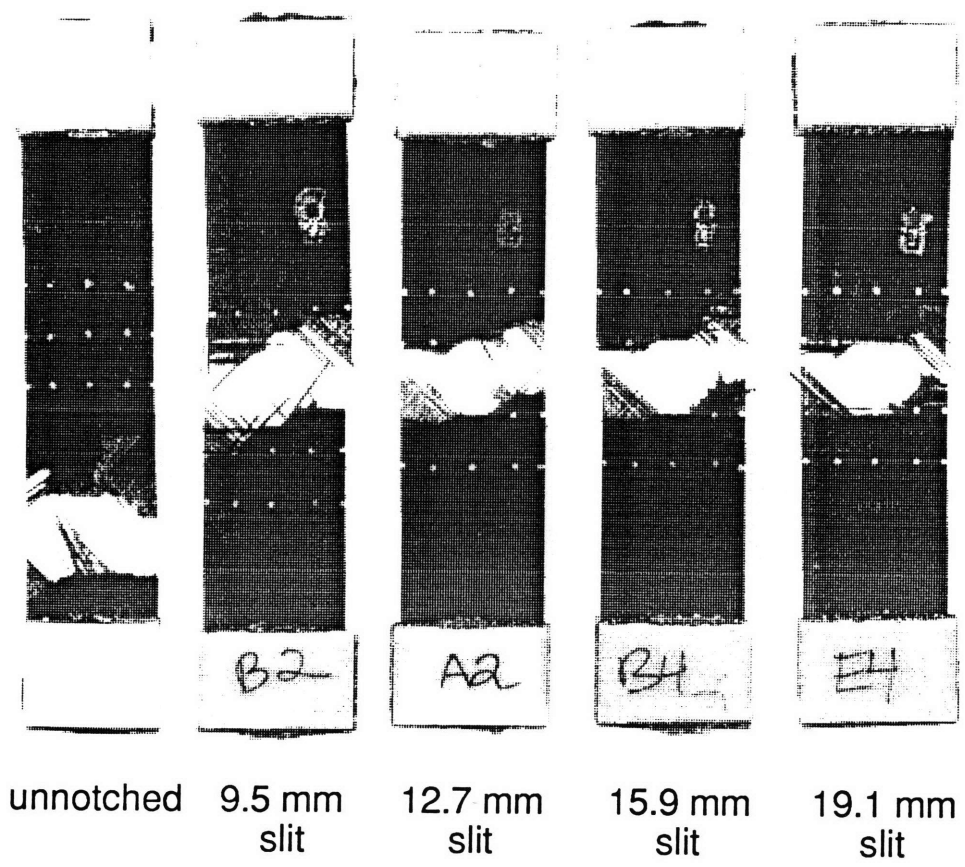
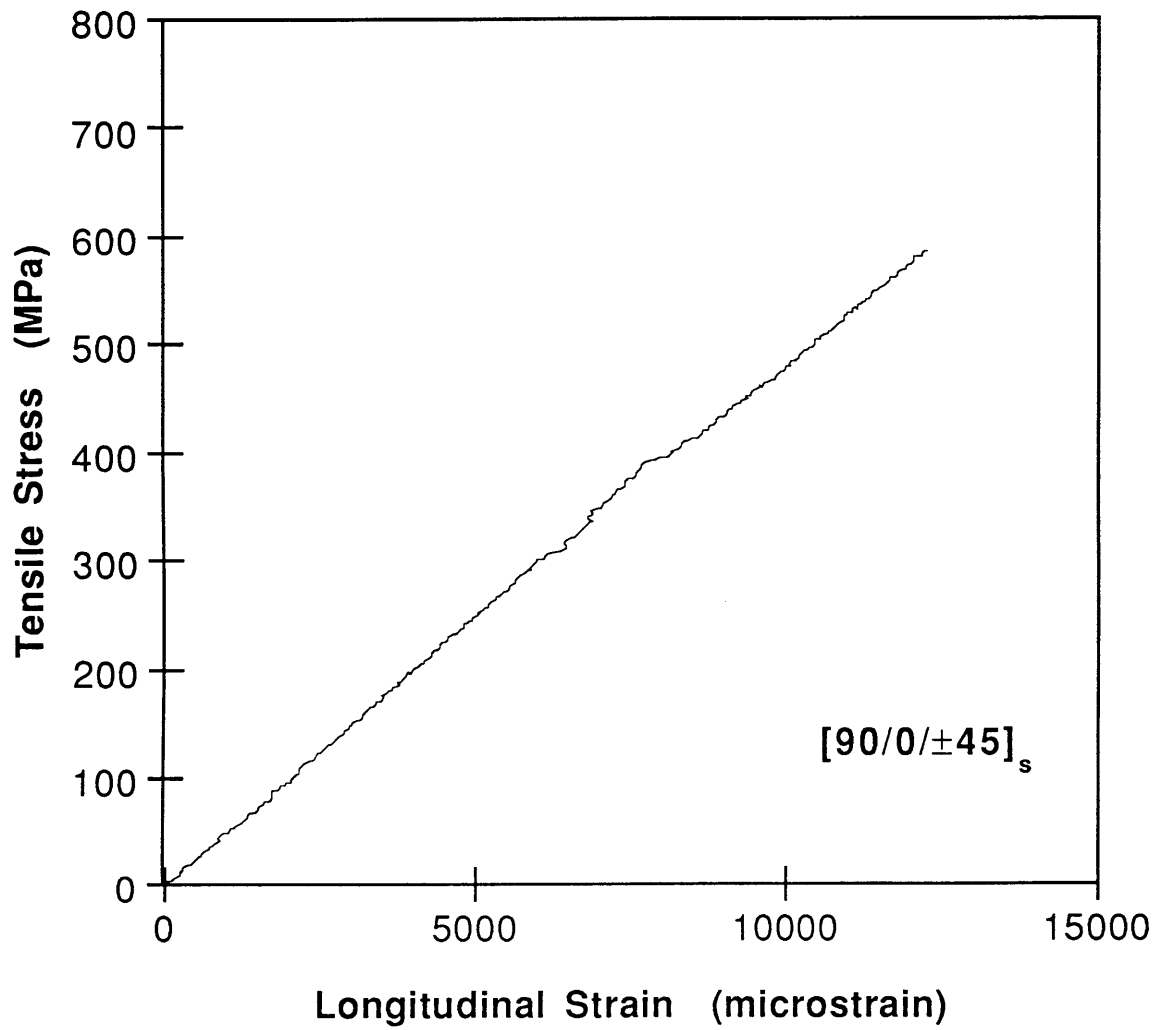Figure 4.1 Photograph of Fractured $[90/0\pm45]_s$ Coupons.

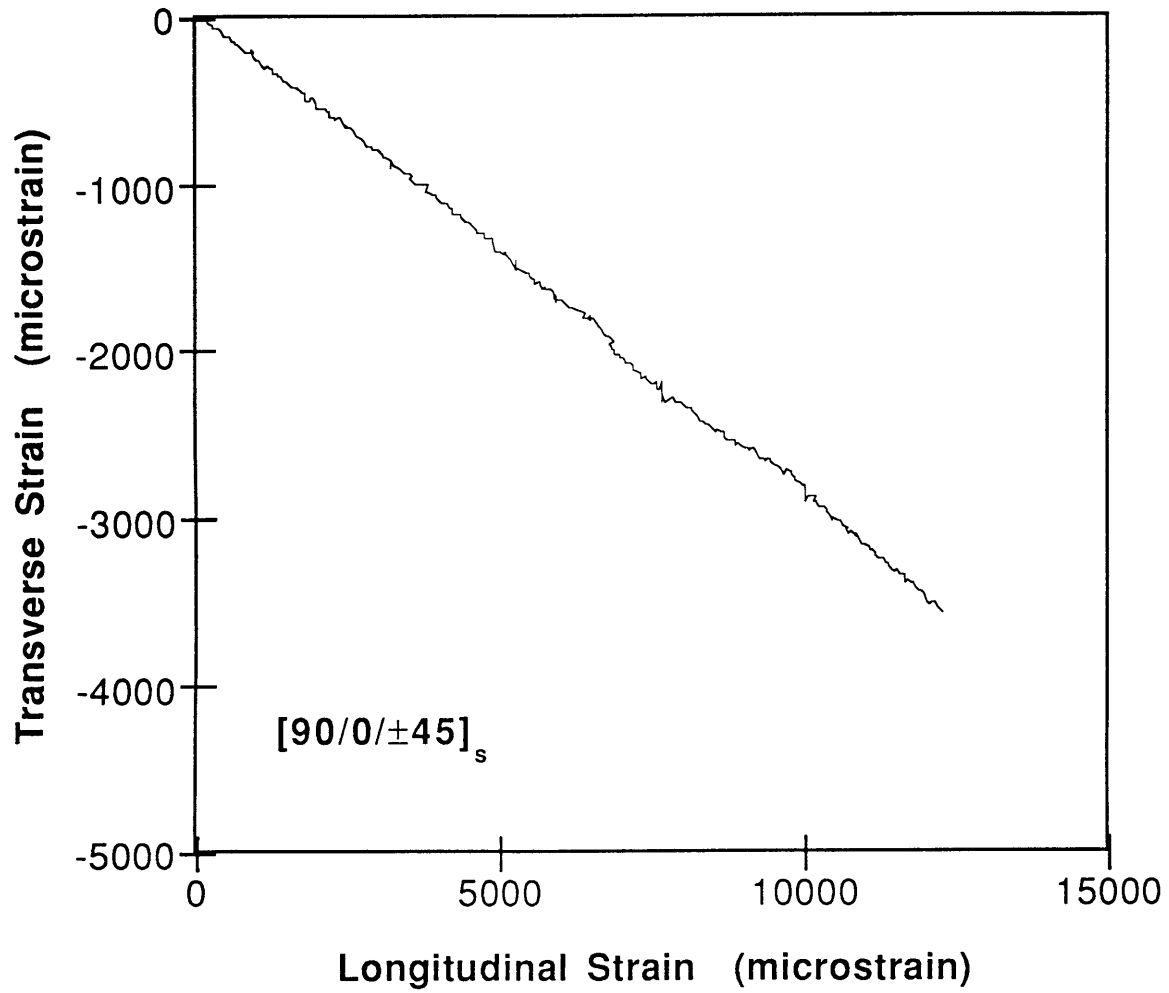Figure 4.2 Tensile Stress versus Longitudinal Strain for Typical Unnotched
[90/0/±45]ₛ Coupon.

Figure 4.3 Transverse Strain versus Longitudinal Strain for Typical
Unnotched [90/0/±45]$_s$ Coupon.

Average fracture stresses and coefficients of variation for the notched specimens are shown in Table 4.1. Individual fracture stresses are tabulated in Appendix A. Nominal slit sizes, coupon widths, and laminate thicknesses were used to calculate the fracture parameter H_c. The average value for the $[90/0/\pm45]_s$ notched coupons is 664 MPa*mm$^{0.28}$, with a coefficient of variation of 4.2%. Values for individual specimens are given in Appendix A. The Mar-Lin correlation was determined using this value, and is shown with coupon data in Figure 4.4. Scatter of the data is small.

In all cases, fracture originated at the slit ends and propagated outward to the edges of the specimens. A photograph of representative notched specimens is shown in Figure 4.1. Fracture paths in the specimens with 9.5 mm slits travelled along the $\pm45°$ direction halfway to the coupon edge from the slit ends before turning to $90°$ and running parallel to the slit. The $0°$ fibers, aligned with the tensile load, broke cleanly along the fracture path. The fibers oriented at $90°$ did the same, but secondary delamination from the surface of the coupon was observed. The angled fibers running along the portion of the fracture path at $\pm45°$ separated with little delamination, but those perpendicular to the fracture path were pulled out and broke raggedly. As with the unflawed coupons, delamination between $\pm45°$ plies extended towards the loading tabs from the line of fracture.

Fracture of the coupons with larger slit sizes was similar. Fibers in the $0°$ direction broke along the fracture path, and the $0°$ plies exhibited little splitting. The $\pm45°$ fibers seemed to pull out of the coupon on either side of the slit, indicating that failure was due primarily to fracture of the $0°$ fibers. As slit size increased, the fracture path was oriented more in the $90°$ direction than in the $45°$ direction.

Table 4.1 Fracture Data for $[90/0/\pm45]_s$ Coupons

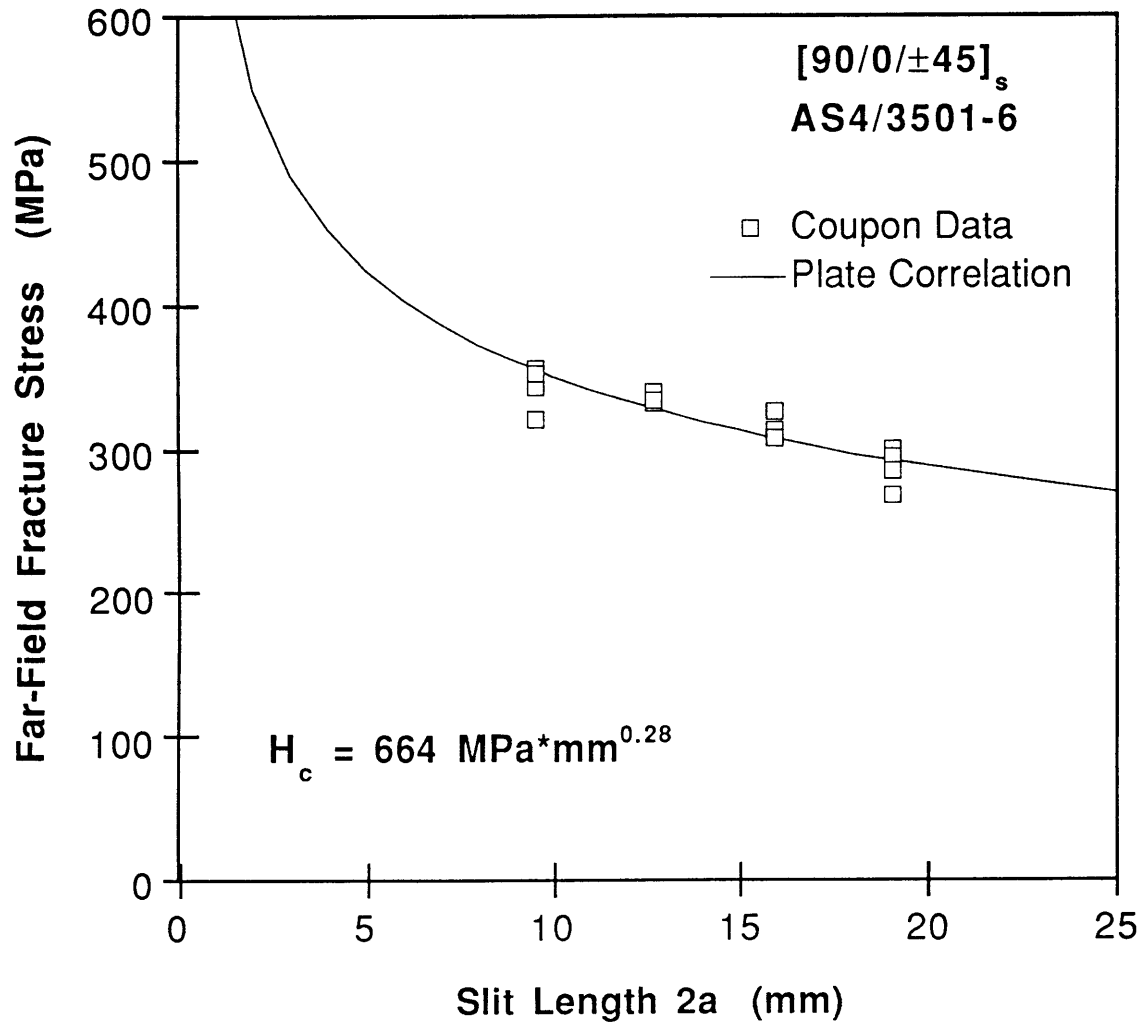| Nominal Slit Length [mm]	Average Fracture Stress [MPa]	Average H_c [MPa*mm^m]
unnotched	621 (10.6%)[a]	--
9.5	342 (4.8%)	643 (4.7%)
12.7	334 (1.1%)	680 (1.2%)
15.9	314 (2.7%)	681 (2.7%)
19.1	286 (5.0%)	653 (5.0%)

[a] numbers in parentheses are coefficients of variation

Figure 4.4 Notched [90/0/±45]s Coupon Results and Fracture Stress
Correlation Curve.

Longitudinal strain gage data for all specimens is similar. Strains are linear for at least the first quarter of each test, and stress/strain curves were similar to those found for the unnotched coupons. A typical stress/longitudinal strain curve is shown in Figure 4.5. Consistency amongst notched coupon strain data and similarity of notched data to unnotched results indicate that the laminate quality of the notched coupons was good.

4.1.2 [±45/0]$_s$ Coupons

Unnotched coupon data was collected from eight specimens as indicated in Table 3.2. The average fracture stress of the unnotched [±45/0]$_s$ coupons is 743 MPa, with a coefficient of variation of 13.4%. Values for individual specimens are tabulated in Appendix A.

Fracture of the [±45/0]$_s$ coupons is much more ragged than that of the [90/0/±45]$_s$ specimens. Fracture paths in the unnotched coupons are generally oriented across the specimen with some deviations in the ±45° directions. Fibers in the 0° direction broke cleanly, while the external ply of 45° fibers fractured raggedly and delaminated from the -45° fibers directly underneath in secondary failure. No delamination of the 0° plies or between 0° and 45° plies is apparent. A post-test photograph of a representative unnotched coupon is shown in Figure 4.6.

As with the [90/0/±45]$_s$ specimens, strain gage data from the [±45/0]$_s$ coupons was used to monitor the quality of the laminates. Representative stress-strain and strain-strain graphs are shown in Figures 4.7 and 4.8. As with the unnotched quasi-isotropic coupons, the curves remain linear for the first third of each test. The modulus and Poisson's ratio of the laminate are determined from a least squares linear curve fit to the linear
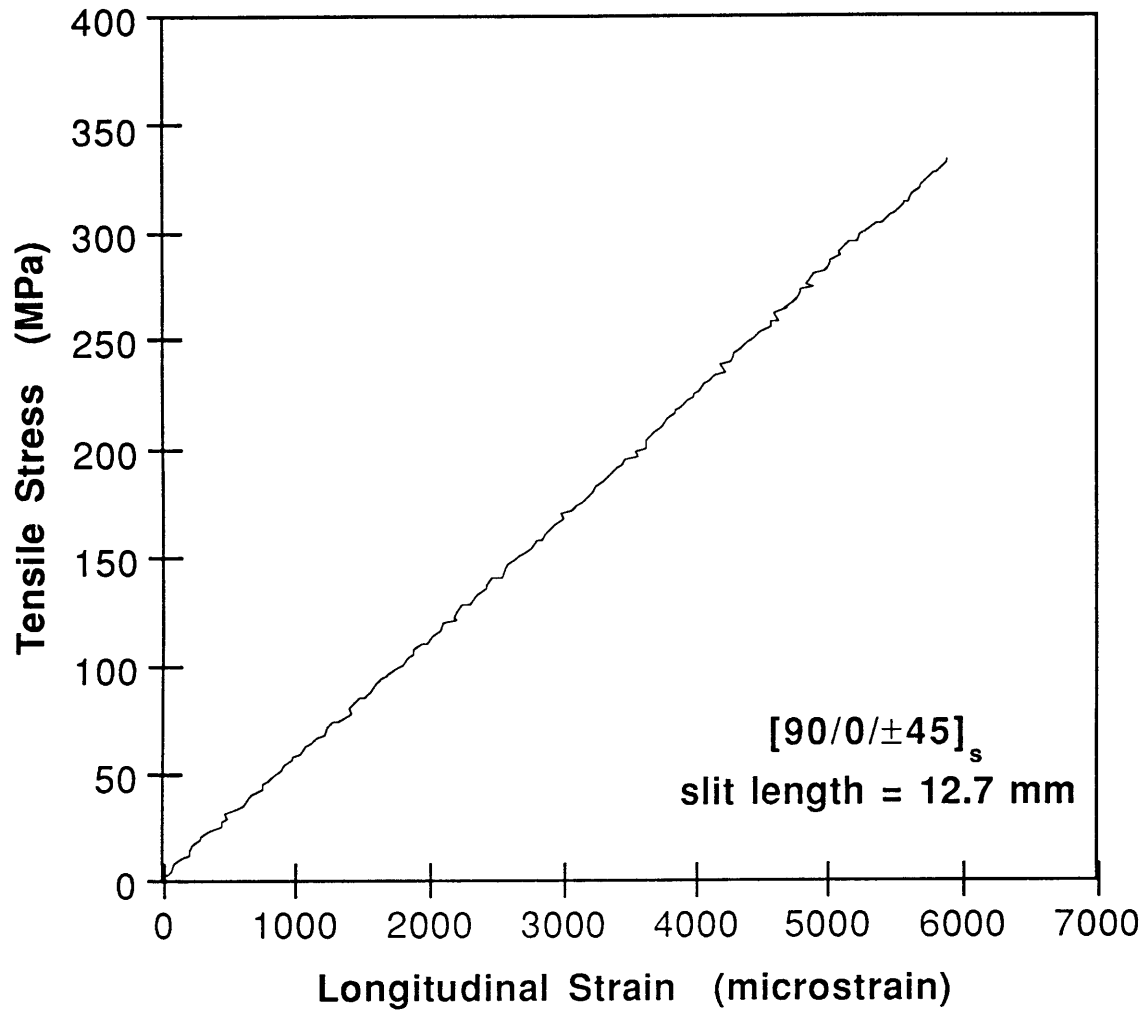
Figure 4.5 Tensile Stress versus Longitudinal Strain for Typical Notched
         [90/0/±45]s Coupon.

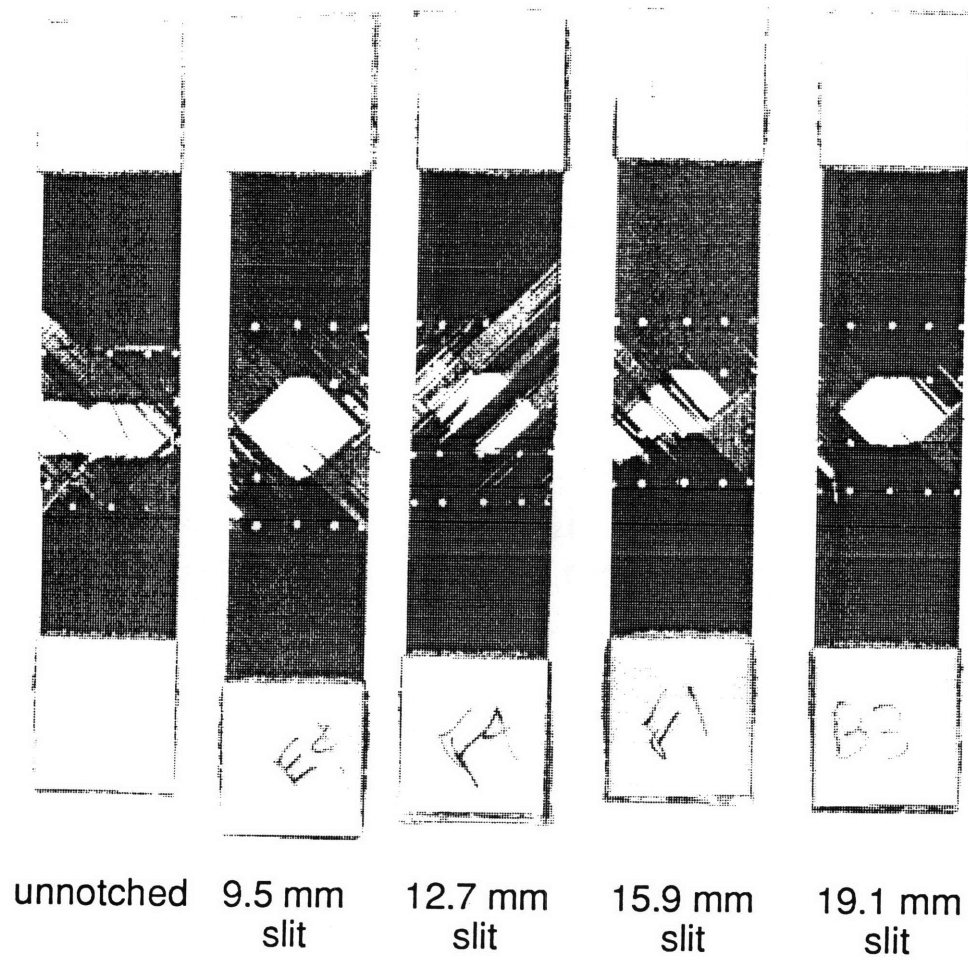Figure 4.6 Photograph of Fractured [±45/0]$_s$ Coupons.
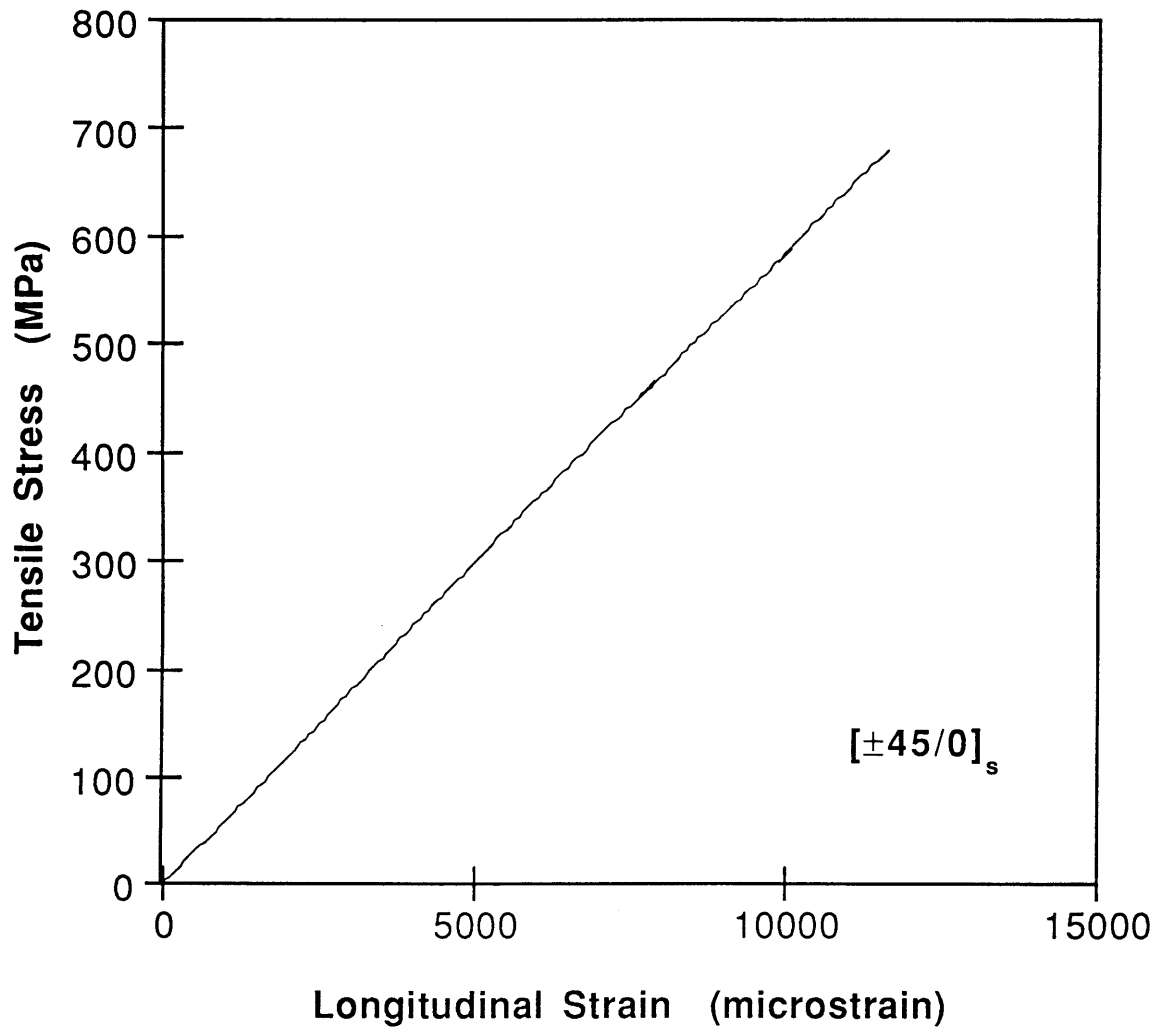
Figure 4.7 Tensile Stress versus Longitudinal Strain for Typical Unnotched [±45/0]s Coupon.
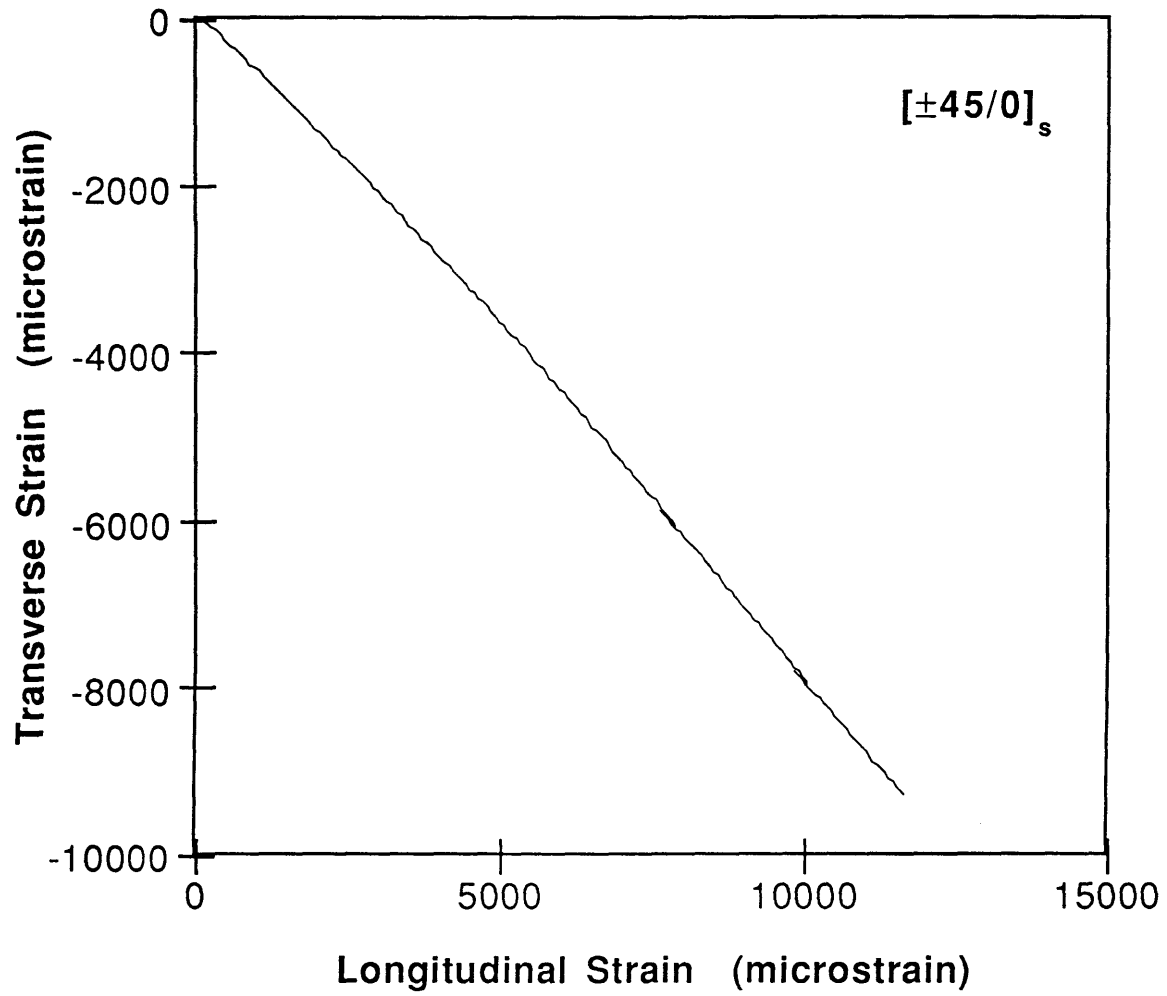
Figure 4.8 Transverse Strain versus Longitudinal Strain for Typical
Unnotched [±45/0]$_s$ Coupon.

region of the strain data. The experimental longitudinal modulus, determined from the stress/longitudinal strain curves of eight specimens, is 61.5 GPa with a coefficient of variation of 4.1%. This result agrees closely with the value of 61.8 GPa calculated from the material properties of the AS4/3501-6 graphite/epoxy tape. Linear curve fits to the transverse/longitudinal strain curves yield a Poisson's ratio of 0.70 with a 5.0% coefficient of variation. This result agrees with the calculated value of 0.69. Close correlation between these calculated and experimental laminate properties indicates that the quality of the laminates was good.

Notched fracture stress values, averaged for each notch size, are given with coefficients of variation in Table 4.2. Individual specimen data is tabulated in Appendix A. Correlation of the far-field fracture stresses of the specimens is accomplished using the Mar-Lin equation as described previously. The value for the fracture parameter H_c, averaged from all notched coupons, is 715 MPa*mm^m, with a coefficient of variation of 5.6%. A graph of the stress correlation and the notched coupon data is shown in Figure 4.9. Although the data exhibits considerably more scatter than that of the $[90/0/\pm45]_s$ coupons, the correlation remains good.

Fracture of $[\pm45/0]_s$ coupons with notches originated at the slit ends. A photograph of typical fractured specimens is shown in Figure 4.6. Note that the fractures of the notched and unnotched specimens are similar. The fracture path is typically oriented at a -45° angle, perpendicular to the direction of the surface fibers, from the slit tip to the edge of the laminate. Secondary delamination of the external 45° plies along the fracture path results in a 'butterfly' fracture pattern extending from both ends of the slit to the edges of the laminate. No delamination of internal plies is visible.

Table 4.2 Fracture Data for $[\pm 45/0]_s$ Coupons

Nominal Slit Length [mm]	Average Fracture Stress [MPa]	Average H_c [MPa*mm^m]
unnotched	743 (13.4%)[a]	--
9.5	392 (4.2%)	754 (5.0%)
12.7	344 (3.9%)	709 (2.4%)
15.9	311 (6.5%)	680 (6.1%)
19.1	313 (4.8%)	718 (4.1%)

[a] numbers in parentheses are coefficients of variation
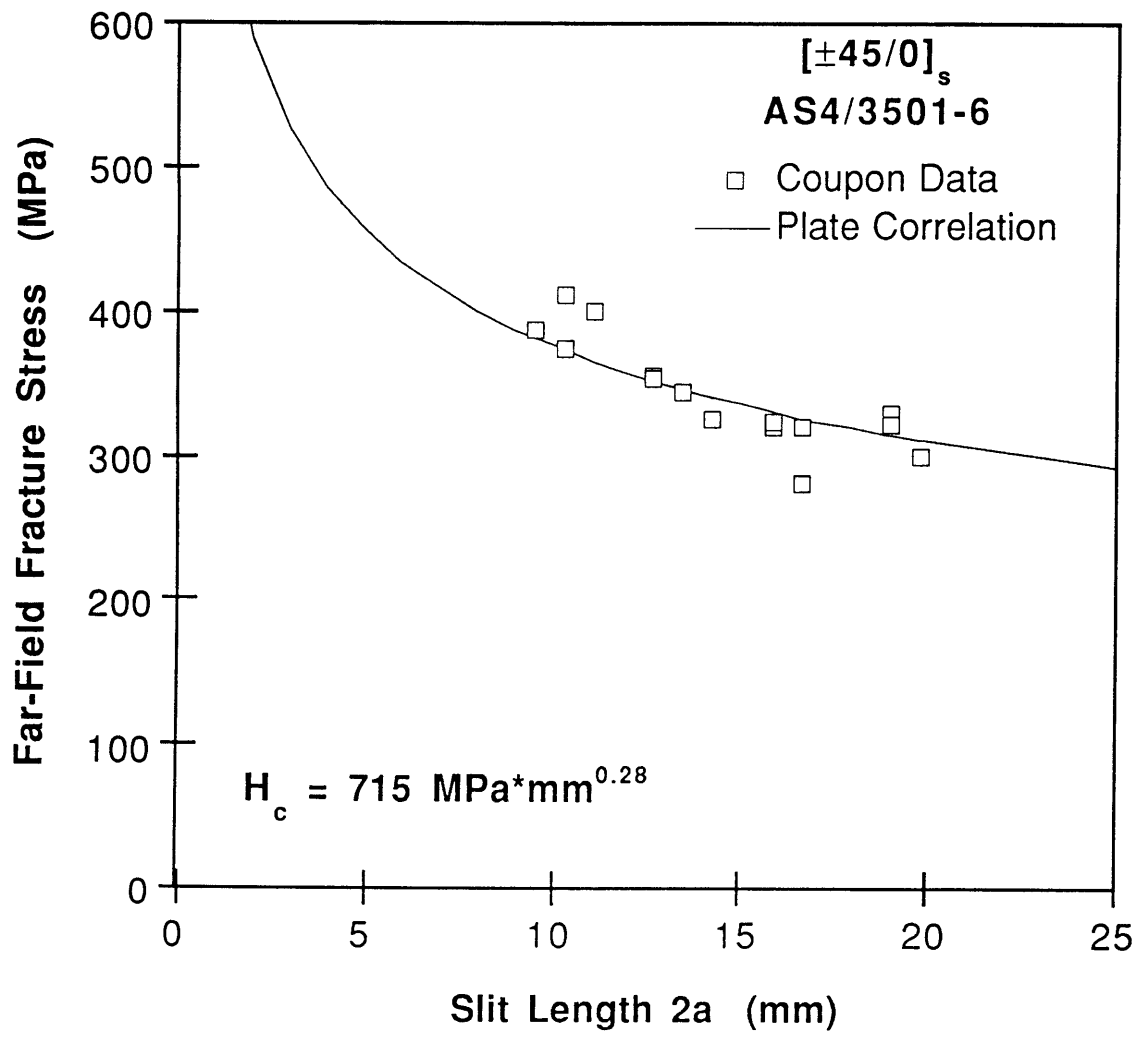
Figure 4.9 Notched [±45/0]ₛ Coupon Results and Fracture Stress
Correlation Curve.

Specimens with larger slits also exhibit some fracture along the 0° fibers; generally this is apparent close to the edges of the specimen.

Longitudinal far-field strain gage data collected from the notched specimens is similar for all coupons. A typical stress/strain graph, shown in Figure 4.10, indicates that the strain is linear for the first quarter of each test. Notched and unnotched coupons exhibited similar stress/strain curves, thus ensuring that the laminates were all of the same quality.

4.1.3 [±45/90]$_s$ Coupons

Eight unnotched [±45/90]$_s$ specimens were tested in tension. Average far-field fracture stress for these coupons is 224 MPa, with a coefficient of variation of 3.9%. As expected, this value is much lower than that found for the [±45/0]$_s$ specimens. Individual coupon data is tabulated in Appendix A.

A post-test picture of a representative unnotched [±45/90]$_s$ specimen is shown in Figure 4.11. Fracture of the unnotched coupons is visible on the surface in the +45° direction. A band, approximately 10 mm wide, of fibers oriented in this direction has delaminated completely from the underlying -45° ply. This is apparent on both sides of the specimen. While showing little fiber breakage, the -45 plies exhibit matrix cracking along the line of principal fracture defined by the external +45° ply. Delamination of internal 90° plies from each other and from the adjacent -45° fibers is apparent at the edges of the specimen. Originating at the ends of the primary fracture, these delaminations extend to the fiberglass loading tabs.

Stress-strain and strain-strain graphs for the [±45/90]$_s$ laminates are presented in Figures 4.12 and 4.13. As for the [±45/0]$_s$ coupons, the strains are linear with stress for the first third of the tests. The longitudinal modulus, determined from the slope of the graphically-determined linear
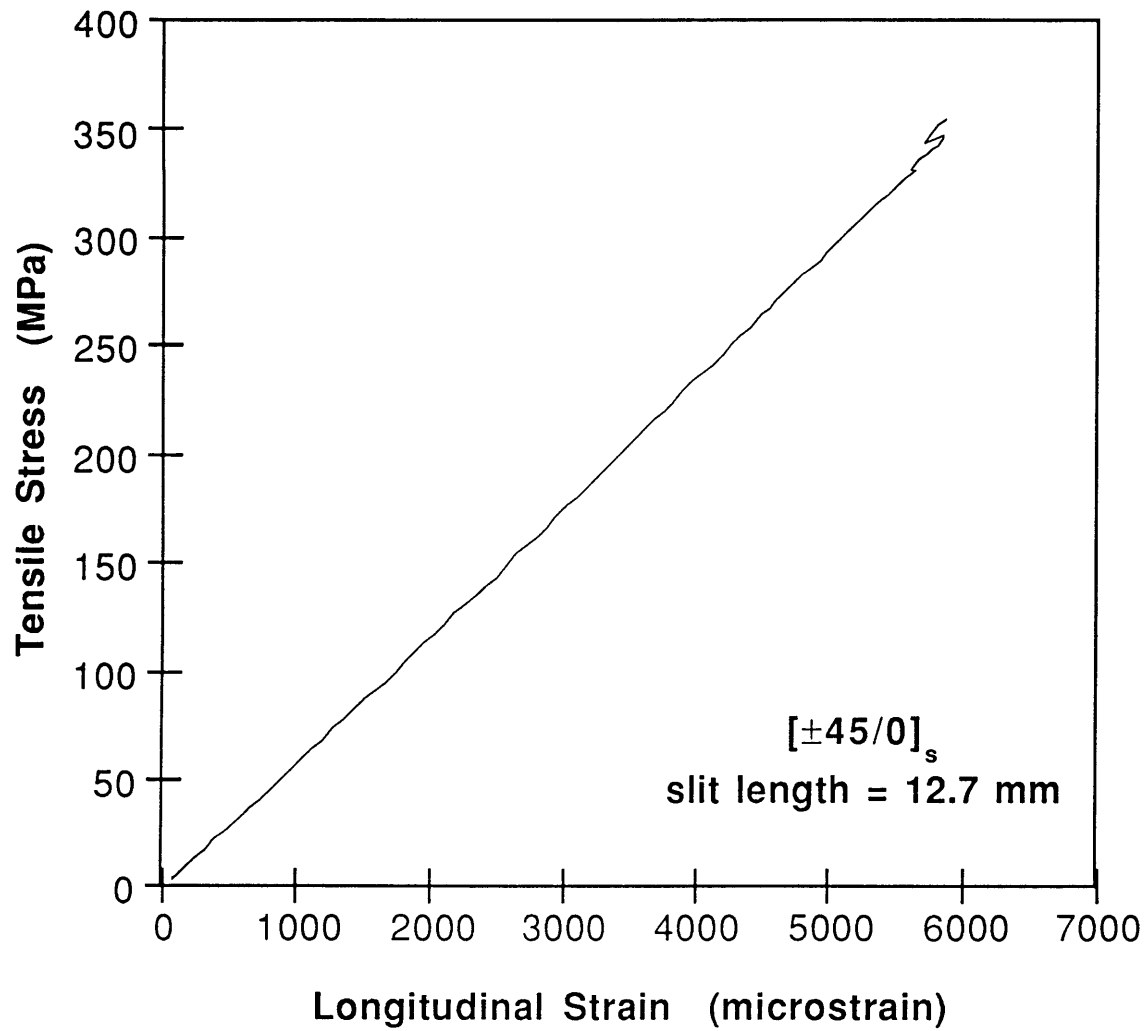
Figure 4.10 Tensile Stress versus Longitudinal Strain for Typical Notched [±45/0]$_s$ Coupon.

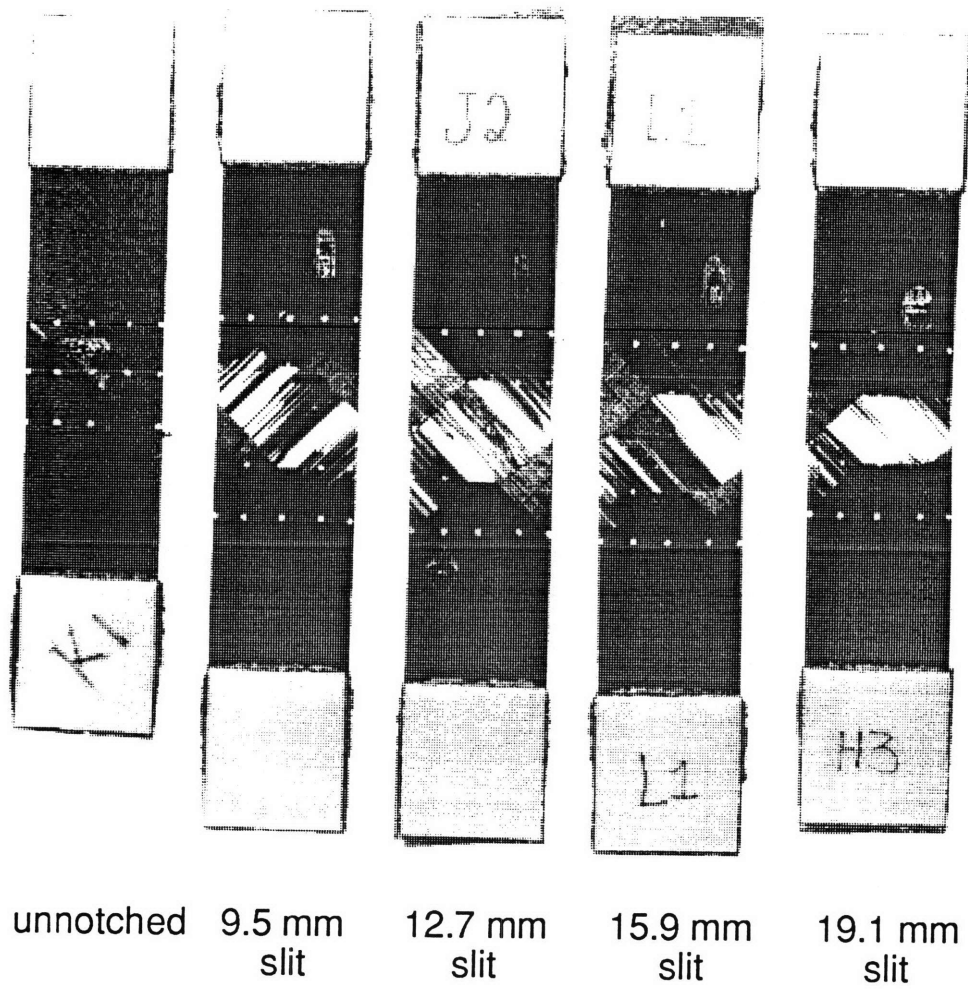| unnotched | 9.5 mm slit | 12.7 mm slit | 15.9 mm slit | 19.1 mm slit |

Figure 4.11 Photograph of Fractured [±45/90]$_s$ Coupons.
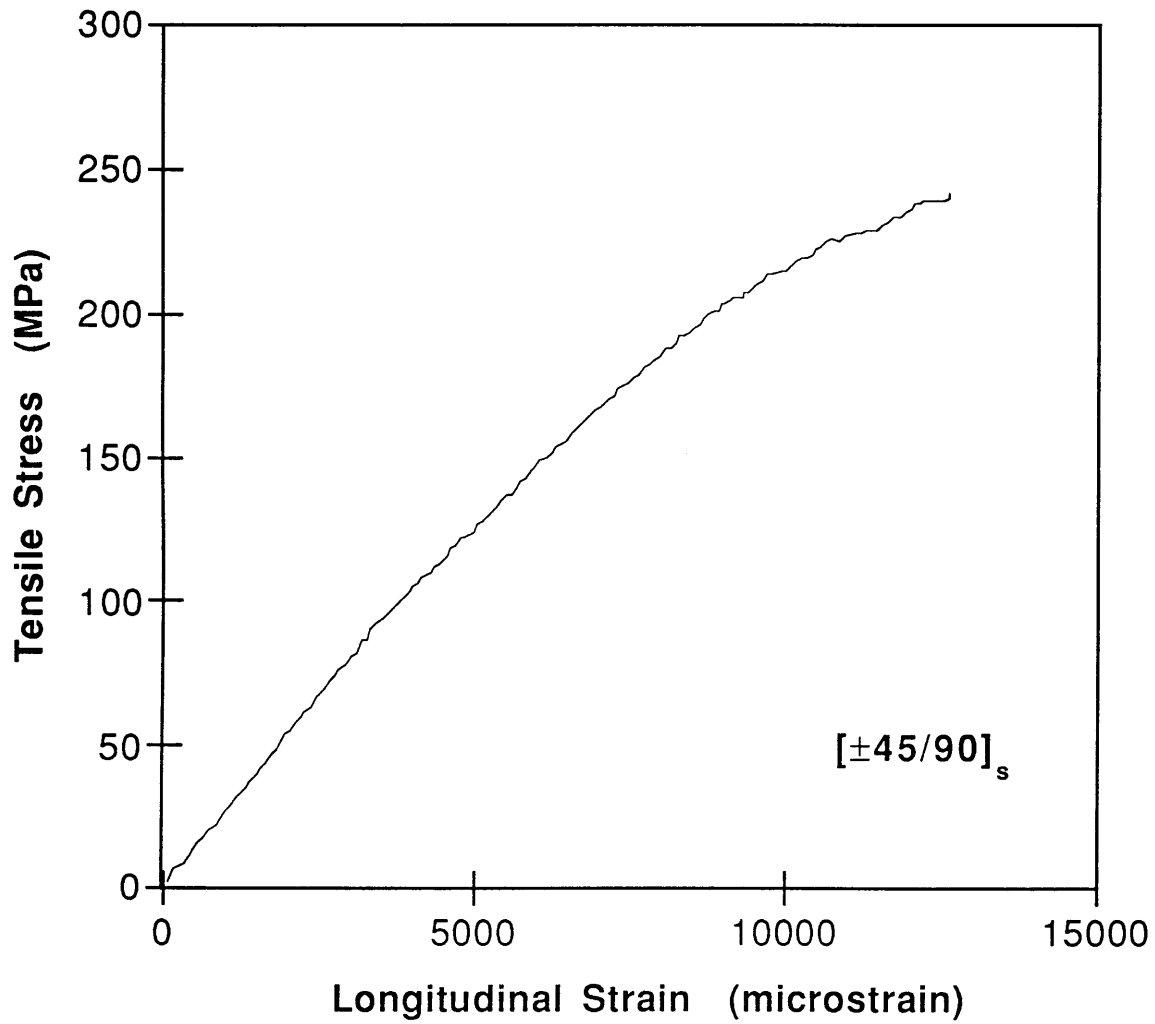
Figure 4.12 Tensile Stress versus Longitudinal Strain for Typical
Unnotched [±45/90]s Coupon.
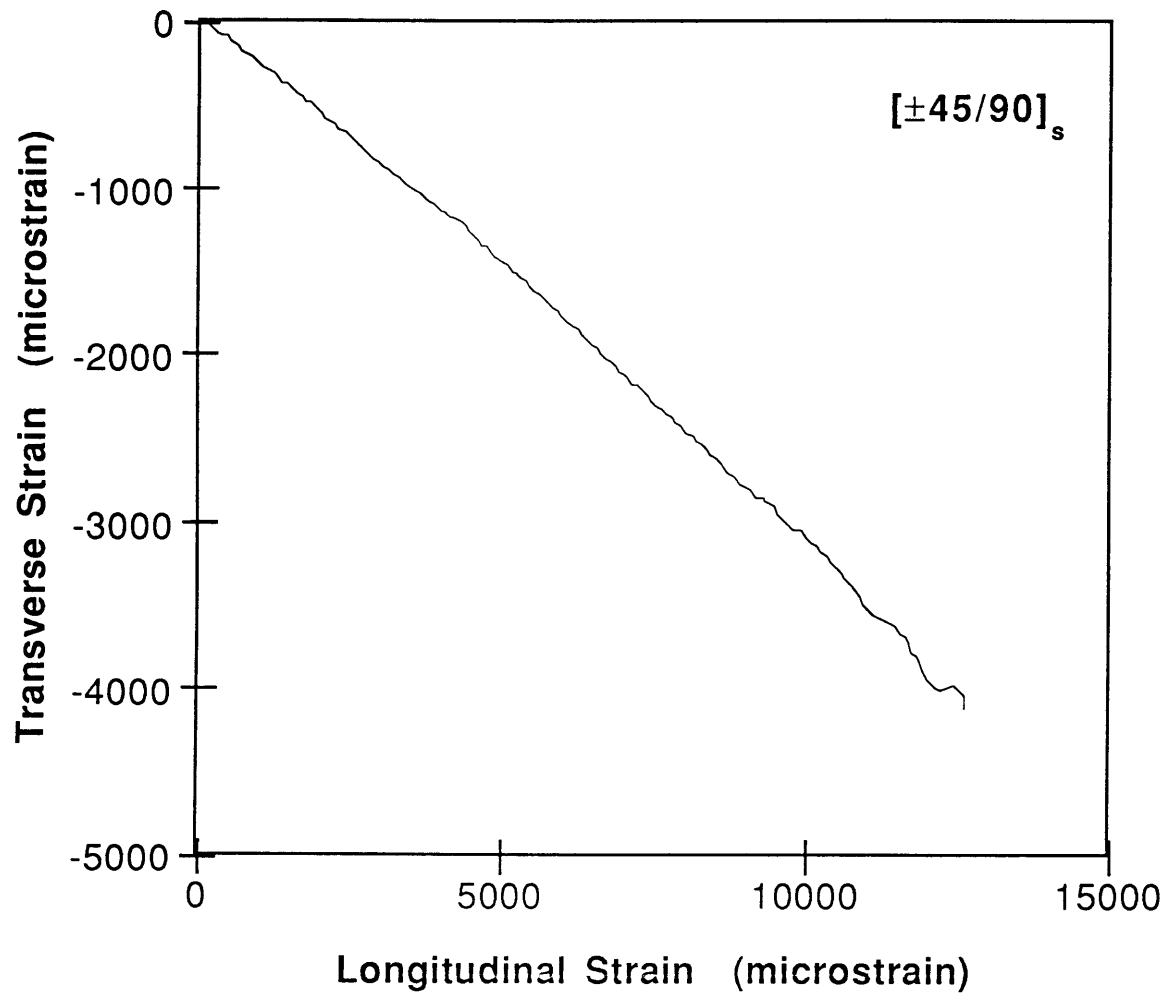
Figure 4.13 Transverse Strain versus Longitudinal Strain for Typical
Unnotched [±45/90]$_s$ Coupon.

regions of the stress/longitudinal strain curves, averages to 26.9 GPa with a coefficient of variation of 2.5%. This value agrees closely with the calculated longitudinal modulus of 26.7 GPa. The average of the experimentally-determined Poisson's ratios of the eight specimens is 0.30 with a 7.7% coefficient of variation. The Poisson's ratio calculated from material properties is 0.30, as well. Close agreement of these calculated and experimental laminate properties is an indication that the specimens are of good quality.

Fracture stresses of the notched specimens, ranging from 189 MPa (19.1 mm slit) to 218 MPa (9.5 mm slit) were only slightly lower than those found for the unnotched coupons. Average fracture stress values for each notch size are given in Table 4.3 with coefficients of variation. The Mar-Lin equation is used to correlate the coupon fracture stresses. Values for the composite fracture parameter, H_c, are determined from coupon failure stresses and nominal specimen dimensions. The average value for the notched specimens is 422 MPa*mm$^{0.28}$, with a coefficient of variation of 4.3%. The Mar-Lin correlation curve resulting from this average is presented in Figure 4.14 along with the coupon data. Numerical fracture data is presented in Appendix A for individual coupons.

In all cases, fracture originates at the ends of the slit. A photograph of fractured notched coupons is shown in Figure 4.11. Examination of the post-test notched specimens indicates that the fracture modes are not dominated by the delamination found in the unnotched coupons. In the notched coupons, the fracture path, which extends from the slit to the edges of the specimen, lies along the -45° direction. The internal -45° and 90° plies fracture cleanly along this line. The external +45° fibers exhibit matrix cracking and delamination from underlying plies in the region around the

Table 4.3 Fracture Data for Notched [±45/90]$_s$ Coupons

Nominal Slit Size [mm]	Average Fracture Stress [MPa]	Average H$_c$ [MPa*mm^m]
unnotched	224 (3.9%)[a]	--
9.5	218 (3.4%)	411 (3.5%)
12.7	205 (4.3%)	421 (5.2%)
15.9	197 (4.3%)	427 (4.1%)
19.1	189 (4.6%)	431 (4.5%)

[a] numbers in parentheses are coefficients of variation
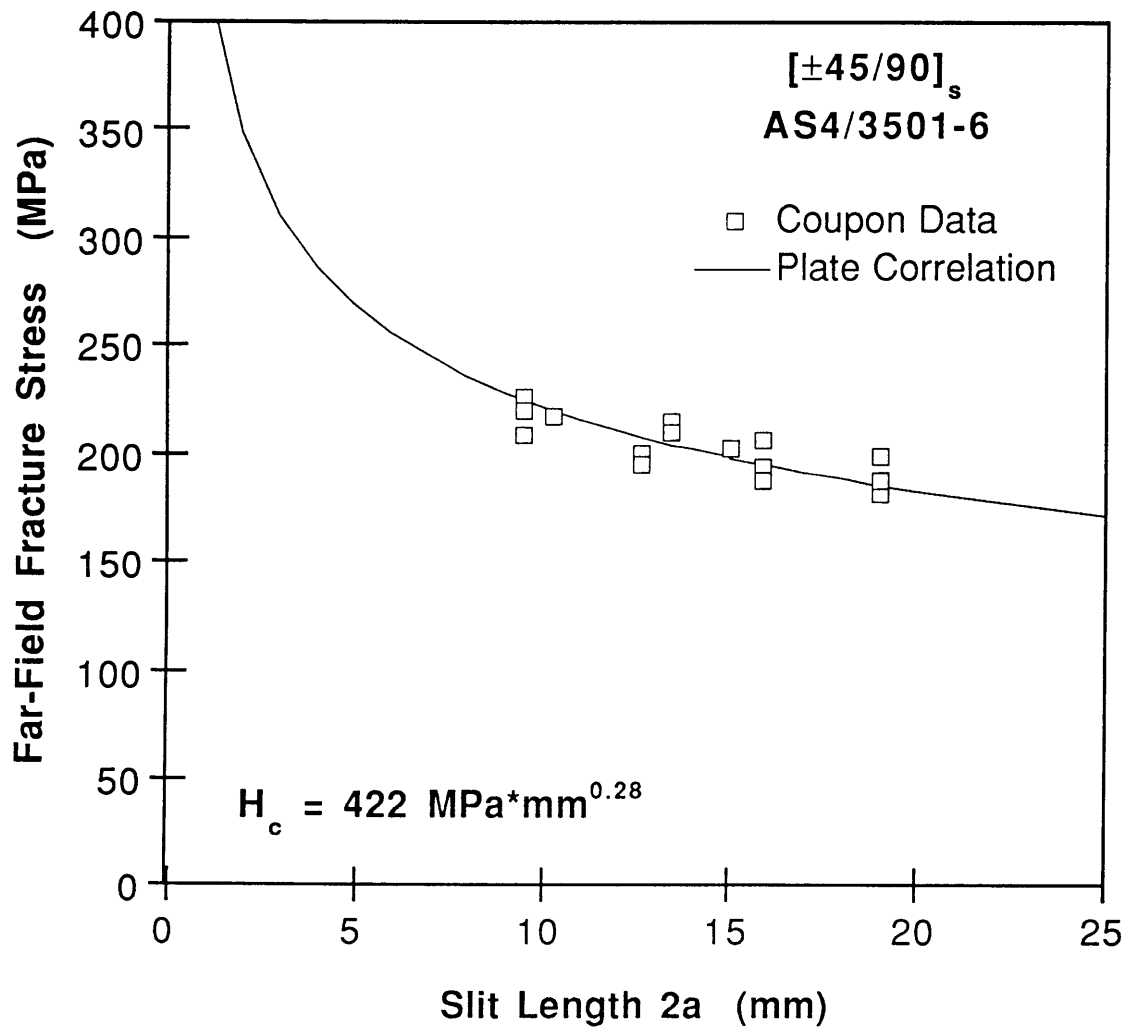
Figure 4.14 Notched [±45/90]ₛ Coupon Results and Fracture Stress
Correlation Curve.
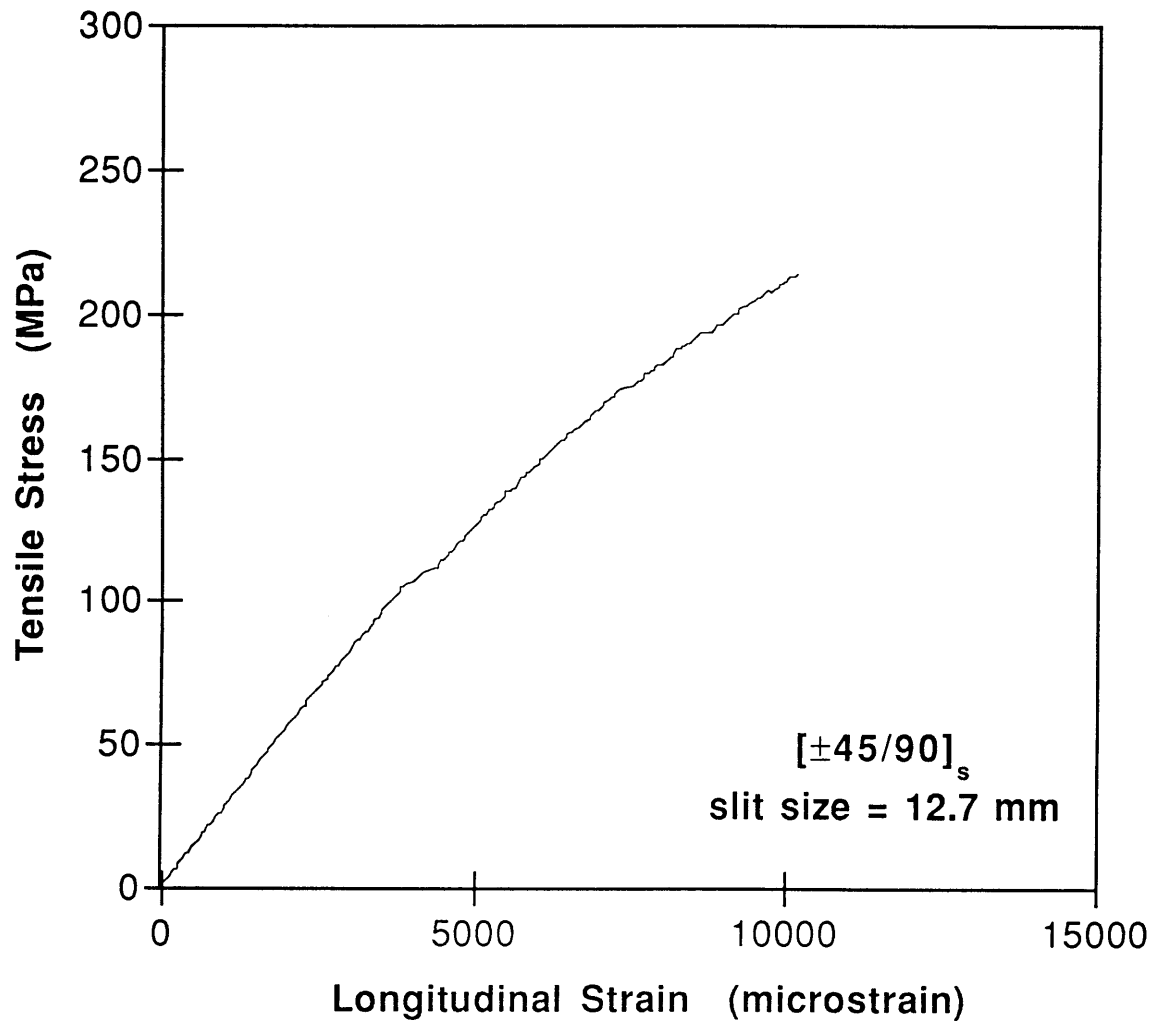
Figure 4.15 Tensile Stress versus Longitudinal Strain for Typical Notched [±45/90]$_s$ Coupon.

primary fracture. This secondary delamination of the surface plies originates at the -45° line of fracture and extends to the edges of the laminate in the +45° direction. A butterfly-shaped region of damage, similar to that found in the [±45/0]$_s$ notched specimens, results. Separation of the 90° plies from one another and from the -45° plies, originating at the fracture and extending a short distance to the loading tabs, is seen at the edges of some specimens.

A representative stress/longitudinal strain graph is shown in Figure 4.15 for the [±45/90]$_s$ notched coupons. Strain data is linear for at least the first quarter of the test, and data compares well with that collected from unnotched specimens. Agreement indicates that laminate quality is uniform.

4.2 Cylinder Results

Notched cylinder data is presented for [90/0/±45]$_s$, [±45/0]$_s$, [±45/90]$_s$, and [0$_f$/45$_f$]$_s$ cylinders. Data includes final failure pressures, post-test photographs of the fractured cylinders, and sketches of the failure paths for individual specimens. Fracture pressure predictions determined from coupon data are presented to provide context for the experimental results.

The coupon far-field failure stress can be expressed in terms of internal cylinder pressure p,

$$\sigma_f = \frac{pr}{t} \tag{4.2}$$

and the Mar-Lin equation (4.1) can effectively be rewritten as

$$p = \frac{H_c t}{r}(2a)^{-m} \qquad (4.3)$$

In these equations, the radius r and wall thickness t of the cylinder are expressed in mm, and the internal pressure p in MPa. It should be noted that equations 4.2 and 4.3 do not include a curvature correction factor, but only express the far-field stress of a flat plate in terms of internal pressure, p, which, when applied to a cylinder, would cause that same extensional stress in the hoop direction.

As stated in Chapter 2, it has been proposed that the far-field circumferential failure stress of a cylinder with an axial slit can be related to the far-field failure stress of a notched coupon in uniaxial tension. The relationship can be expressed as the following quotient:

$$\sigma_{cyl} = \frac{\sigma_f}{K} \qquad (4.4)$$

where σ_{cyl} is the circumferential stress in the cylinder at failure, σ_f is the coupon failure stress, and K is the extensional stress intensity factor accounting for specimen geometry, loading conditions, and material behavior. This relationship may also be expressed in terms of cylinder pressure and the 'plate' pressure found in equation 4.3:

$$p_{cyl} = \frac{p}{K} \qquad (4.5)$$

where p_{cyl} is the internal pressure applied to the cylinder.

Values for the stress intensity factor K can be determined for both isotropic and specially orthotropic materials. While the isotropic 'shell

correction factor' can be written in closed form [21], the orthotropic one must be evaluated numerically [25].

The isotropic correction factor, K_i, is a function of slit length, cylinder geometry, and the Poisson's ratio of the laminate:

$$K_i = (1 + 0.317\lambda_i^2)^{0.5} \tag{4.6}$$

where the isotropic shell parameter λ_i can be expressed as

$$\lambda_i^2 = \frac{a^2[12(1 - v^2)]^{0.5}}{rt} \tag{4.7}$$

The thickness t and radius r of the cylinder are expressed in mm, the half-slit length a also in mm, and the Poisson's ratio of the laminate as v. Since the major and minor Poisson's ratios are different for the anisotropic cylinder, a mean value is used instead. This is calculated as the square root of the product of these laminate properties. Given a specific cylinder geometry, K_i can be expressed as a continuous function of slit length. The result is then applied to equation 4.4 or 4.5 to determine the predicted circumferential failure stress or failure pressure of the quasi-isotropic cylinders.

The orthotropic stress intensity factor, K_o, is a function of the orthotropic shell parameter λ_o, and the cylinder radius and thickness.

$$K_o = F(\lambda_o, r, t) \tag{4.8}$$

The orhtotropic shell parameter can be expressed in terms of material properties and specimen geometry:

$$\lambda_o^4 = \frac{12a^4(1\text{-}v^2)}{\delta^2 t^2 r^2} \qquad (4.9)$$

where a is the half-slit length in mm, r and t are the cylinder radius and thickness in mm, v^2 is the product of the major and minor Poisson's ratios, and the orthotropy parameter, δ, is defined as

$$\delta^4 = \frac{E_L}{E_T} = \frac{v_{LT}}{v_{TL}} \qquad (4.10)$$

Krenk [25] has numerically determined the value of $K_o(\lambda_o)$ for a discrete number of cylinder radius/thickness ratios. For the purpose of this investigation, the K_o values for the proper r/t ratio are found via linear interpolation of Krenk's numerically-presented results. The resulting series of K_o values can be applied to equations 4.4 and 4.5 to determine the expected cylinder pressures and circumferential stresses as before. It should be noted, however, that this correction factor is for specially orthotropic materials, and is not necessarily applicable to the structurally anisotropic cylinders tested in this investigation. Therefore, agreement between experimental data and predicted values is not expected to be as good as that between the quasi-isotropic cylinders and the isotropic shell prediction.

4.2.1 [90/0/±45]$_s$ Cylinders

Failure pressure prediction for the quasi-isotropic [90/0/±45]$_s$ cylinders was determined with the appropriate coupon data. A graph of failure pressure versus slit size is presented in Figure 4.16, and the data is presented numerically in Table 4.4. The graph includes the Mar-Lin correlation curve determined from the [90/0/±45]$_s$ coupons as well as the corrected shell prediction for the quasi-isotropic cylinders. The coupon data, determined for slit sizes in the range of 9.5 to 19.1 mm, is not shown. Comparison of the experimental cylinder failure pressures and the predicted curve indicates that, for the larger slit sizes, the predictive methodology is accurate. However, the experimentally-determined failure pressure of the cylinder with the 12.7 mm slit is not only much higher than the predicted curve, but also greater than the coupon correlation found for the same slit size.

The fracture modes of the cylinders are examined individually in order of decreasing slit length. The unstiffened [90/0/±45]$_s$ specimen with a slit length of 50.8 mm fractured into three pieces at an internal pressure of 0.79 MPa. A photograph of the cylinder after failure is shown in Figure 4.17, and a schematic of the damage to the cylinder is shown in Figure 4.18. The main fracture extends from the slit ends to the endcaps, and ends roughly 45° circumferentially from the slit in either direction. This fracture path originates at either end of the slit and travels at -45° for approximately 100 mm in both directions. Bifurcation, or splitting of the fracture path into two separate paths, occurs on both sides of the slit at this point. The four paths, which run to the endcaps at roughly ±45°, are uneven. The paths curve from ±45° to 90°, and fracture occurs along 0°, 90°, and ±45° directions. A secondary fracture, originating at the main fracture
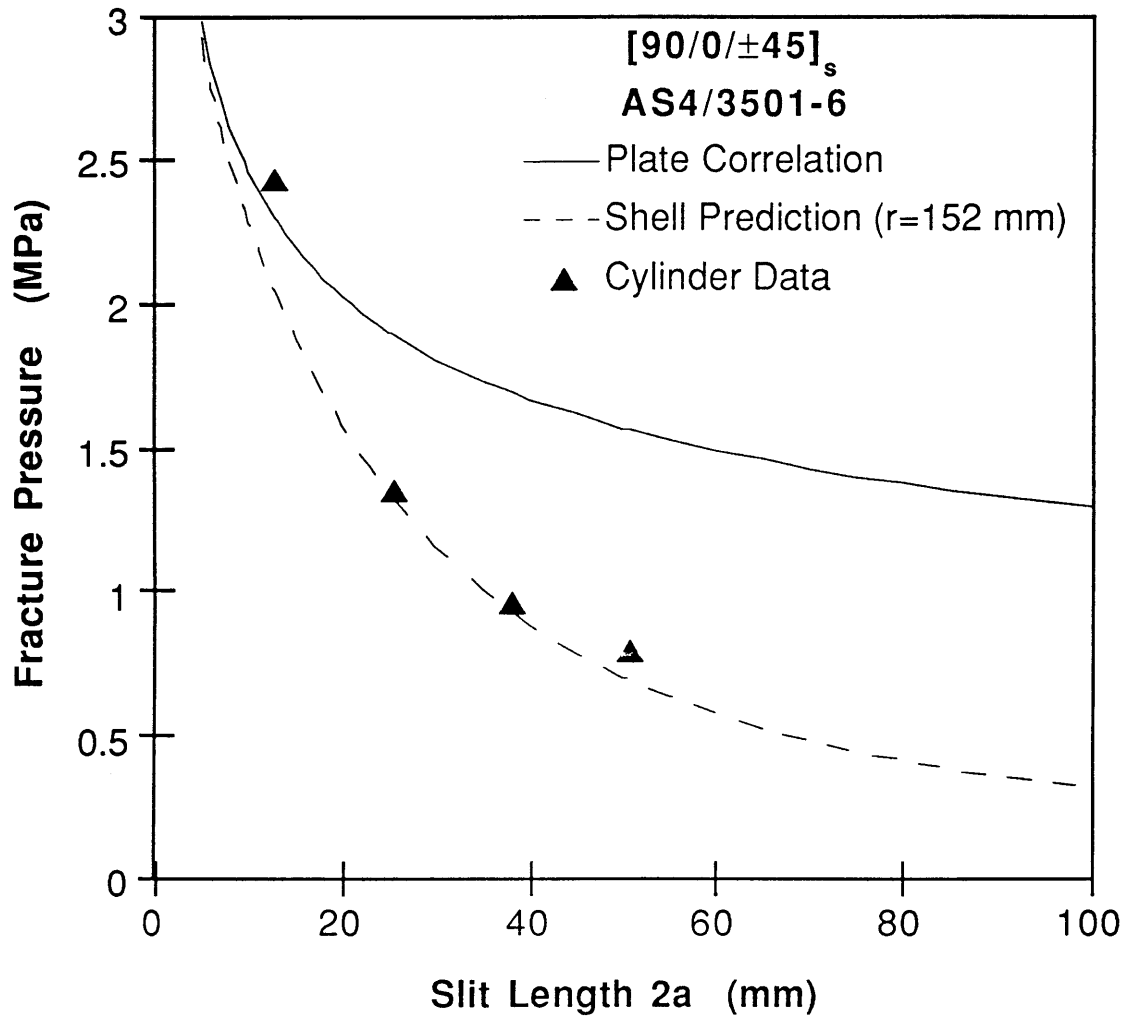
Figure 4.16 [90/0/±45]$_s$ Cylinder Fracture Pressures and Prediction Curve.

Table 4.4 Fracture Data for [90/0/±45]$_s$ Cylinders

Slit Size [mm]	Number of Stiffener Layers	Fracture Pressure [MPa]
12.7	0	2.42
25.4	0	1.34
38.1	0	0.96
50.8	0	0.79
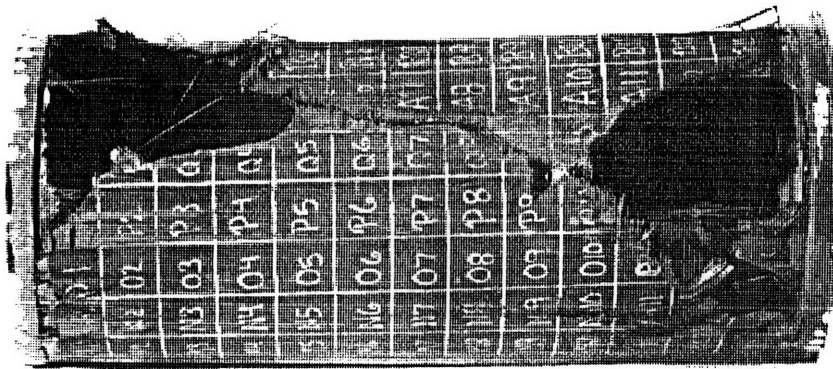
Figure 4.17 Post-Test Photograph of [90/0/±45]$_s$ Cylinder with 50.8 mm Slit and No Stiffeners.
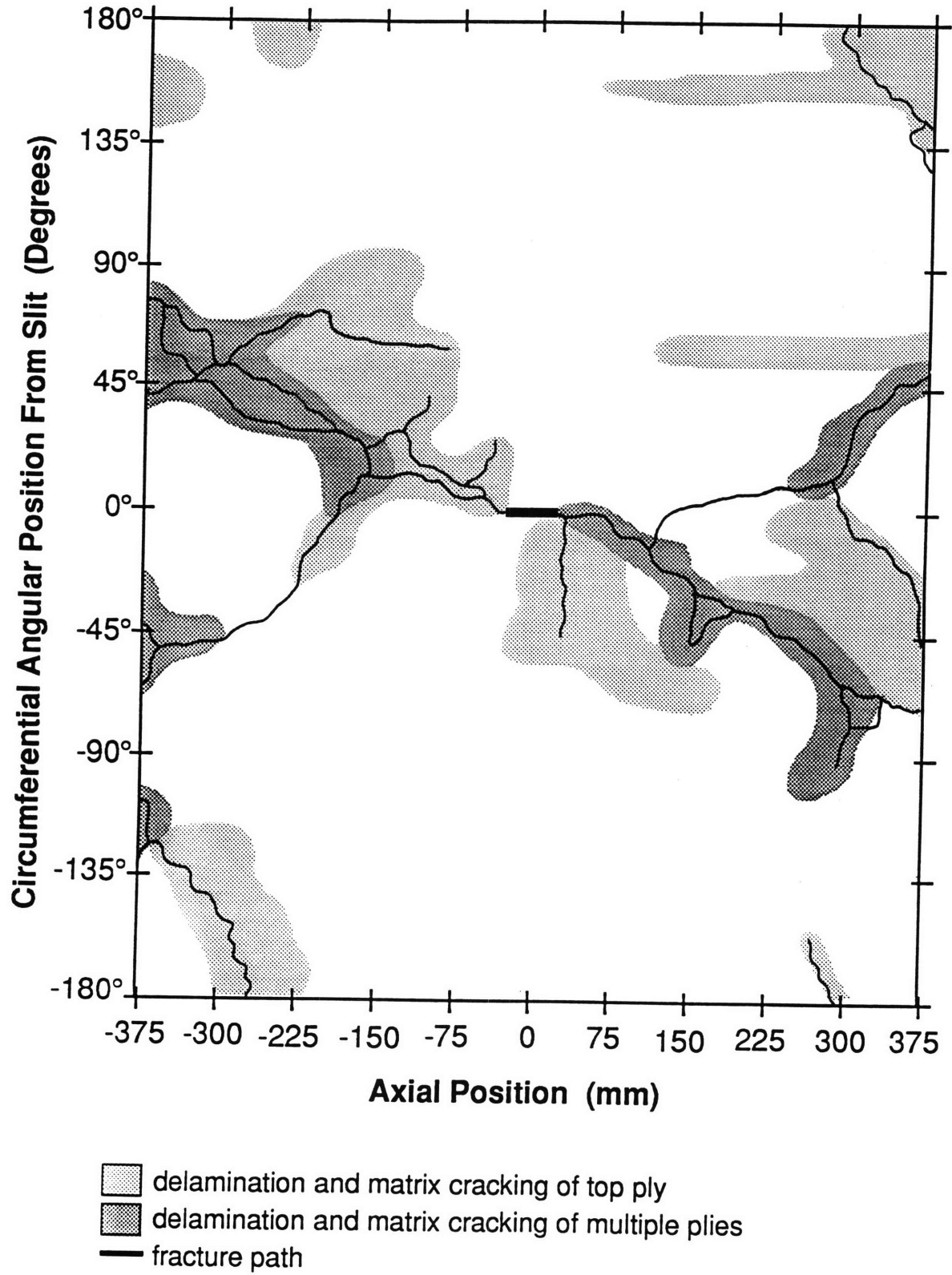
Figure 4.18 Schematic of Fractured [90/0/±45]s Cylinder with 50.8 mm Slit
and No Stiffeners.

path just beyond one slit end and travelling in the circumferential direction for approximately 150 mm before stopping, is visible near the slit as well. Delamination is apparent mainly along the fracture paths.

Fracture of the unstiffened [90/0/±45]$_s$ cylinder with the 38.1 mm slit, occurring at 0.96 MPa, is similar to that of the previous specimen. A post-test photograph and a schematic of the fracture path are shown in Figures 4.19 and 4.20, respectively. The fracture path again originates at the slit ends and extends at -45° towards the endcaps. Bifurcation of the fracture occurs between 100 and 200 mm from the slit ends, resulting in four paths which travel to the endcaps at approximately ±45°. Upon reaching the endcaps, the fracture paths at both ends of the cylinder are abruptly turned and continue around the cylinder to the back. The endcaps are completely separated from the body of the cylinder. Delamination of the external ply, mainly in the 90° direction, is apparent along the primary fracture, in the triangular regions between the bifurcated paths, and along the secondary fracture paths extending from the primary ones. Secondary fracture paths extend back towards the front center of the cylinder from the bifurcated sections. Although the damage is more extensive for this cylinder than for the first, the initial fracture near the slits is similar.

Failure of the [90/0/±45]$_s$ cylinder with the 25.4 mm slit occured at 1.34 MPa. The cylinder fractured into several pieces as seen in the photograph of Figure 4.21 and damage schematic in Figure 4.22. Fracture, originating at the slit ends, travels in the 90° direction for less than 50 mm before abruptly splitting, on one side into two, and on the other into three paths. On both sides, two of the fracture paths extend at ±45° angles. The -45° branches of the fractures continue at this angle for approximately 50 mm before turning back to 90° and progressing directly to the endcaps. The

Figure 4.19 Post-Test Photograph of [90/0/±45]ₛ Cylinder with 38.1 mm Slit
and No Stiffeners.
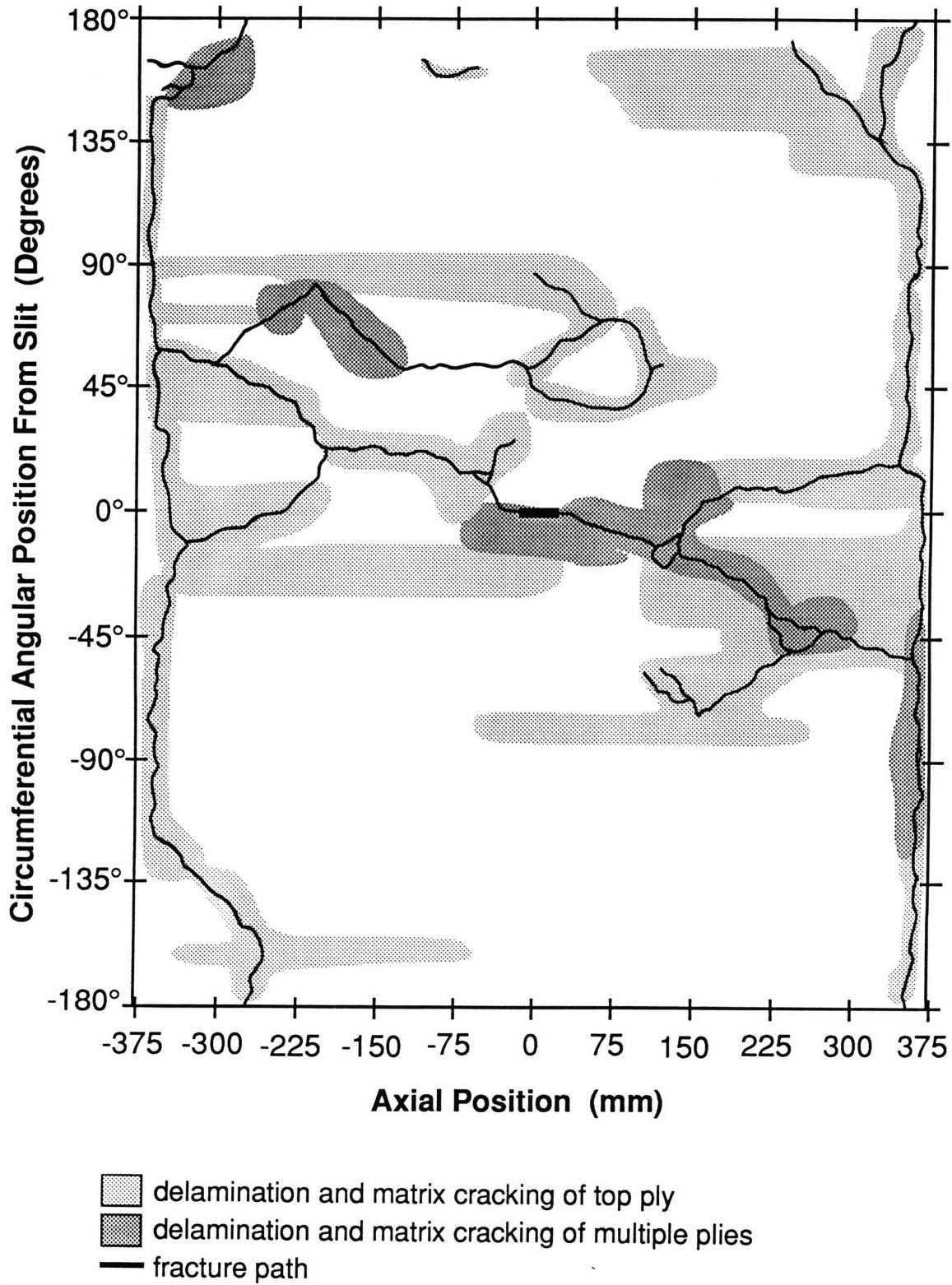
Figure 4.20 Schematic of Fractured [90/0/±45]$_s$ Cylinder with 38.1 mm Slit and No Stiffeners.

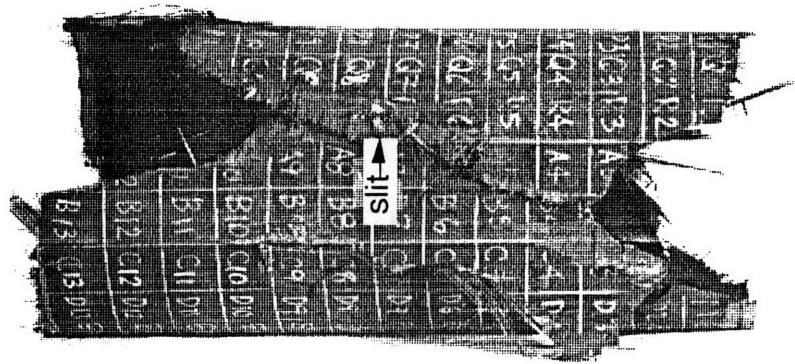Figure 4.21 Post-Test Photograph of [90/0/±45]ₛ Cylinder with 25.4 mm Slit and No Stiffeners.

124
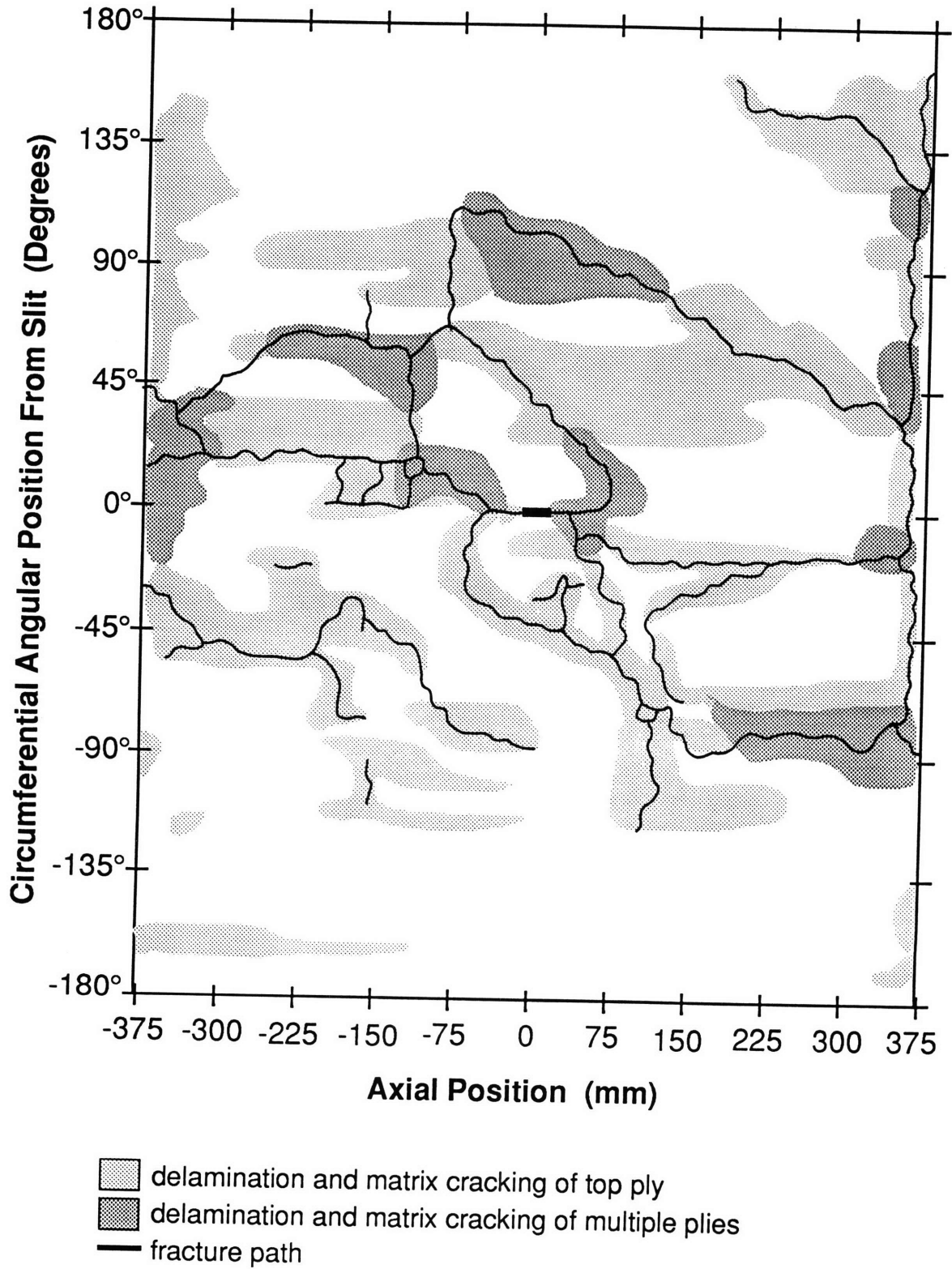
Figure 4.22 Schematic of Fractured [90/0/±45]$_s$ Cylinder with 25.4 mm Slit and No Stiffeners.

45° paths curve first to 0° and then around to -45°, eventually travelling back to the opposite endcaps at this angle. The third path, existing only on one side of the slit, travels around the cylinder for 120 mm at an angle of roughly 15°. Fracture along the endcaps does not extend around the specimen. The region of the cylinder around the slit is permeated with small running cracks which result in many unconnected fragments of graphite/epoxy. Much delamination is apparent in this area as well as along the material near the endcaps.

The fracture of the [90/0/±45]$_s$ cylinder with the 12.7 mm long slit occurred at 2.42 MPa. As shown in Figures 4.23 and 4.24, the cylinder fractured into many fragments. Three fracture paths originate at the slit ends. Two of these paths travel from either end of the slit directly to the endcaps before turning and going entirely around the cylinder. The other path originates at one slit end and extends circumferentially around the cylinder for roughly 70 mm before splitting into two paths. Eventually curving to the axial direction, these paths branch to form many small cylinder fragments. Two clean fractures running axially at the back of the cylinder are visible in Figure 4.24. These occured when the back of the cylinder struck the channel upon which the cylinder was resting, indicating that the sides of the cylinder swung open during the depressurization process. Delamination of the surface 90° fibers, visible over the whole surface of the cylinder, is most apparent in the regions which fractured into small pieces. Most delamination originates at the fracture paths, and little is visible at the back of the cylinder.

A comparison of the post-test [90/0/±45]$_s$ cylinders indicates that fracture modes may depend on slit size. Fracture paths in the regions around the slits are similar in the cylinders with larger slits. In these
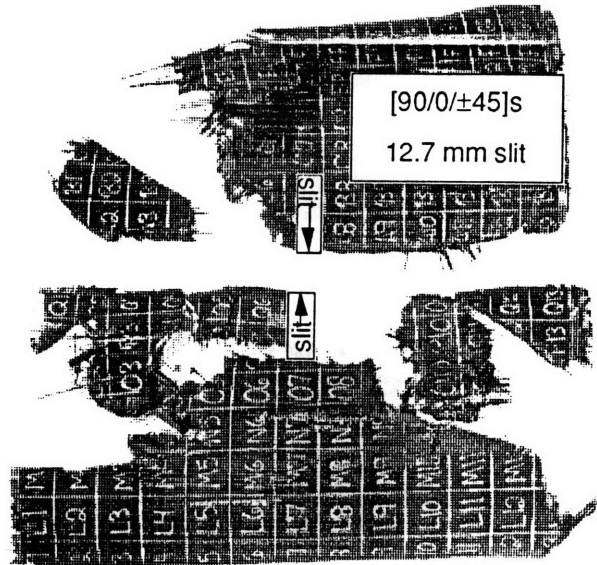
Figure 4.23 Post-Test Photograph of [90/0/±45]$_s$ Cylinder with 12.7 mm Slit and No Stiffeners.

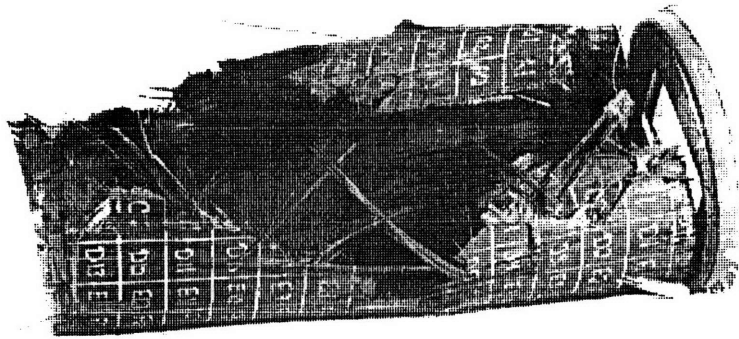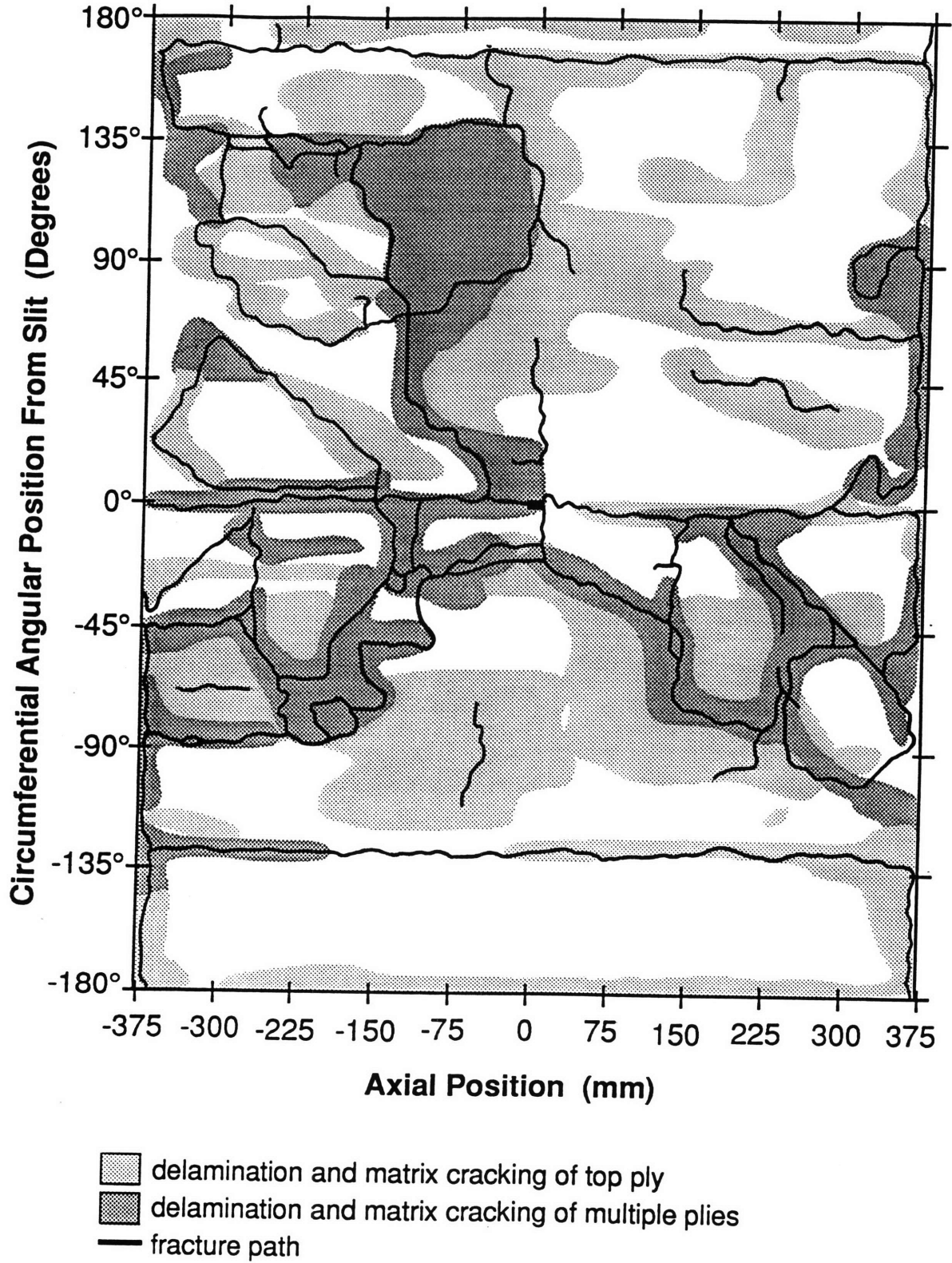Figure 4.24 Schematic of Fractured [90/0/±45]s Cylinder with 12.7 mm Slit and No Stiffeners.

specimens, two primary fracture paths extend outward from the slit ends before bifurcating between 30 and 200 mm from the slit ends to form four lines of fracture. Initial fracture of these cylinders is comparable to that found in the coupons described previously. The cylinder with the 12.7 mm slit, however, has three primary fracture paths originating at the slit ends. In addition to two paths which extend at 90° and proceed directly to the endcaps, another extends in the 0° direction from the slit end. Unlike circumferential fractures in the cylinders with larger slit sizes, the fracture here extends directly from the slit end, and continues for 80 mm before splitting to form two axial fracture paths which contribute greatly to the overall damage in the cylinder.

4.2.2 [±45/0]$_s$ Cylinders

Failure pressures for the structurally anisotropic cylinders were estimated from the coupon data as described previously. The predicted values were used to determine an initial range of slit sizes for which reasonable failure pressures could be expected. In addition to the quasi-isotropic correction factor used to predict failure pressures for the [90/0/±45]$_s$ cylinders, an orthotropic stress correction factor, as previously described, was also applied. Because the properties of the structurally anisotropic cylinders cannot adequately be described in the predictive methods used here, the predicted failure pressures cannot be expected to match the experimental results. The predictive methodology is presented both as an estimate of the range of failure pressures and because the difference between the predicted and experimental results is indicative of the applicability, or lack thereof, of the predictive method.

A graph of the experimental and predicted failure pressures for the [±45/0]$_s$ cylinders is presented in Figure 4.25. The quasi-isotropic and orthotropic corrections fall well below the plate correlation. The experimental data for the cylinders with larger slit sizes falls between the plate and shell prediction curves. For smaller slits, the failure pressures are near the plate values. As the slit size increases, however, the failure pressures are closer to the shell prediction curves. The failure pressure of the specimen with the 12.7 mm slit, however, is not only well above the shell predictions but is higher than the equivalent plate data as well. Data for individual cylinders is presented numerically in Table 4.5.

The fracture of the [±45/0]$_s$ cylinders is quite different from that observed for the [90/0/±45]$_s$ specimens. Discussion of fracture of the individual cylinders is given in order of decreasing slit size. A post-test photograph of the [±45/0]$_s$ cylinder with 63.5 mm slit, which failed at 0.50 MPa, is shown in Figure 4.26. A schematic of the fractured cylinder is shown in Figure 4.27. Note that this cylinder has two layers of stiffening bands on either side of the region with the slit. As with the [90/0/±45]$_s$ specimens, fracture originates at the slit ends. Five initial fracture paths, oriented at angles close to 0°, extend from the slit ends and travel around the cylinder in both directions. Two paths on one side of the slit stop after travelling part of the way around the cylinder. The third path on that side, as well as the paths on the other side of the slit, travel around the cylinder and axially outward at a shallow angle. After reaching the stiffeners, these fracture paths turn back to 0° and continue around the body of the cylinder. The fracture paths extend through the stiffeners on both sides of the slit, but do not reach either endcap. Delamination of the external 45° ply is visible in
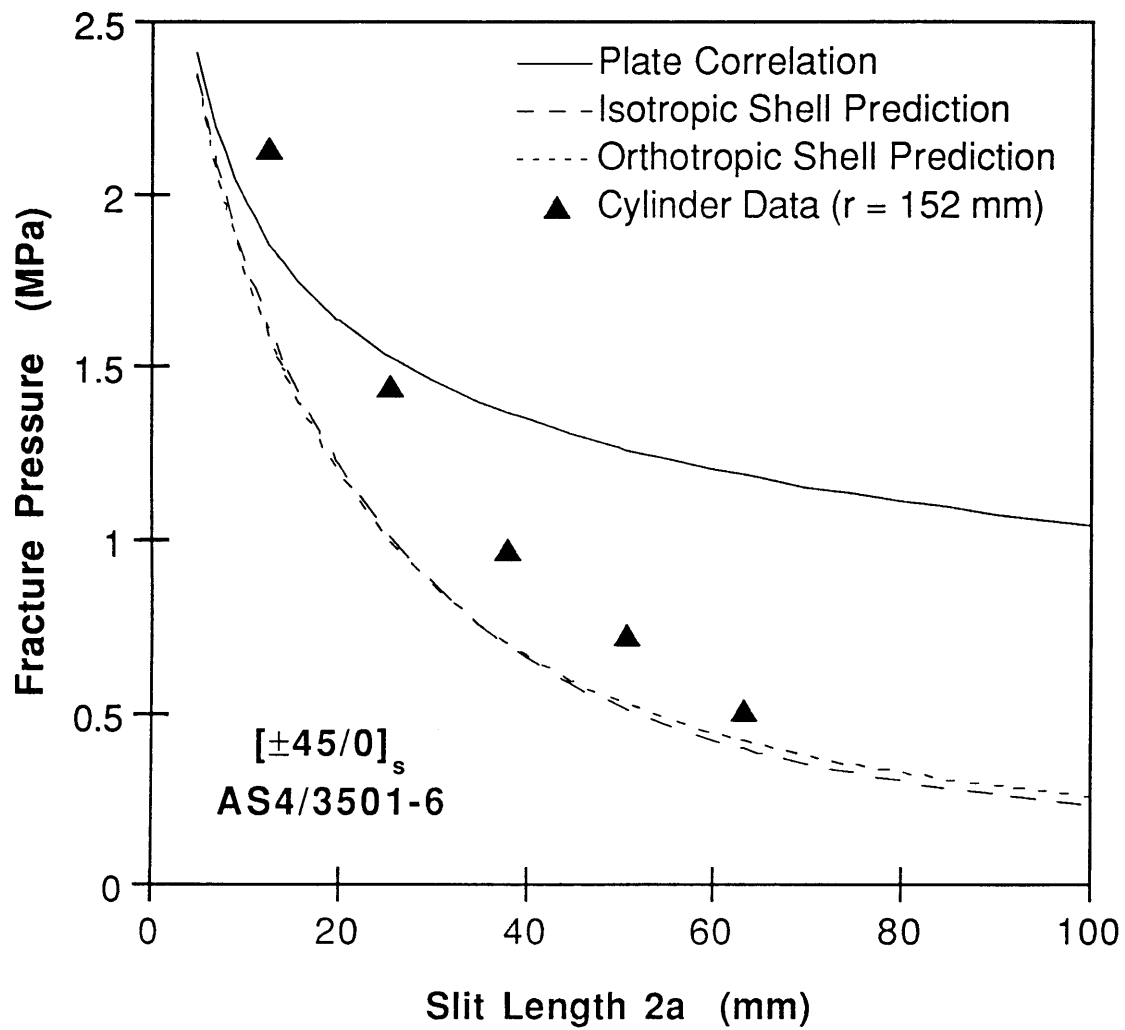
Figure 4.25 [±45/0]$_s$ Cylinder Fracture Pressures and Prediction Curve.

Table 4.5 Fracture Data for [±45/0]$_s$ Cylinders

Slit Size [mm]	Number of Stiffener Layers	Fracture Pressure [MPa]
12.7	4	2.13
25.4	0	1.44
38.1	4	0.97
50.8	2	0.72
63.5	2	0.50

Figure 4.26 Post-Test Photograph of [±45/0]$_s$ Cylinder with 63.5 mm Slit and
2 Layers of Stiffeners.
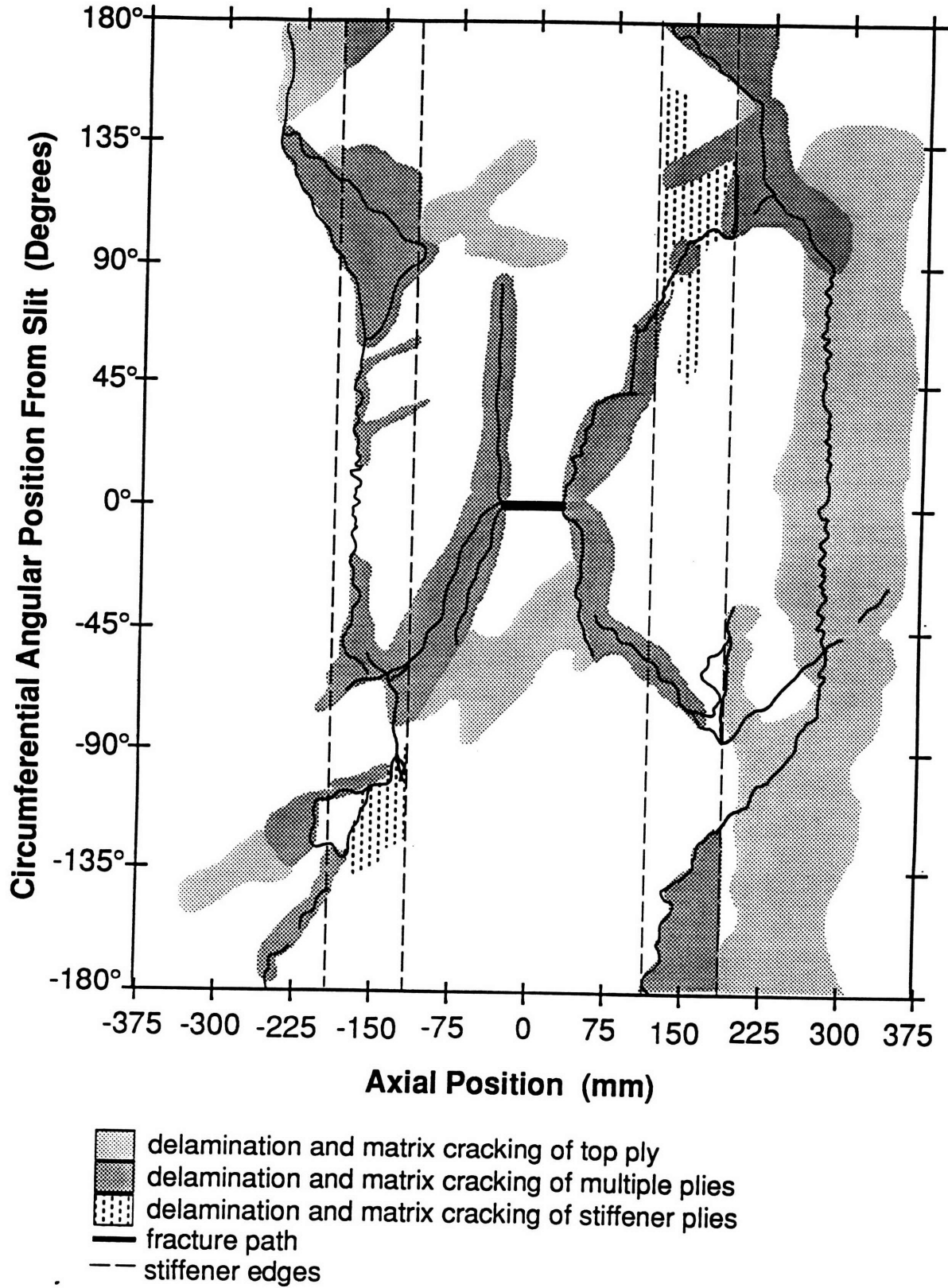
Figure 4.27 Schematic of Fractured [±45/0]s Cylinder with 63.5 mm Slit and 2 Layers of Stiffeners.

the region just outside the stiffeners, along the fracture paths, and in the region surrounding the slit.

The [±45/0]$_s$ cylinder with a 50.8 mm slit failed at 0.72 MPa. A photograph of the post-test specimen is shown in Figure 4.28. The cylinder is divided into three sections by the fracture paths as shown in the schematic in Figure 4.29. The area of damage to the cylinder is contained almost entirely by the two layers of external stiffeners located 90 mm to either side of the slit ends. Four major paths of damage originate at the slit ends. Three of these paths extend at ±45° from the slit end and turn to 0° near the edge of the stiffeners. Of these, one path extends into the stiffener about 25 mm before changing angle and continuing around the cylinder. The fourth fracture path extends at 0° from the slit end and continues halfway around the cylinder before angling out to meet its partner travelling around the cylinder from the other direction. Delamination of the surface 45° fibers is visible mainly in the center section near the slit.

Fracture of the [±45/0]$_s$ cylinder with the 38.1 mm slit occured at 0.97 MPa. The damage is entirely contained in the region between the pair of stiffeners, each four layers thick, as shown in the photograph in Figure 4.30. A schematic of the fracture paths is shown in Figure 4.31. Four fracture paths originate at the slit ends at ±45° angles. Roughly 50 mm from the stiffeners, the fracture paths on one side of the slit turn towards 0°, travelling to the stiffeners at a shallow angle. Upon reaching the stiffeners, the paths turn to 0° and continue around the cylinder where they meet in the back. The -45° fracture path on the opposite side of the slit behaves in a similar fashion, while the other curves from +45° to -45°, traversing the center region of the cylinder 100 mm from the slit. Local damage around the slit is severe; portions of the cylinder from this area

Figure 4.28 Post-Test Photograph of $[\pm 45/0]_s$ Cylinder with 50.8 mm Slit and 2 Layers of Stiffeners.

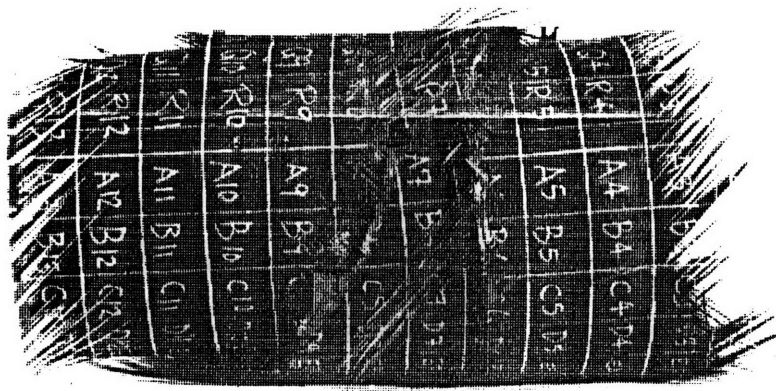Figure 4.29 Schematic of Fractured [±45/0]ₛ Cylinder with 50.8 mm Slit and 2 Layers of Stiffeners.

Figure 4.30 Post-Test Photograph of [±45/0]$_s$ Cylinder with 38.1 mm Slit and
4 Layers of Stiffeners.

Figure 4.31 Schematic of Fractured [±45/0]$_s$ Cylinder with 38.1 mm Slit and 4 Layers of Stiffeners.

were not recovered from the fragments in the blast chamber. Delamination of fibers in the surface 45° ply is limited to the center section bounded by the stiffeners.

The [±45/0]$_s$ cylinder with a 25.4 mm slit failed at 1.44 MPa. The cylinder, which had no stiffeners, fractured into numerous pieces as seen in the photograph in Figure 4.32. A schematic of the recovered cylinder fragments is shown in Figure 4.33. Some of the material in the region around the slit was not identifiable after the test. Portions of the cylinder surrounding the slit indicate that four fracture paths extend from the slit ends at angles between 0° and ±45°. Branching of the fracture paths occurs above and below the slit, and results in numerous small cylinder fragments, especially in the region immediately surrounding the slit. Fractures terminating at the endcaps are rough and uneven, and do not follow any one angle as they progress outward. The fracture paths do not travel around the entire circumference of the cylinder.

The failure pressure for the [±45/0]s cylinder with the 12.7 mm slit is 2.13 MPa. It is difficult to determine the fracture paths for this cylinder because the damage to the cylinder is so severe. A post-test photograph of this cylinder, which has four layers of stiffeners, is shown in Figure 4.34. A schematic of the damage is shown in Figure 4.35. Fracture paths originating at the slit are seen both along 0° and 90° directions. The main fracture extends to the stiffeners at 90°. At the stiffeners, the paths are turned to shallow angles, and travel almost all the way around the tube before going all the way through the stiffeners. At this point, the fractures turn outward to the endcaps. The fracture paths then continue around the cylinder at the endcaps. Considerable damage is also visible in the region directly around the slit. A fracture path propagates halfway around the

Figure 4.32 Post-Test Photograph of [±45/0]$_s$ Cylinder with 25.4 mm Slit and No Stiffeners.

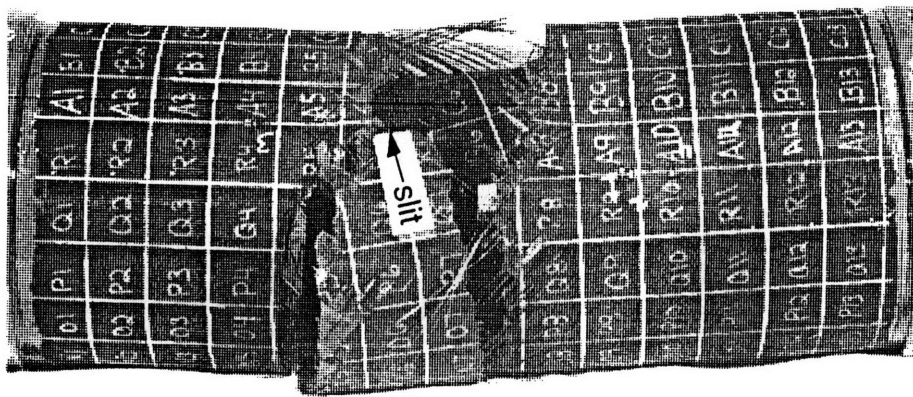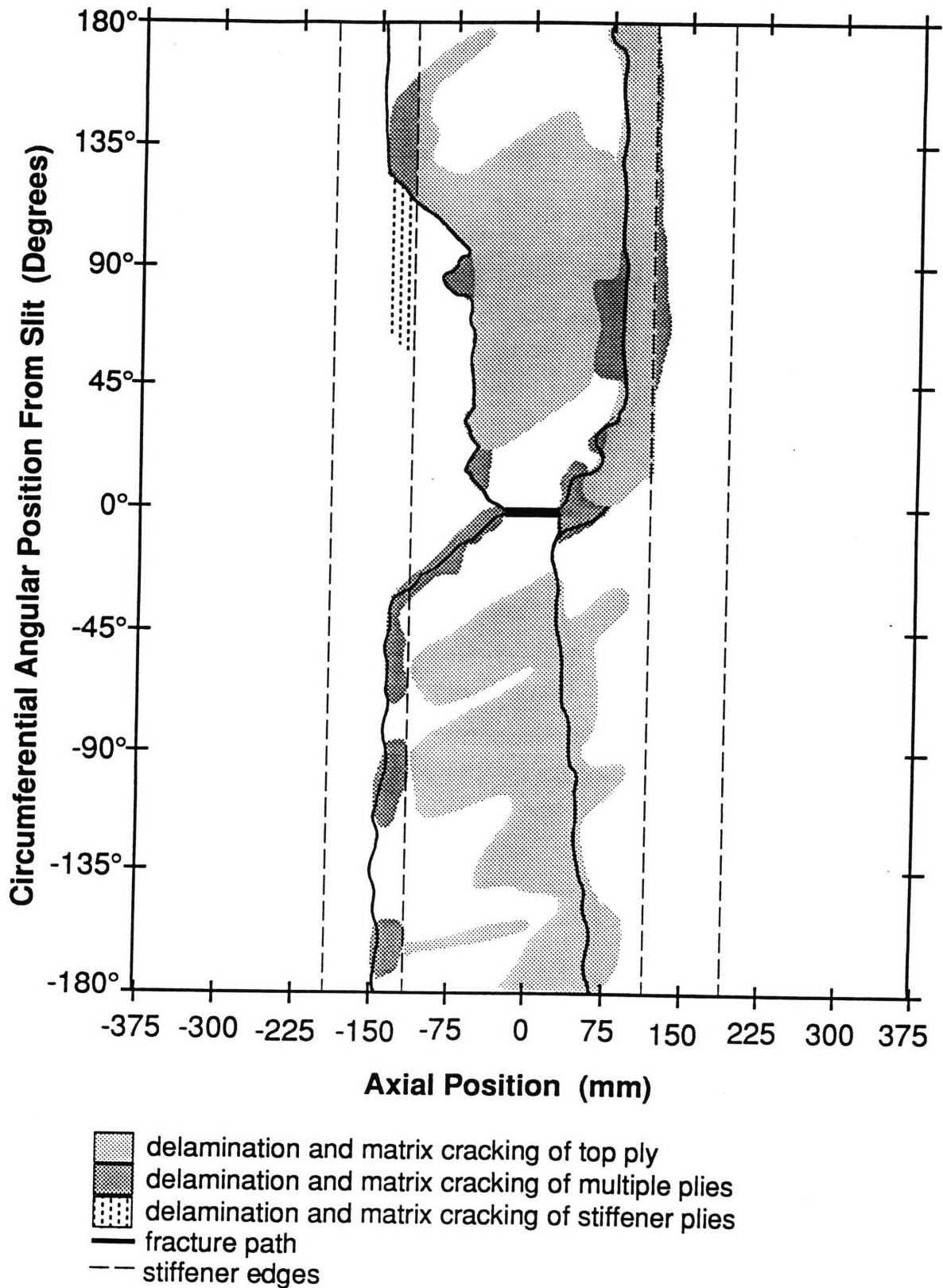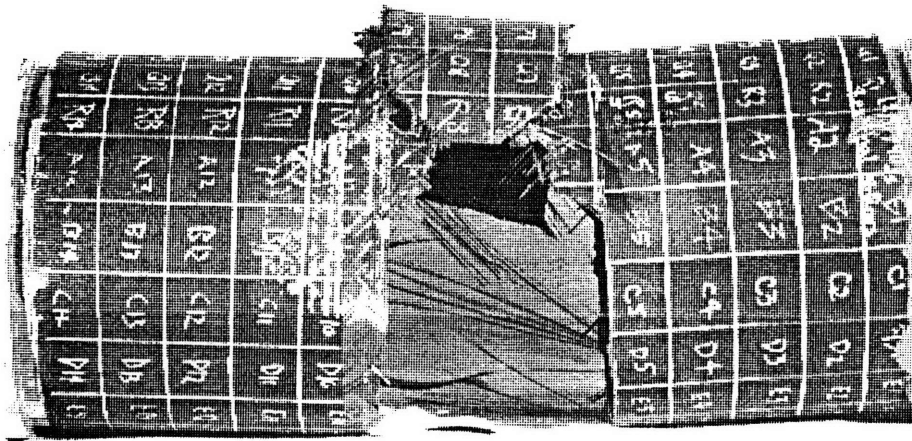Figure 4.33 Schematic of Fractured [±45/0]$_s$ Cylinder with 25.4 mm Slit and No Stiffeners.

Figure 4.34 Post-Test Photograph of [±45/0]$_s$ Cylinder with 12.7 mm Slit and 4 Layers of Stiffeners.

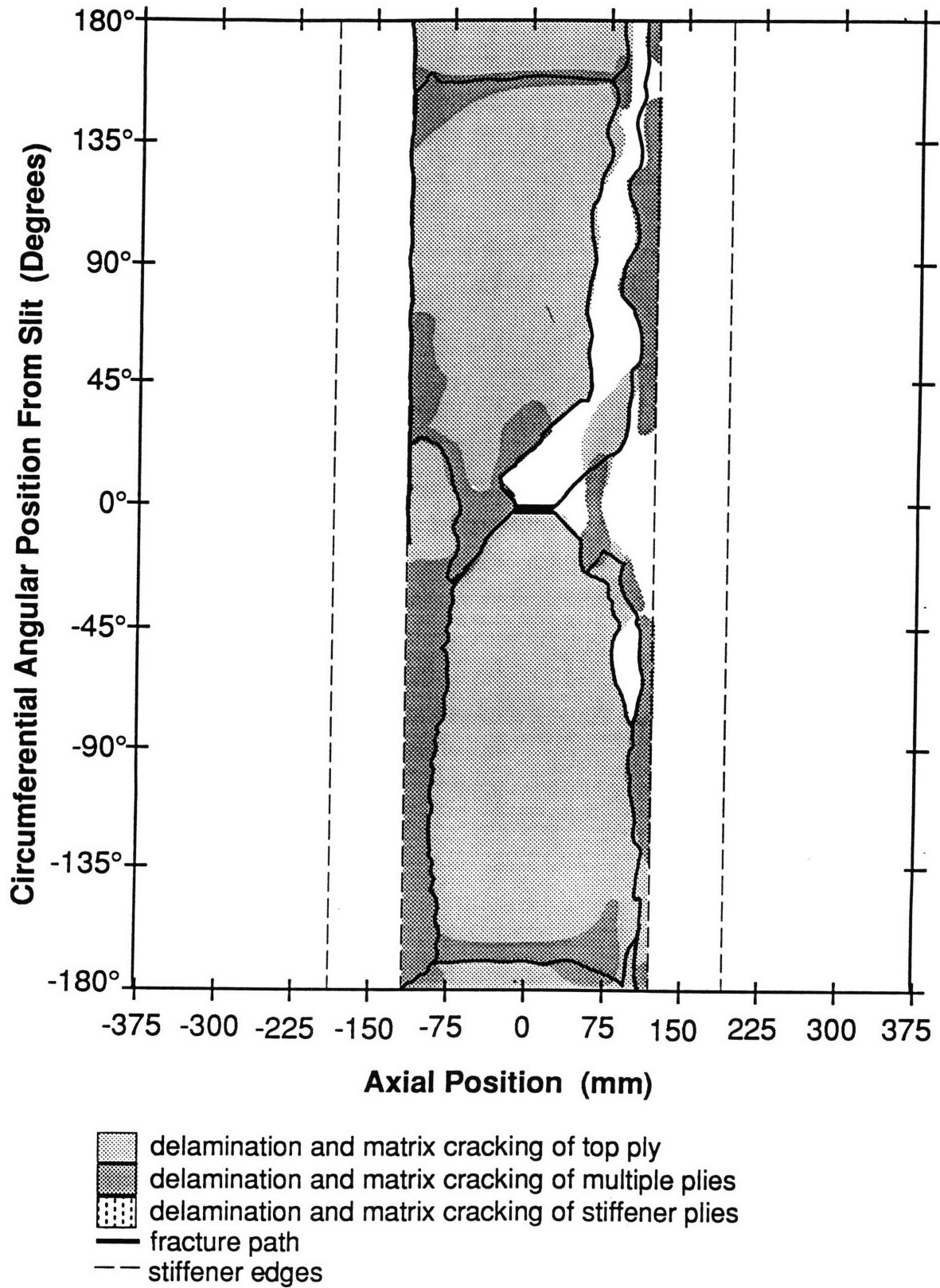Figure 4.35 Schematic of Fractured [±45/0]$_s$ Cylinder with 12.7 mm Slit and 4 Layers of Stiffeners.

cylinder from the slit, and then turns abruptly outward to the stiffeners. As seen in Figure 4.35, a portion of the cylinder adjacent to the slit is missing, and so local fracture is hard to describe. Delamination of the four-ply external stiffening bands from the base laminate is apparent around the entire specimen. Some delamination of the surface ply, extending from the fracture paths, is visible as well.

In general, four fracture paths originate at the slit ends in the [±45/0]$_s$ cylinders. Initial fracture paths of the cylinders with larger slits extend primarily in the 0° and ±45° directions. As slit size decreases, the angles of some of the fracture paths increases. Fracture paths extending from the slit at 90° are visible primarily in the cylinder with the 12.7 mm slit. Initial fracture in the cylinder with no stiffeners and a 25.4 mm slit is similar to that found in cylinders with other slit sizes and stiffener configurations. This indicates that the presence of stiffeners does not change the initial fracture in a region extending at least 30 mm around all sides of the slit.

4.2.3 [±45/90]$_S$ Cylinders

Failure of the [±45/90]$_s$ cylinders occurred at much lower pressures than did failure of the [±45/0]$_s$ specimens with corresponding slit sizes. This is due to the lack of fibers running in the major load-carrying 0° direction. Failure pressures of the cylinders are graphed with the plate correlation and both the quasi-isotropic and orthotropic curvature corrections in Figure 4.36. Individual cylinder data is presented numerically in Table 4.6. As with the [±45/0]$_s$ cylinders, most of the [±45/90]$_s$ data falls between the plate and shell curves. As slit sizes increase, the cylinder data gets closer to the shell predictions. It should be
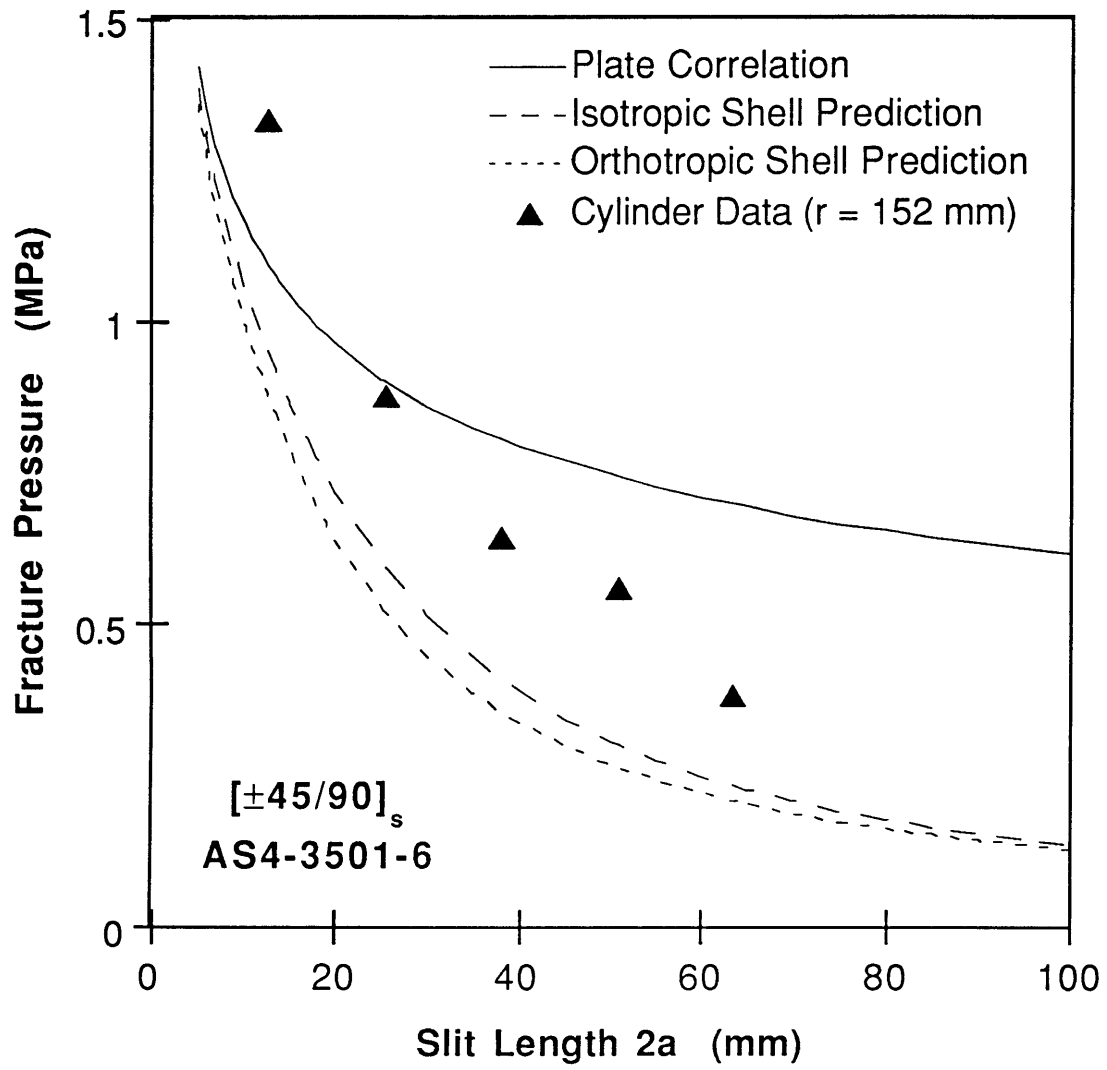
Figure 4.36 [±45/90]ₛ Cylinder Fracture Pressures and Prediction Curve.

Table 4.6 Fracture Data for [±45/90]ₛ Cylinders

Slit Size [mm]	Number of Stiffener Layers	Fracture Pressure [MPa]
12.7	4	1.33
25.4	0	0.88
38.1	0	0.64
50.8	4	0.56
63.5	2	0.38

noted again, however, that agreement of the experimental data and the shell predictions is not expected. As with the other tape cylinders tested, the cylinder with the 12.7 mm slit size failed at a pressure higher than both the shell prediction and the plate correlation and data.

Fracture is described individually for each specimen. The $[\pm45/90]_s$ cylinder with the 63.5 mm slit failed at 0.38 MPa. This cylinder has two layers of external stiffeners as shown in Figure 4.37. A schematic of the fractured cylinder is shown in Figure 4.38. Fracture originates at the slit ends and bifurcates almost immediately to form four $\pm45°$ paths. These paths extend to the stiffeners, where they turn sharply towards the $0°$ direction. Two of the paths continue entirely through the stiffeners and continue to the endcaps. The other two paths turn completely to $0°$ just inside the stiffener. One of these stops at this point while the other then turns abruptly to $90°$ through the stiffener before continuing at $45°$ towards the endcap. Damage extends almost all the way around the cylinder. Delamination of the stiffeners is seen in the regions which the fracture paths traverse.

The failure pressure of the $[\pm45/90]_s$ cylinder with a 50.8 mm slit is 0.56 MPa. As seen in the phototgraph of Figure 4.39 and schematic of Figure 4.40, the fracture path of this cylinder is contained almost entirely by the four layers of external stiffeners. Fracture originates at the slit ends, and as with the previous $[\pm45/90]_s$ cylinder, continues at $90°$ for only a short distance before bifurcating to $\pm45°$. Upon reaching the stiffening bands, the fractures turn abruptly to $0°$ and travel circumferentially along the edges of the stiffeners. One of the four fracture paths extends into the stiffener at a shallow angle before turning inward towards the center of the cylinder. The fracture essentially split the cylinder into three sections. Delamination
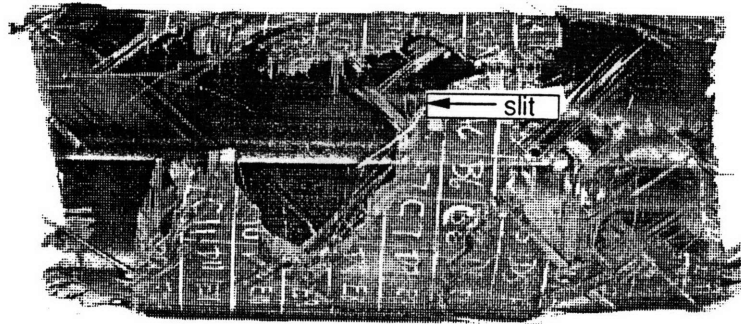
Figure 4.37 Post-Test Photograph of [±45/90]s Cylinder with 63.5 mm Slit
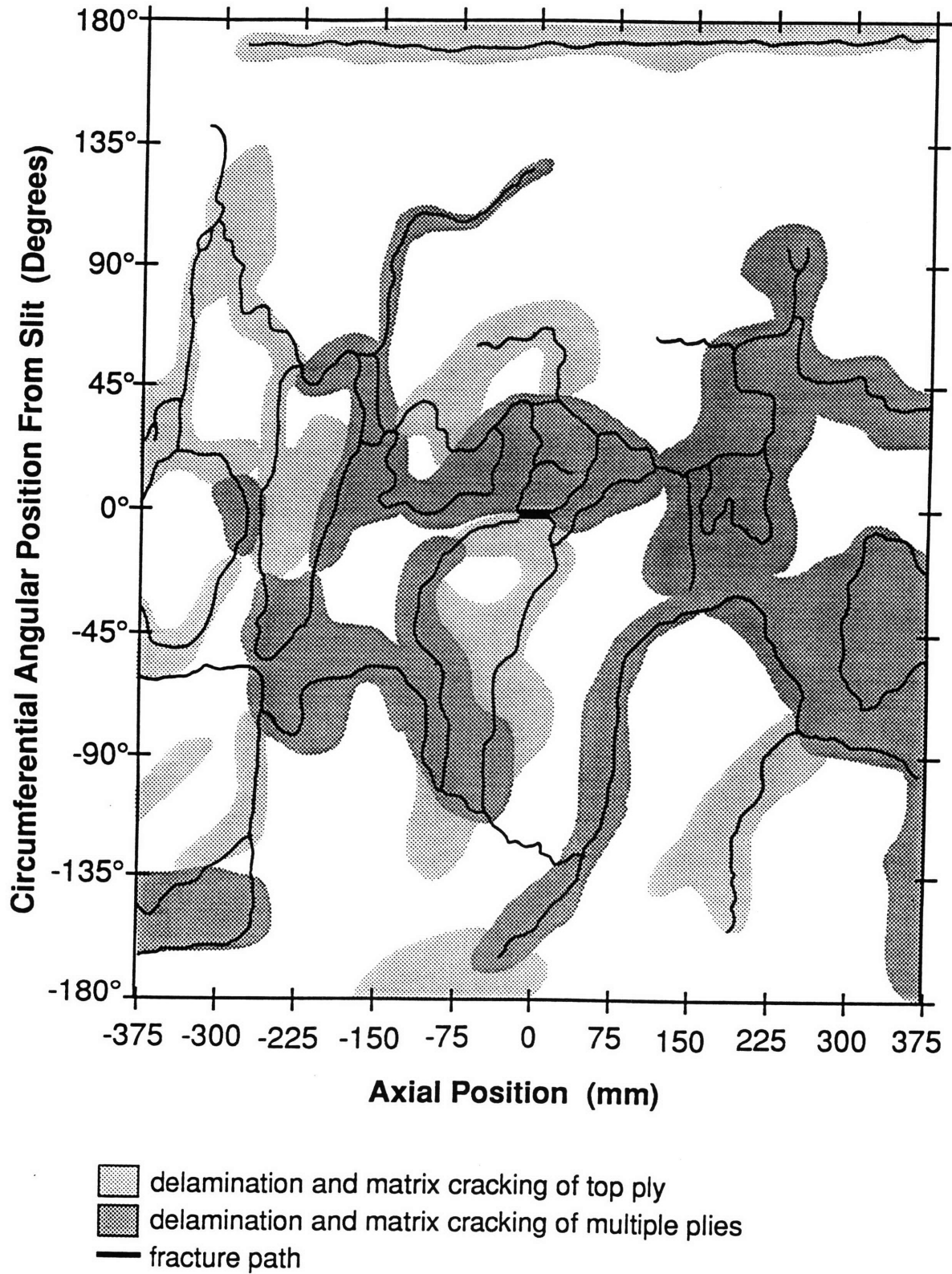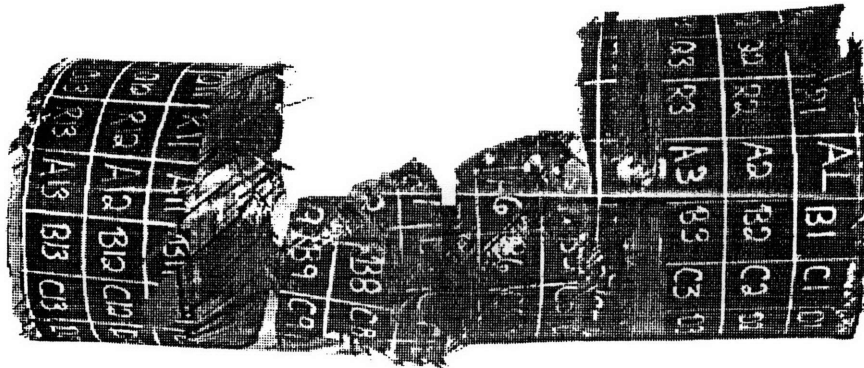and 2 Layers of Stiffeners.

Figure 4.38 Schematic of Fractured [±45/90]ₛ Cylinder with 63.5 mm Slit
and 2 Layers of Stiffeners.

Figure 4.39 Post-Test Photograph of [±45/90]ₛ Cylinder with 50.8 mm Slit
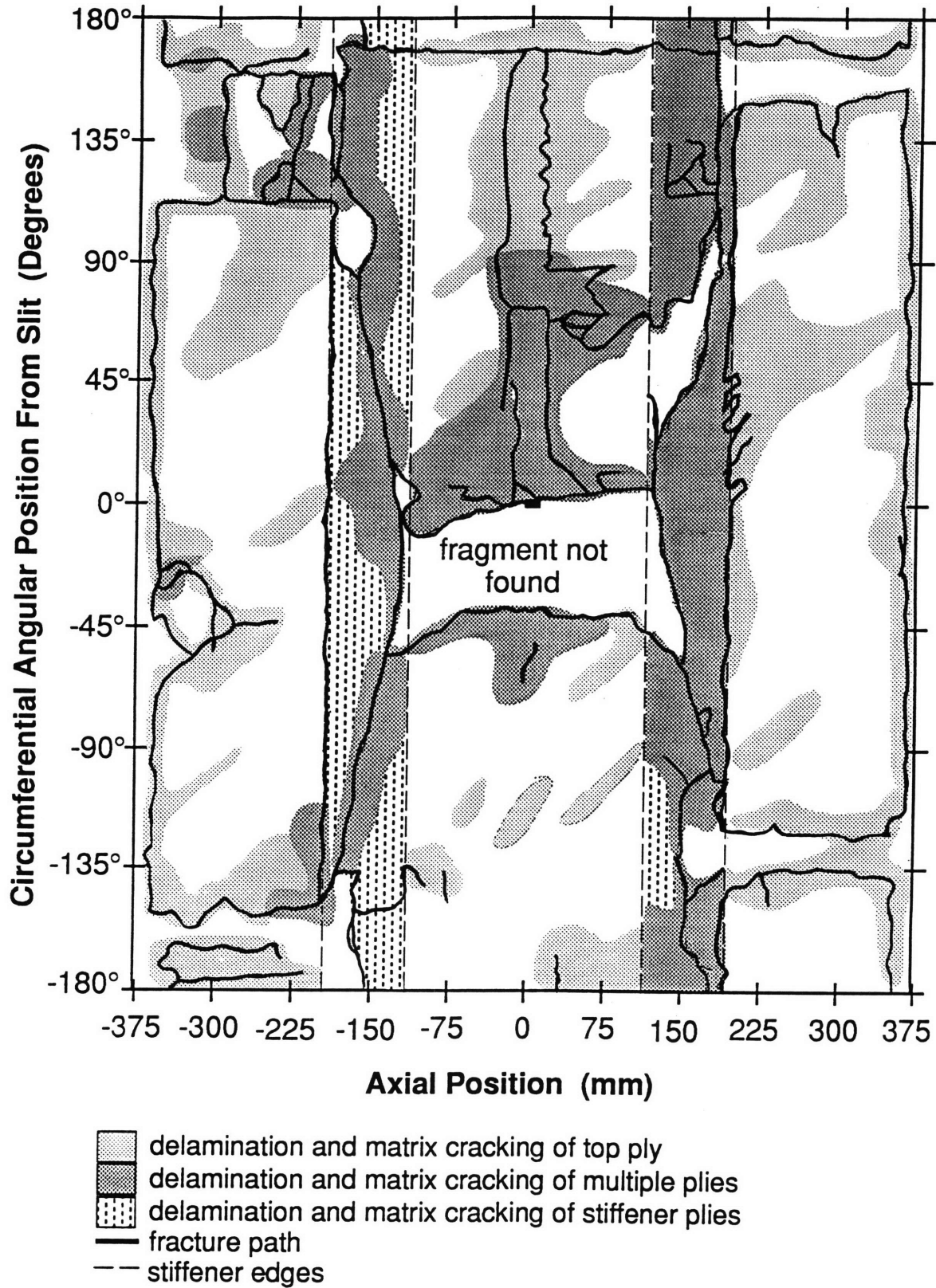and 4 Layers of Stiffeners.
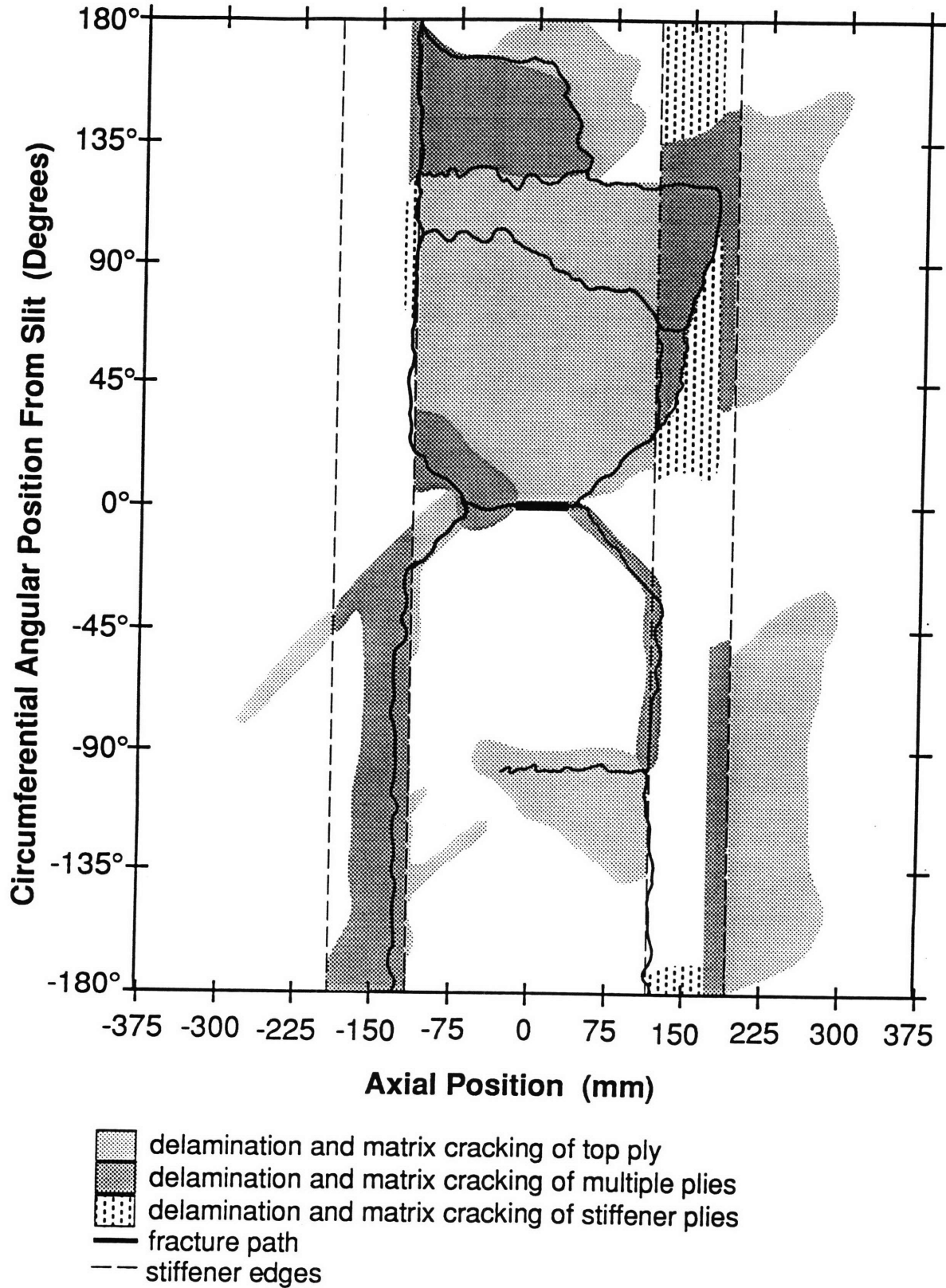
Figure 4.40 Schematic of Fractured [±45/90]s Cylinder with 50.8 mm Slit and 4 Layers of Stiffeners.

of the stiffeners is seen in the region through which the fracture extended. Delamination of the outer +45° ply is apparent in the region near the slit as well as along the outer edge of the stiffeners.

The failure pressure of the cylinder with the 38.1 mm slit is 0.64 MPa. Fracture in this unstiffened cylinder originates at the slit ends, as shown in the photograph in Figure 4.41. A schematic of the damage to the cylinder is shown in Figure 4.42. On one side of the slit, the fracture bifurcates almost immediately, and the arms of the fracture path extend to the endcap at ±45°. The fracture path originating at the other slit end continues towards the endcap for roughly 200 mm before bifurcating. Again, the arms of the fracture extend to the endcap at ±45°. Upon reaching the endcaps, the four fracture paths travel almost entirely around the cylinder, effectively separating the body of the specimen from the endcaps.

Fracture of the [±45/90]$_s$ cylinder with the 25.4 mm slit occurred at 0.88 MPa. Fragments of the post-test cylinder, which has no stiffening bands, are shown in Figure 4.43, and a schematic of the damage follows in Figure 4.44. Reconstruction of the cylinder was difficult because no reference marks had been drawn on the external surface. It can be determined from the identified pieces that fracture originated at the slit ends and propagated outward towards the endcaps at 90°. These fracture paths branched into two or more paths at 75 and 150 mm from the slit ends. The branched paths travelled to the endcaps at angles between ±45° and 90°. The region of the cylinder containing the slit is broken into small pieces by small, ragged fracture paths. An additional fracture path, which does not intersect with the slit, extends from one endcap to the other exactly at a -45° angle.
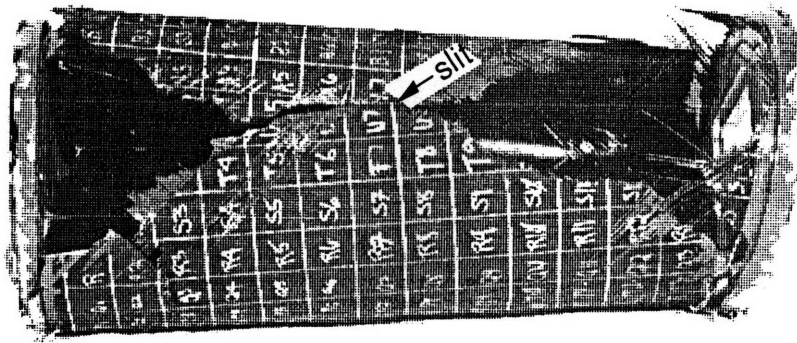
Figure 4.41 Post-Test Photograph of [±45/90]ₛ Cylinder with 38.1 mm Slit
and No Stiffeners.
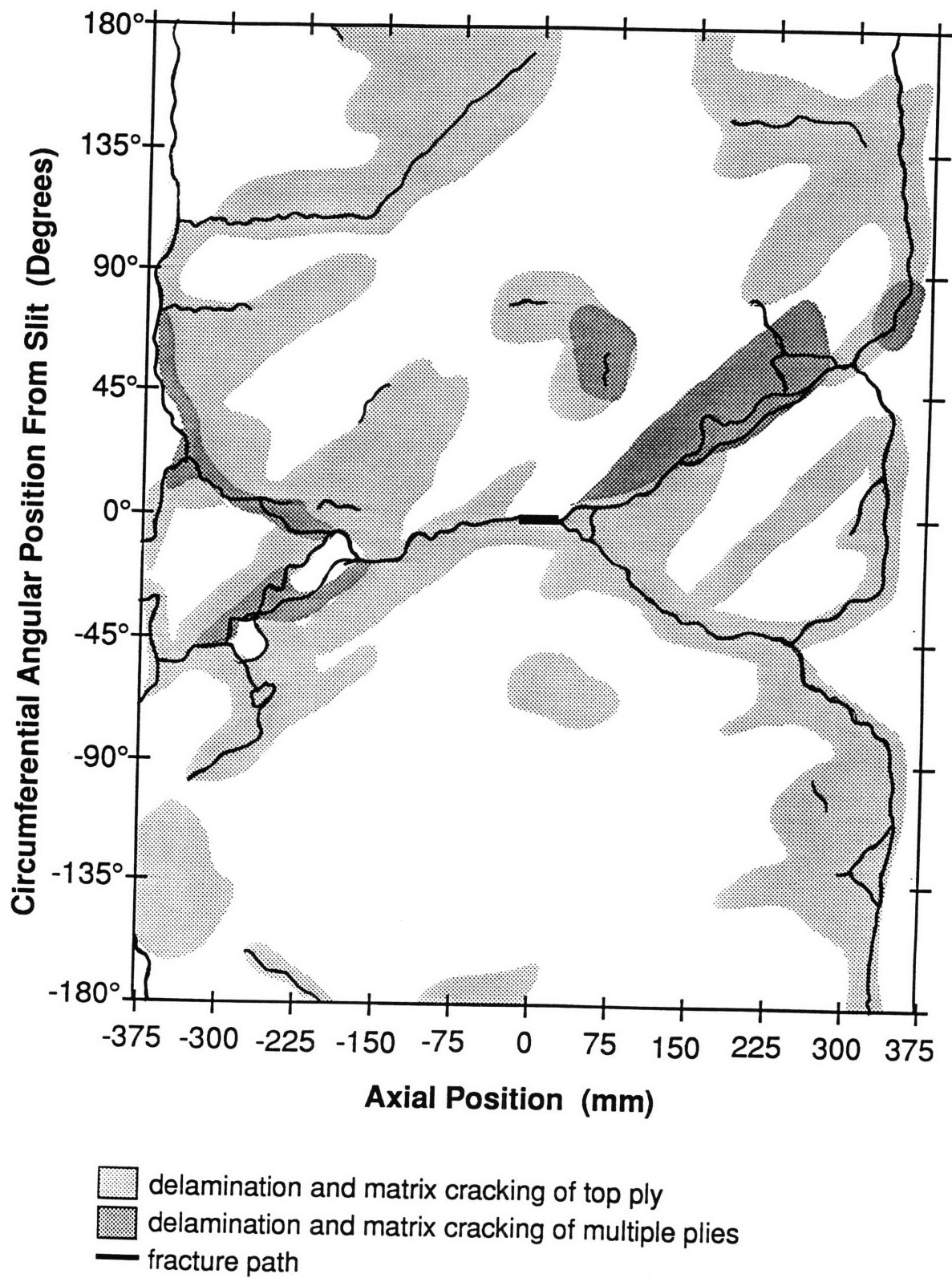
Figure 4.42 Schematic of Fractured [±45/90]s Cylinder with 38.1 mm Slit
and No Stiffeners.

Figure 4.43 Post-Test Photograph of [±45/90]ₛ Cylinder with 25.4 mm Slit and No Stiffeners.
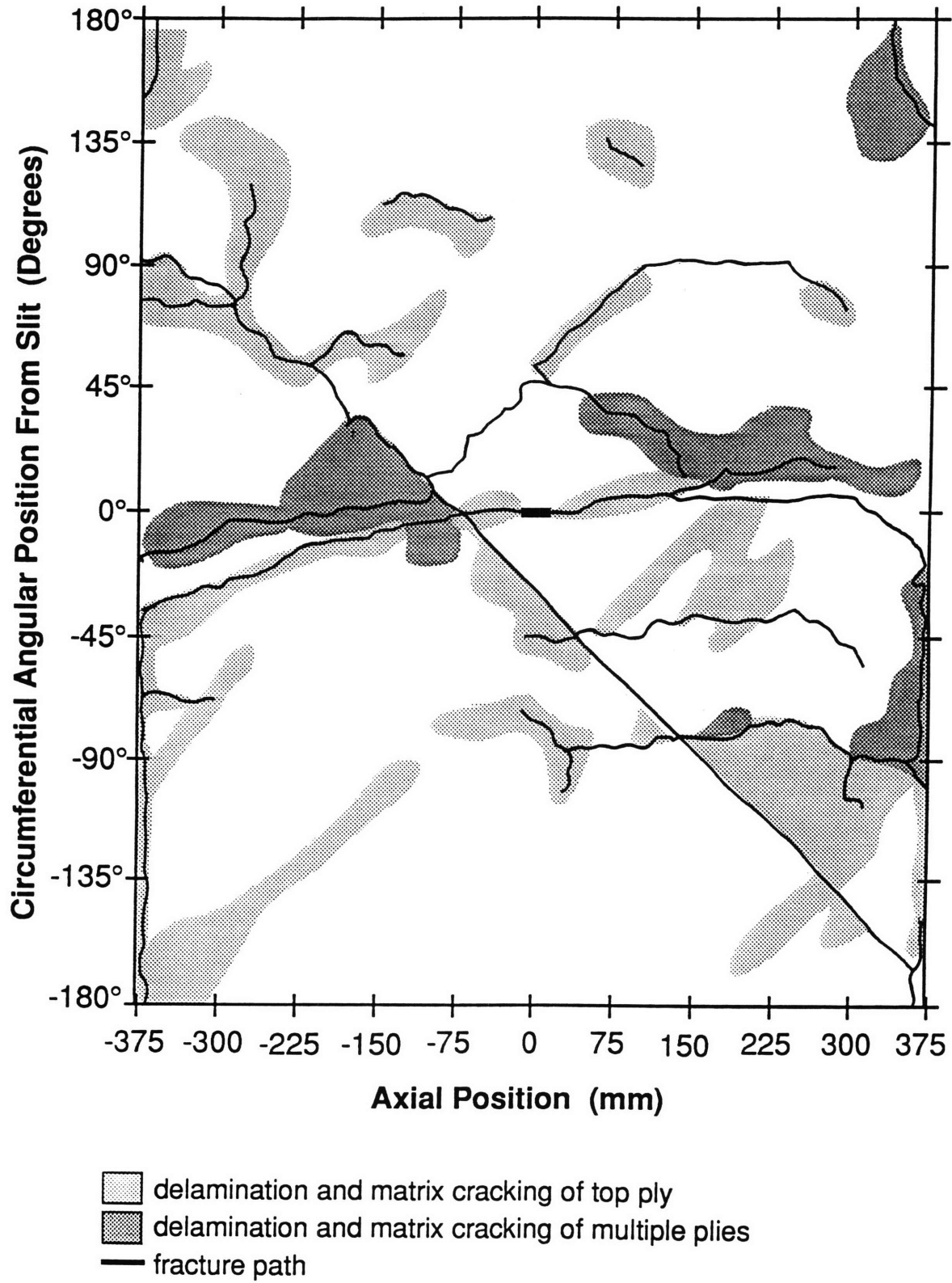
Figure 4.44 Schematic of Fractured [±45/90]ₛ Cylinder with 25.4 mm Slit and No Stiffeners.

The [±45/90]$_s$ cylinder with the 12.7 mm slit fractured at an internal pressure of 1.33 MPa. A photograph of the cylinder, which has four layers of stiffening bands, is shown in Figure 4.45. The damage to this cylinder is catastrophic as seen in the schematic shown in Figure 4.46. The region around the slit was fractured into many small fragments, some of which have not been identified. It is possible, however, to describe much of the fracture from the remaining pieces. The fracture paths originating at the slit ends travel outward at 90° to the center of the stiffeners. The damage paths then bifurcate and turn abruptly to follow the stiffeners around the circumference of the cylinder. At one end of the cylinder, the fracture only goes halfway through the stiffener, and damage outside the stiffener is limited to delamination of the external +45° ply. At the other, fracture extends completely through the stiffener at several points. The paths extend directly to the endcap and turn to go around the entire circumference of the cylinder. Fracture paths emanating from the damage at the stiffeners traverse the region between the stiffeners as well. The region of the cylinder containing the slit is damaged most severely.

Two initial fracture paths originating at the slit ends and propagating in the 90° direction are found in all [±45/90]s cylinders. Bifurcation of the fracture paths is seen in all cylinders, and occurs between 20 and 50 mm from the slit ends in the cylinders with stiffening bands, and between 20 and 200 mm from the slit ends in the unstiffened cylinders. The cylinder with the 12.7 mm slit exhibits much more damage in the region around the slit than do the cylinders with larger slit sizes.
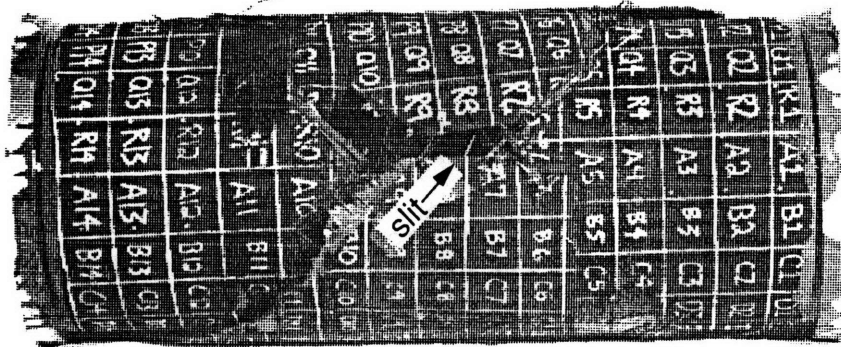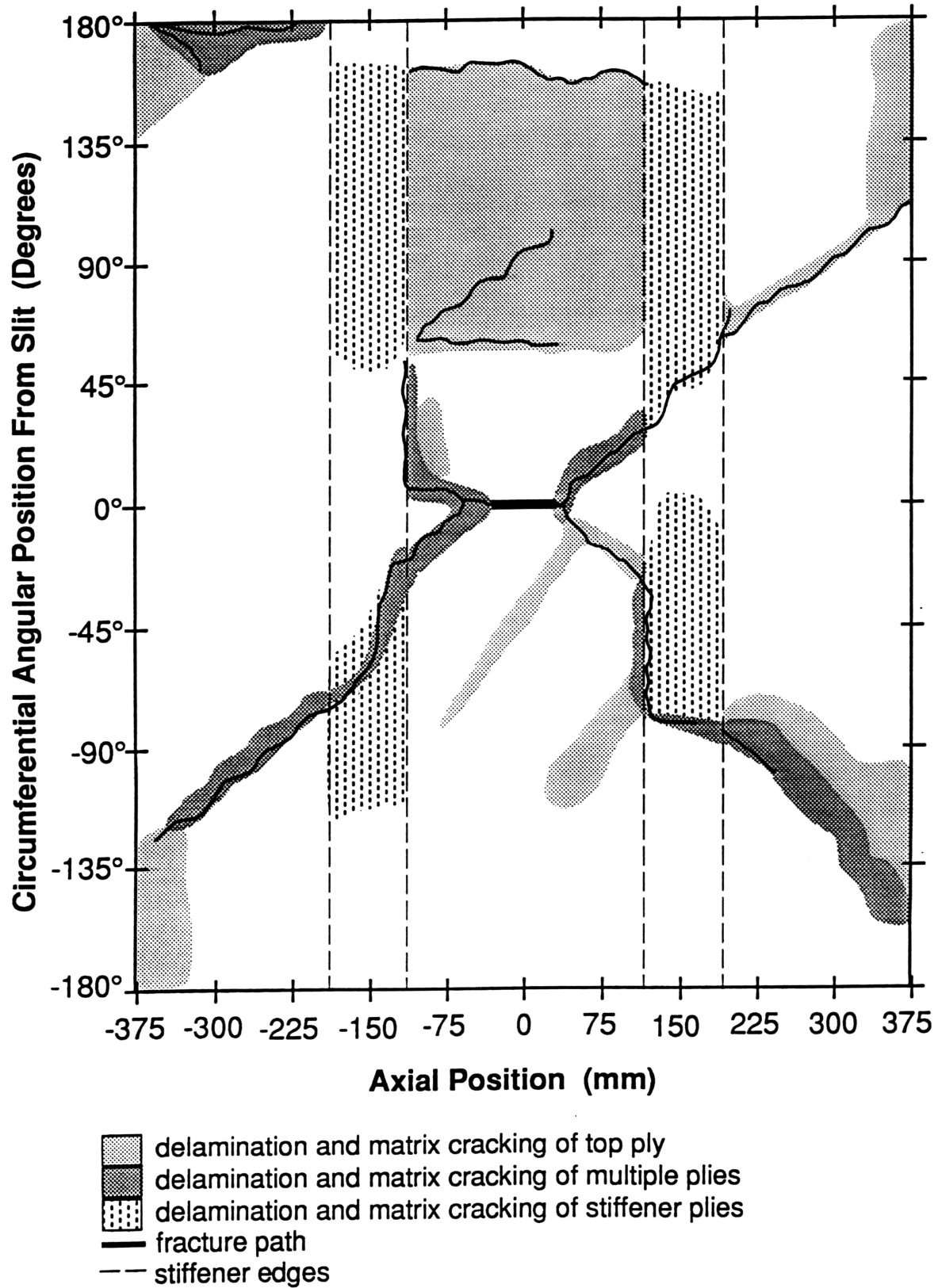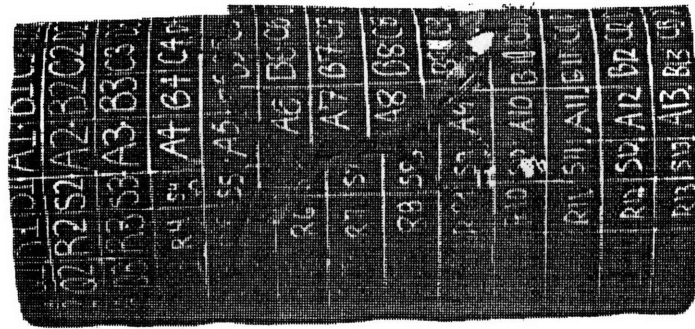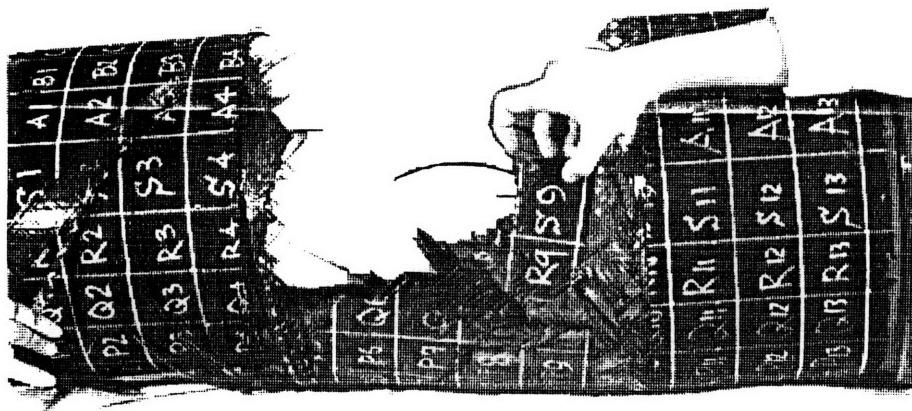
Figure 4.45 Post-Test Photograph of [±45/90]$_s$ Cylinder with 12.7 mm Slit
and 4 Layers of Stiffeners.
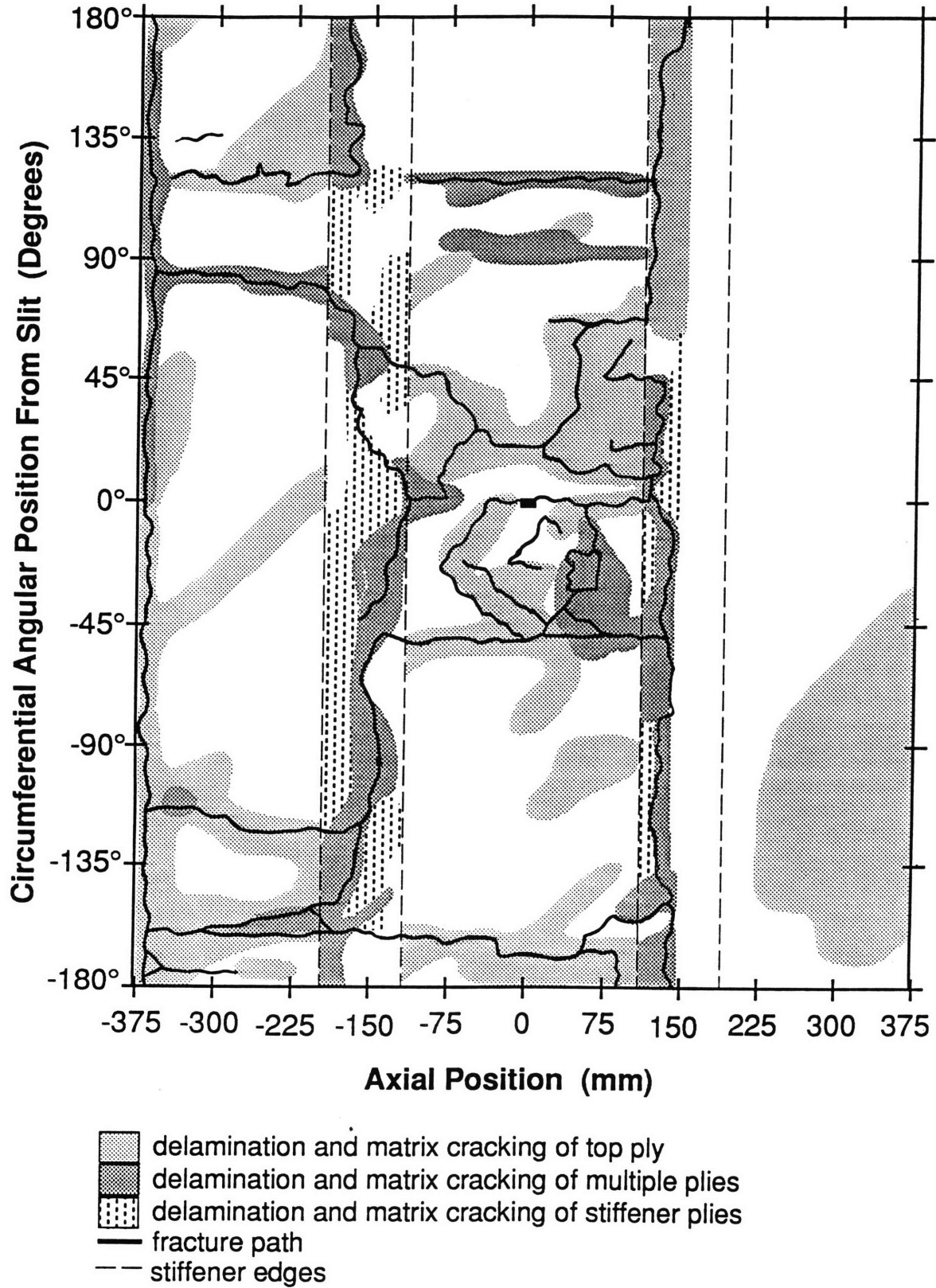
Figure 4.46 Schematic of Fractured [±45/90]ₛ Cylinder with 12.7 mm Slit and 4 Layers of Stiffeners.

4.2.4 [0$_f$/45$_f$]$_s$ Cylinder

The failure pressure of the [0$_f$/45$_f$]$_s$ quasi-isotropic fabric cylinder with the 12.7 mm long slit is graphed with a plate correlation and quasiisotropic shell failure prediction in Figure 4.47. The plate data, acquired in previous work, was found for the same material and layup [29]. The shell correction factor was determined as explained in section 4.2.1. Cylinder data, determined in previous work for larger slit sizes [7], is included, as well, to provide a basis for comparison of the data and predicted results. Unlike the data for the graphite/epoxy tape cylinders with 12.7 mm slits, the failure pressure of the fabric cylinder agreed with the predicted value.

The cylinder, containing a 12.7 mm axial flaw, failed at 2.82 MPa of internal pressure. A photograph of the cylinder, which has no stiffening bands, is shown in Figure 4.48. As shown in the schematic of Figure 4.49, the damage to the cylinder is severe, and the section of the specimen near the original slit is broken into many small pieces. An axial fracture path travelling all the way to the endcap emanates from each end of the slit. Upon reaching the endcaps, these paths bifurcate and turn to 0°, travelling around the cylinder and completely separating the body of the specimen from the endcaps. The two axial fractures at the rear of the tube are due to the constraint of the channel supporting the cylinder. Although the cylinder rests on its endcaps, leaving 15 mm between the channel and the closest part of the laminate, the force at failure causes the cylinder to hit and fracture at the edges of the channel. Additional damage occurs around the slit as other fractures branch from the primary paths at a 0° angle. These paths curve to ±90°, forming small pieces as shown in the schematic in Figure 4.49.
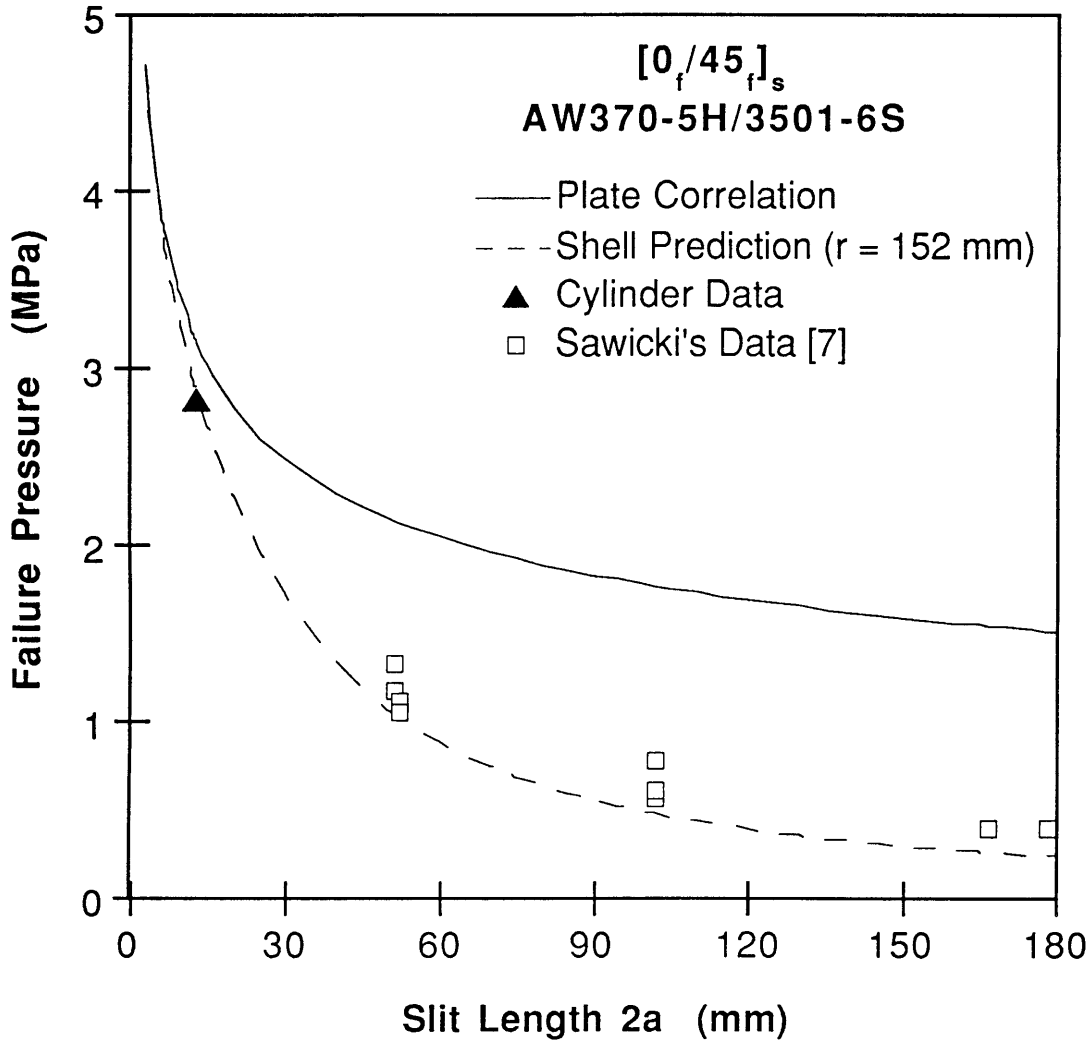
Figure 4.47 [0f/45f]s Cylinder Fracture Pressures and Prediction Curve.
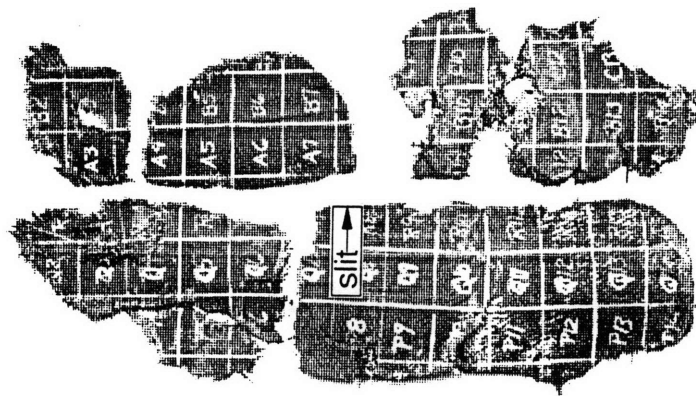
Figure 4.48 Post-Test Photograph of $[0_f/45_f]_s$ Cylinder with 12.7 mm Slit and No Stiffeners.

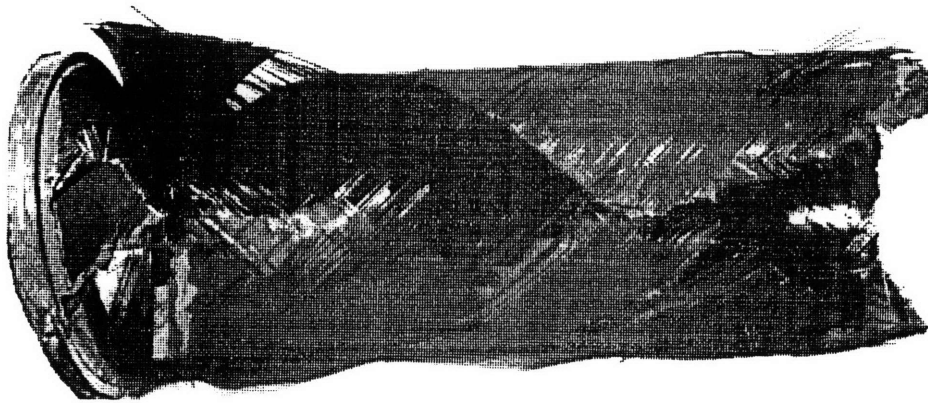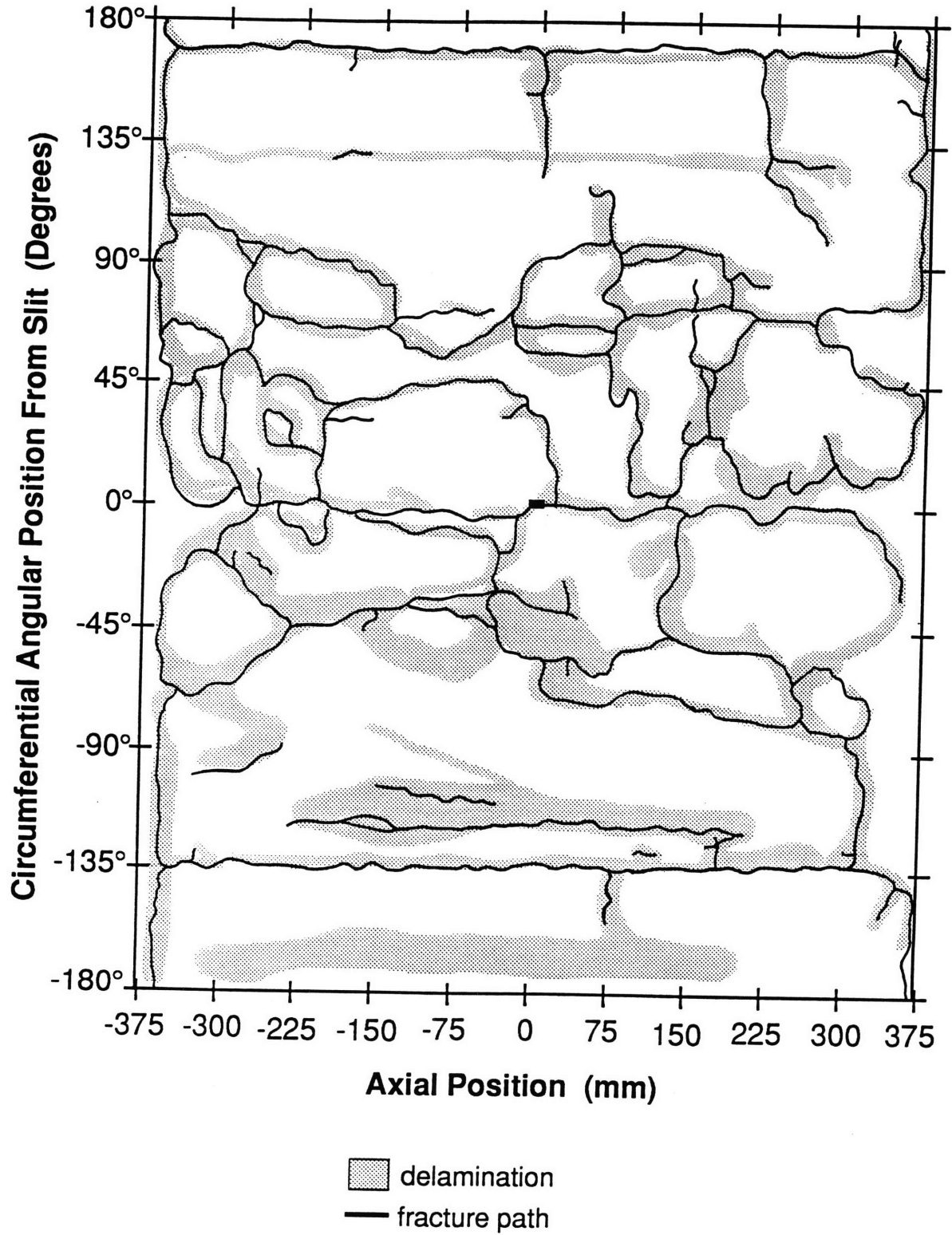Figure 4.49 Schematic of Fractured $[0_f/45_f]_s$ Cylinder with 12.7 mm Slit and No Stiffeners.

CHAPTER 5

Discussion

The purposes of this investigation are twofold. First, the applicability of the existing predictive methodology to quasi-isotropic and structurally anisotropic tape cylinders is examined. The experimental results and the correlation of fracture pressures with predicted values are discussed in Section 5.1. Second, the ability of circumferential stiffening bands to arrest damage in structurally anisotropic tape cylinders is investigated. Fracture propagation and arrest, as well as a simple quantitative measure of stiffener effectiveness, are presented in Section 5.2.

5.1 Fracture

A comparison of experimental cylinder data with predicted fracture pressures reveals two interesting issues. Data from the structurally anisotropic cylinders shows that the fracture pressures of these cylinders are not adequately predicted by the quasi-isotropic or orthotropic methodologies applied in this investigation. Furthermore, the fracture pressures of both the quasi-isotropic and structurally anisotropic graphite/epoxy tape cylinders with 12.7 mm slits are greater than the equivalent stresses for coupons with the same slit sizes. Possible reasons for these two issues are discussed individually.

An overriding assumption of the predictive methodology applied in this investigation is that the initial fracture modes of the cylinders are similar to those for the coupons of the same laminate. It is therefore

necessary to examine and compare the fracture modes of the coupons and cylinders, and to determine what similarities, if any, can be found between the specimen types. It is important to realize that the entire fracture paths of the specimens are not comparable. The cylinder geometry, as well as any added stiffeners, will affect the direction and manner of damage propagation in the shell specimens. Only initial fracture, which occurs in the region around the slit where the stiffeners exert little influence, can be considered for comparative purposes. Therefore, comparisons of plate and cylinder fracture should be restricted to this region which, for the purposes of this investigation, has been limited in the cylinders to 20 mm on any side of the slit.

With the exception of the cylinder with the 12.7 mm slit, the fracture pressures of the [90/0/±45]ₛ cylinders agree well with the values predicted from the correlated coupon data using the quasi-isotropic shell correction. Fracture pressures for the cylinders with the larger slits lie an average of 7% above the predicted curve. Agreement of the predicted results and experimental data indicates that the predictive methodology used in this investigation applies to quasi-isotropic tape as well as fabric cylinders for all but the smallest slit size tested here. The failure pressure of the quasi-isotropic tape cylinder with the 12.7 mm slit, however, is 18% above the predicted isotropic shell value.

Initial fracture paths in the [90/0/±45]ₛ cylinders with larger slit sizes are similar to those found in the notched coupons of the same laminate. Two primary fracture paths originate at the slit ends and travel towards the edges of the specimens at ±45° angles. The bifurcation of the fracture paths, which occurs in the cylinders between 30 and 200 mm from the slit ends, is sufficiently far from the slits that it is not considered to be part of

the initial fracture. Fracture of the $[90/0/\pm45]_s$ cylinder with the 12.7 mm slit, however, differs from that found both in the coupons and in other cylindrical specimens. Three fracture paths originate at the slit ends. While two of these paths travel outward to the endcaps in a manner similar to the paths found in the other specimens, the third travels around the circumference of the cylinder, effectively splitting the 0° ply. The difference in fracture paths indicates that a different initial fracture mode may dominate in the cylinder with the small slit. Since the predictive methodology requires that the fracture modes of the coupon and shell specimens be the same, the methodology is most likely not applicable to the quasi-isotropic tape cylinder with the 12.7 mm slit. Further examination of the fracture modes of quasi-isotropic tape cylinders with small slit sizes is suggested. Since the failure pressure of the quasi-isotropic fabric cylinder with the same 12.7 mm slit size is accurately predicted by the current methodology, the differences between fracture modes of tape and fabric cylinders should be investigated.

Fracture pressures of the structurally anisotropic cylinders do not agree with the predicted quasi-isotropic or orthotropic shell values at any point. Ranging from slightly above the shell predictions for the largest slit size to well above the equivalent coupon pressures for the smallest slit size, the data falls generally between the coupon correlations and shell predictions.

The inability of the isotropic and specially orthotropic shell prediction methods to predict failure of the structurally anisotropic specimens is not unexpected. Reasons for this may include differences in fracture modes of cylinders and coupons as well as the inability of the isotropic and specially

orthotropic predictive methodologies to account for the material behavior unique to the structurally anisotropic specimens.

Initial fracture modes of the structurally anisotropic cylinders differ from those found in the coupons. In the [±45/0]$_s$ notched coupons, two fracture paths oriented at -45° originate at the slit ends and travel outward to the edges of the specimens. Delamination of the external +45° ply accompanies the fracture paths. In contrast, four fracture paths originate at the slit ends in the cylinders of the same laminate. These fracture paths depart from the slit ends at angles varying from 0° to 90°. Little similarity in initital fracture is seen between [±45/0]$_s$ plate and cylindrical specimens, indicating that application of the current predictive methodology to these specimens is likely not justified.

In the [±45/90]$_s$ cylinders and notched coupons, two fracture paths originate at the slit ends. In the coupons, these fracture paths are oriented at -45° angles. Fracture of the 90° fibers occurs cleanly along this -45° line. The damage paths in the cylinders, however, extend in the 90° direction from the slit ends before bifurcating to ±45° between 20 and 200 mm from the slit. Again, there is little similarity in the direction of the initial fracture paths of the [±45/90]$_s$ coupons and cylinders. Application of the predictive methodology to these specimens may therefore not be valid.

It is stressed that the results presented here encompass only one cylinder radius and a finite range of slit sizes. These factors greatly affect the predicted failure pressures calculated from coupon data; however, their effect on experimental specimens is not known. As cylinder radius increases, the curvature of the specimen decreases. In the limit, the curvature is zero and the flat plate is recovered. The existing cylinder data falls both above and below the flat plate data, and a line drawn through the

data points has a steeper slope than does the coupon correlation curve. Failure of structurally anisotropic cylinders with different radii should be investigated to determine if the experimental data approaches the flat plate values as radius increases. Work of this nature would indicate if the slope of the experimental data decreases with curvature, and if there is a single slit size below which all cylinder failures occur at higher pressures than do the corresponding coupon fractures. Both experimental and analytic work is indicated.

For large slit sizes, the failure pressures determined in this investigation fall closer to the values predicted by the isotropic and specially orthotropic shell predictions. It is not known if these curves are an asymptote for the failure pressures of the structurally anisotropic cylinders, or if the pressures will continue to decrease below the isotropic prediction curve. Experimental and analytic data for structurally anisotropic cylinders with larger slit sizes should be found to determine the existence of such an asymptote.

The applicability of the predictive methodology to these cylinders may be further hampered because properties unique to the structurally anisotropic laminates are neglected. Among these properties is the bending-twisting coupling exhibited by the $[\pm 45/0]_s$ and $[\pm 45/90]_s$ cylinders. The effect of this coupling, which does not affect the uniaxial tensile coupons due to the lack of bending, is not incorporated into the predictive methodology. Extension-extension coupling, expressed for an isotropic material in terms of the Poisson's ratio, cannot be as concisely described for a structurally anisotropic material since both major and minor Poisson's ratios exist. Although large changes in the average of the Poisson's ratios, used in this investigation, do not significantly affect the prediction results,

the use of this value alone cannot accurately reflect the laminate behavior. Analysis of the laminate behavior in the cylindrical geometry should be conducted to determine the effects of both types of coupling.

The most broad assumption made in applying the predictive methodology to any cylinder is that the axial loading of the cylinder does not affect the fracture pressure of the specimen. For quasi-isotropic cylinders, this assumption seems valid due to the reasons previously discussed. However, the axial loading may have more effect on the stresses at the slit end in structurally anisotropic cylinders through the coupling mechanisms described above. Furthermore, whereas splitting cannot occur in the fabric cases, it can occur in the tape cylinders. This may also make the axial load more important. Analysis is necessary to determine the effects of these factors on the failure pressures of biaxially-loaded structurally anisotropic cylinders.

All graphite/epoxy tape cylinders with 12.7 mm slits fractured at pressures higher than both the predicted shell values and the equivalent coupon pressures. The quasi-isotropic fabric cylinder with the same slit size, however, matched the predicted shell value. It is important to identify possible explanations for this special case. Work by Harris and Morris [38] on a series of center-cracked tape laminates in uniaxial tension indicates that damage in the region adjacent to a notch tip can relieve the local stresses in some laminate types. The mitigation of stress is accomplished via local damage to the laminate. In particular, axial fractures in 0° plies accompanied by delamination are quite effective in mitigating stress since the specimen is divided into sections with and without notches. Examination of the $[90/0/\pm45]_s$ cylinder with the 12.7 mm slit shows that a circumferential fracture originates at the slit end. This fracture may

indicate the development of a split in the 0° ply which reduced the local stress state, resulting in a higher specimen failure pressure. This stress mitigation does not occur in the quasi-isotropic fabric cylinder with the same slit size as axial splitting is limited by the woven nature of the fabric. The cited investigation does not indicate that stress mitigation occurs in uniaxially-tensioned [±45/0]$_s$ specimens. However, it is possible that the biaxial loading of the pressurized cylinders induces similar damage in the laminates tested here. No data is available for [±45/90]$_s$ laminates.

It is clear from the results of this investigation that the available information is insufficient to describe the behavior of tape cylindrical specimens, epecially those which are structurally anisotropic. Based on coupon data, the predictive methodology applied here does not accurately forecast the failure pressures of these cylinders. A key to the applicability of this methodology lies in the similarity of coupon and cylinder failure mechanisms. If these are different for the two specimen geometries, the methodology does not yield accurate results. The fracture mechanisms of the tape cylinder, particularly of the structurally anisotropic laminates, should be investigated to determine the factors affecting stresses at the slit. Detailed stress analysis of laminate behavior incorporating specimen geometry, complete loading conditions, material and laminate properties, and slit size should be conducted.

5.2. Notch Propagation and Damage Arrest

The purpose of this section is mainly to examine qualitatively the effect of stiffening bands on the propagation and arrest of damage initiating at a notch. Factors included in this discussion are the direction and extent

of notch propagation, the severity of damage to the cylinder, and the ability of the stiffeners to contain damage. Damage is presented first with respect to slit size, and then with respect to number of stiffeners. Finally, a qualitative factor correlating the severity of the damage with the slit length and stiffener properties is presented.

Severity of damage to a cylinder which has ruptured due to fracture initiating at a slit is defined here as a combination of factors. These factors include the amount of surface area of the cylinder through which damage paths have propagated, the size and number of the remaining fragments, and the amount of delamination and matrix cracking apparent on the cylinder surface. Essentially a quantitative measure, this term is used not to judge the fractures absolutely, but to rank the cylinders of a laminate type relative to one another.

Severity of damage decreases with slit size for all cylinders. As slit size decreases, more force in the form of internal pressure is required to produce the same local stresses. Regardless of number of stiffeners, the fractures of the specimens with the smallest slit sizes are most severe. Numerous damage paths traverse the laminates, fracturing them into many small fragments and causing widespread delamination of the surface plies. The slit size can therefore be used as an inverse measure of the energy which must be dissipated in the fracture and pressure release processes. More energy, provided by the internal pressure, is available to promote fracture propagation in the cylinders with small slits; consequently, more damage occurs. Any measure of damage propagation in a laminate must include a factor accounting for the available energy.

In all cases investigated here, the presence of stiffeners drastically affects the direction of propagation of the fracture paths after initial

fracture occurs. It is again stressed that the initial fractures of the cylinders, originating at the slit tips, are not affected by the presence of the stiffening bands. Discussions and comparisons of fracture paths presented previously support this statement. In the cylinders without stiffeners, namely all [90/0/±45]$_s$ specimens, the [±45/0]$_s$ cylinder with the 25.4 mm slit, and the [±45/90]$_s$ specimens with 25.4 and 38.1 mm slits, the fractures propagate all the way to the endcaps. When any stiffeners are added, the direction of fracture propagation is noticeably altered. While not all paths are permanently redirected to 0°, the stiffeners do cause fracture paths to travel further circumferentially and less in the axial direction than those in the unstiffened cylinders. The ability of the stiffeners to turn the slits abruptly to 0° seems to depend on the thickness of the stiffener layer.

Circumferential stiffening bands are thought to affect the direction of fracture propagation by lowering circumferential strains in the laminate [7]. Thicker layers of stiffeners, which are more resistant to the bending which occurs as the damage propagates, thus further lower the local circumferential strains. The ratio of bending stiffnesses of the stiffened to unstiffened regions of the cylinder can therefore be used as a measure of the effectiveness of a stiffener in containing fracture.

A quantitative method of evaluating stiffener effectiveness in containing or turning damage paths must therefore include both measures of slit size or failure pressure and of bending stiffness. A laminate-specific containment ratio, C, dependent upon these measures is proposed:

$$C = \frac{D_s}{D_u} \left(\frac{2a}{r} \right) \tag{5.1}$$

This non-dimensional containment factor is dependent upon the ratio of the circumferential bending stiffness of the stiffened regions, D_s, to that of the unstiffened base laminate, D_u. The slit length, 2a, is non-dimensionalized by the cylinder radius, r, thus incorporating the effects of specimen curvature. The value of the containment ratio increases with likelihood of turning or containing damage originating at a slit end between the set of stiffeners. As the radius of a cylinder approaches infinity and the specimen approximates a flat plate, the value of the containment ratio approaches zero. Work by Sawicki [7], which shows that stiffeners have no effect on the direction of notch propagation in flat plates, supports the use of the radius, r, in the denominator of the containment ratio.

Values of the containment ratios are compared with qualitative estimations of the state of cylinder damage and effectiveness of stiffeners in redirecting fracture paths in the circumferential direction. For the purposes of this investigation, the damage of the cylinders is described in terms of three words: 'through', 'turned', or 'into'. These words correspond to the extent of the fracture paths relative to the stiffener locations. 'Through' indicates that at least one fracture path has extended entirely through the stiffening band, or in the case of unstiffened cylinders, all the way to the endcaps. 'Into' indicates that a fracture path has travelled at least partway into the stiffened region, and 'turned' indicates that the fracture path has been turned to 0° at the inside edge or within the width the stiffener. More than one term may apply to each cylinder. However, a direct comparison of containment ratio values and schematics of the individual stiffener damage states may be more enlightening.

Values of the containment ratios for the individual cylinders are presented with the qualitative descriptions in Tables 5.1 and 5.2. With the

Table 5.1 Qualitative and Quantitative Fracture Assessment of [±45/0]$_s$ Cylinders

Slit Size [mm]	Number of Stiffener Layers	Containment Ratio	Qualitative Fracture Description
12.7	4	1.50	through
25.4	0	0.17	through
38.1	4	4.49	turned
50.8	2	2.09	into/turned
63.5	2	2.61	through/turned[a]

[a] fracture extends through the stiffeners but turns before reaching the endcaps

Table 5.2 Qualitative and Quantitative Fracture Assessment of [±45/90]$_s$
Cylinders

Slit Size [mm]	Number of Stiffener Layers	Containment Ratio	Qualitative Fracture Description
12.7	4	1.65	through/turned
25.4	0	0.17	through
38.1	0	0.25	through
50.8	4	6.62	into/turned
63.5	2	2.85	through/turned

exception of the [±45/0]$_s$ cylinder with two stiffeners and a 63.5 mm slit, the qualitative and quantitative measures of cylinder damage correlate within each laminate type. These three words, however, are insufficient to describe the damage to each cylinder. The containment ratios reflect the gradations in ability of stiffeners to redirect damage much more accurately.

A comparison of fracture descriptions and containment ratios follows. The highest containment ratio value for the [±45/0]$_s$ cylinders is 4.49, determined for the cylinder with a 38.1 mm slit and four layers of stiffening bands. The damage is qualified as 'turned'. No fracture paths or delamination damage extend beyond the inside edge of the stiffening bands, and the fracture is entirely contained by the stiffeners. The containment value for the [±45/0]$_s$ cylinder with a slit length of 50.8 mm and two layers of stiffeners is 2.09. At its furthest extent, the 'into/turned' fracture travels roughly one-third of the way into one of the stiffening bands before turning. The [±45/0]$_s$ specimen with a 12.7 mm long slit and four layers of stiffeners has a containment ratio of 1.50. Although the stiffening bands do turn the direction of fracture propagation, they are unable to contain any of the four fracture paths emanating from the slit. The cylinder with the 25.4 mm slit has a low containment ratio value of 0.17 because no stiffeners were added to the layup. Fracture extends to the endcaps of the cylinder. The only apparently aberrant data point for the [±45/0]$_s$ cylinders is that of the cylinder with two stiffeners and a 63.5 mm long slit. While the ranking of the 2.61 containment ratio indicates that the damage should be turned and contained within the stiffening bands, the fracture paths extend through the stiffeners. These fractures, however, do turn to travel around the cylinder just outside the stiffened regions, never extending all the way to the endcaps.

A similar comparison can be made for the [±45/90]$_s$ cylinders. The cylinder with a 50.8 mm long slit and four layers of stiffeners has a containment ratio of 6.62. The damage to this cylinder, labelled 'into/turned', is limited for the most part to the center section of the cylinder. All but one fracture path are turned to 0° before entering the stiffened region, and the last travels partway through the bands before turning likewise. The second largest containment ratio, 2.85, is found for the cylinder with two layers of stiffeners and a 63.5 mm slit length. Of the four fracture paths emanating from the slit in this specimen, three travel through the stiffeners to the endcaps while the remaining path turns abruptly to 0° at the stiffener. Of the three paths that extend through the stiffening bands, two turn first to 0° before continuing axially outward to the endcaps. As with the previous cylinder, the fracture paths do not branch and the cylinder fragments are few in number. The damage is qualified as 'through/turned'. The last of the [±45/90]$_s$ cylinders with stiffening bands, assigned a containment ratio of 1.65, is that with the 12.7 mm slit and four layers of stiffeners. The fracture, described as 'through/turned', extends through the stiffener on one side of the slit. Damage on this side of the cylinder is quite extensive. Multiple fracture paths, delamination of the stiffener plies and base laminate delamination are visible at and outside the stiffening band. Fracture on the other side of the slit extends into the stiffener before turning to the 0° direction. However, delamination of the base laminate is visible outside the stiffener on this side as well. The remaining two [±45/90]$_s$ cylinders have no stiffening bands, and consequently the values of the containment ratio are low for these specimens. In both of the cylinders, which contain 25.4 and 38.1 mm long slits, fracture extends to the endcaps.

The containment values generally correlate with the extent of damage to the cylinder which propagates through the stiffening bands. It is important to note that the correlations are laminate specific. The applicability of this containment ratio to other cylinder types is untested. Present work is limited to 152 mm radius structurally anisotropic tape cylinders with 5 different slit sizes. Applicability of the ratio has been determined for one cylinder radius and laminate thickness only. It is not known what effect variation of the specimen geometry will have on the applicability of the containment ratio to categorize fracture. An increase in cylinder radius, which, for the same slit size, reduces the failure pressure of a cylinder, may result in less severe damage. However, that same increase in radius will yield a lower containment ratio, indicating that a larger cylinder is more susceptible to damage. Thus, the containment ratio may be specific to cylinder size. Experimental work to determine the extent of the applicability of the containment ratio to stiffened cylinders of other radii is suggested .

Furthermore, the investigation conducted here is limited to a small set of slit sizes. The containment ratio increases with the slit size. While use of this relation in the containment ratio has been experimentally validated for the specimens tested here, it may not be applicable for a different range of slit sizes.

Changes in laminate properties other than bending stiffness may affect the generality of the containment ratios as well. The individual bending stiffnesses of the stiffened and unstiffened regions, as well as their ratios, are similar for the $[\pm 45/0]_s$ and $[\pm 45/90]_s$ laminates investigated here. This results in containment ratios which are of the same orders of magnitude for both specimen groups. However, the extent of damage

through the stiffeners is not comparable for a $[\pm 45/0]_s$ and a $[\pm 45/90]_s$ cylinder with the same containment ratio. The quantative ranking of damage severity thus appears to be laminate-specific.

CHAPTER 6

Conclusions and Recommendations

The conclusions and recommendations presented in this chapter are a result of the experimental work and subsequent analysis conducted in the course of this investigation and presented in the previous chapters.

6.1 Conclusions

1. The failure pressures of the $[90/0/\pm45]_s$ cylinders with axial slits ranging from 25.4 to 63.5 mm in length agree with the results of the current predictive methodology, which utilizes the isotropic shell correction factor.

2. The predictive methodology used in this investigation accurately determines the failure pressure of the $[0_f/45_f]_s$ fabric cylinder with the 12.7 mm long slit, but is unable to predict failure of the $[90/0/\pm45]_s$ tape cylinder with the same slit size. The initial fracture of the tape cylinder is not comparable to the modes found in other cylinders and coupons of the same layup. Stress mitigation at the notch tip due to local damage may be a factor in this case.

3. Failure pressures of the structurally anisotropic $[\pm45/0]_s$ and $[\pm45/90]_s$ tape cylinders with slit sizes ranging from 12.7 to 63.5 mm are not predictable using the current methodology. Laminate properties

such as structural coupling as well as the biaxial loading state, not included in the predictive methodology, may be important factors.

4. Different fracture modes in coupons and cylinders of the same laminate type indicate that the current predictive methodology is not applicable in these cases. Failure pressures of [90/0/±45]$_s$ cylinders in which the fracture modes are similar to those found in coupons are accurately predicted by the coupon-based predictive methodology. In the structurally anisotropic laminates, however, the fracture modes of cylinders and coupons do not match, and the failure predictions do not agree with experimental results.

5. A possible explanation for the high failure pressure of the [90/0/±45]$_s$ quasi-isotropic tape cylinder with the 12.7 mm slit is that axial splitting of the 0° ply, accompanied by local delamination in the region near the slit, reduces the stresses at the notch tip. The presence of a circumferential fracture path originating at the slit tip in the cylinder supports this explanation. Stress mitigation may occur in a similar manner in the structurally anisotropic cylinders.

6. External stiffeners located on either side of a slit generally redirect fracture paths from the axial to the circumferential direction. The amount of redirection depends on the number of stiffeners as well as the internal pressure applied to the cylinder.

7. Ability of the stiffening bands, located on either side of an axial slit, to contain damage depends both on the slit size and the number of

stiffener layers present in the cylinder. Quantification of this effect
has been attempted via a containment ratio dependent on slit length,
cylinder radius, and the bending stiffnesses of the stiffened and
unstiffened regions. The containment ratio successfully ranks the
structurally anisotropic cylinders according to the amount of damage
extending through the stiffeners.

6.2 Recommendations

1. Both quasi-isotropic and structurally anisotropic tape cylinders with
    small slits should be examined to determine if stress-mitigating
    damage occurs at the slit tips under high pressures. Sub-failure
    pressurization of the cylinders and subsequent evaluation of damage
    in the region around the slit via x-ray or ultrasonic scan should be
    conducted to determine what types of damage, if any, occur.

2. Stress analysis of the structurally anisotropic cylinders should be
    conducted to determine the local stresses and fracture modes at the
    slit tip. Analysis should include the bending-twisting and extension-
    extension coupling terms and the biaxial loading of the cylinder.
    Factors causing the structurally anisotropic cylinders to fracture
    differently from the coupons should be identified from this analysis.

3. Effects of changes in cylinder radius on the failure pressures of
    structurally anisotropic cylinders should be investigated.
    Comparison of the pressures and failure modes with existing

cylinder and coupon data should be conducted to determine trends in laminate behavior.

4. Structurally anisotropic cylinders with larger slit sizes should be tested to determine if the isotropic failure prediction curve is an asymptote for the cylinder failure pressures, or if experimental results continue to decrease below the values predicted for isotropic shells.

5. Effects of cylinder radius on the efficacy of the stiffeners in containing damage should be investigated. Applicability of the containment factor to cylinders of different radii, as well as ability of the factor to rank damage containment regardless of radius could be determined from such results.

6. Effects of a different range of slit sizes on the ability of the stiffening bands to contain damage should be investigated. Results could be used to determine the correctness of using slit size as a measure of damage severity in the containment ratio.

7. Stiffener effects on different laminate types should be investigated to determine the generality of the containment factor. Tests should be conducted with cylinders having different stiffened and unstiffened bending stiffnesses, as well as different ratios of the two. Data would indicate if the containment factor accurately ranks the extent of damage to a cylinder of a different laminate type.

References

1. Graves, M.J., "The Catastrophic Failure of Pressurized Graphite/Epoxy Cylinders," TELAC Report 82-10, Department of Aeronautics and Astronautics, Massachusetts Institute of Technology, Cambridge, MA, September 1982.

2. Chang, S.G. and Mar, J.W., "The Catastrophic Failure of Pressurized Graphite/Epoxy Cylinders Flawed with Slits and Holes," TELAC Report 84-13, Department of Aeronautics and Astronautics, Massachusetts Institute of Technology, March 1984.

3. Graves, M.J., and Lagace, P.A., "Damage Tolerance of Composite Cylinders," *Composite Structures*, Vol. 4, No. 1, 1985, pp. 75-91.

4. Chang, S.G. and Mar, J.W., "The Catastrophic Failure of Pressurized Graphite/Epoxy Cylinders Initiated by Slits at Various Angles," *Journal of Aircraft*, Vol. 22, No. 6, June 1985, pp. 462-466.

5. Lagace, P.A. and Saeger, K.J., "Damage Tolerance Characteristics of Pressurized Graphite/Epoxy Cylinders," Proceedings of the Sixth International Symposium on Offshore Mechanics and Arctic Engineering, ASME, Houston, Texas, March,1987, pp. 31-37.

6. Saeger, K.J., and Lagace, P.A., "Fracture of Pressurized Composite Cylinders with a High Strain-to-Failure Matrix System," *Composite Materials: Fatigue and Fracture, Second Volume, ASTM STP 1012*, American Society of Testing and Materials, Philadelphia, 1989, pp. 326-337.

7. Sawicki, A.J., "Damage Tolerance of Integrally Stiffened Composite Plates and Cylinders," TELAC Report 90-17, Department of Aeronautics and Astronautics, Massachusetts Institute of Technology, Cambridge, MA, September 1990.

8. Awerbach, J., and Madhukar, M.S., "Notched Strength of Composite Laminates Predictions and Experiments- A Review," *Journal of Reinforced Plastics and Composites*, Vol. 4, January 1985, pp. 3-159.

9. Mar, J.W., and Lin, K.Y., "Fracture of Boron/Aluminum Composites with Discontinuities," *Journal of Composite Materials*, October 1977, pp. 405-421.

10. Whitney, J.M., and Nuismer, R.J., "Stress Fracture Criteria for Composite Laminates Containing Stress Concentrations," *Journal of Composite Materials*, Vol. 8, 1974, pp. 253-265.

11. Nuismer, R.J., and Whitney, J.M., "Uniaxial Failure of Composite Materials Containing Stress Concentrations," *Fracture Mechanics of Composites*, ASTM 593, American Society for Testing and Materials, 1975, pp. 117-142.

12. Waddoups, M.E., Eisenmann, J.R., and Kaminski, B.E., "Macroscopic Fracture Mechanics of Advanced Composite Materials," *Journal of Composite Materials*, Vol.5, 1971, pp. 446-454.

13. Cruse, T.A., "Tensile Strength of Notched Composites," *Journal of Composite Materials*, Vol. 7, April 1973, pp. 218-229.

14. Lagace, P.A., "Notch Sensitivity and Stacking Sequence of Laminated Composites," *Composite Materials Testing and Design, ASTM STP 893*, American Society for Testing and Materials, 1986, pp. 161-176.

15. Lagace, P.A., "Notch Sensitivity of Graphite/Epoxy Fabric Laminates," *Composites Science and Technology*, Vol. 26, 1986, pp. 95-117.

16. Mar, J.W., and Lagace, P.A., "Tensile Fracture of Graphite/Epoxy Laminates with Holes," *Advances in Composite Materials*, Proceedings of the Third International Conference on Composite Materials, Paris, August 26-29, 1980, pp. 130-145.

17. Fenner, D.N., "Stress Singularities in Composite Materials with an Arbitrarily Oriented Crack Meeting an Interface," *International Journal of Fracture*, Vol. 12, No. 5, October 1986, pp. 705-721.

18. Mar, J.W., and Lin, K.Y., "Fracture Mechanics Correlation for Tensile Failure of Filament Composites with Holes," *Journal of Aircraft*, Vol. 14, July 1977, pp. 703-704.

19. Brewer, J.C., "Tensile Fracture of Graphite/Epoxy with Angled Slits," TELAC Report 82-16, Department of Aeronautics and Astronautics, Massachusetts Institute of Technology, December 1982.

20. Folias, E.S., "On the Effect of Initial Curvature on Cracked Flat Sheets," *International Journal of Fracture Mechanics*, Vol. 5, No. 4, Noordhoff International, Leiden, the Netherlands, 1969, pp. 327-346.

21. Folias, E.S., "An Axial Crack in a Pressurized Cylindrical Shell," *International Journal of Fracture Mechanics*, Vol.1, No.2, 1965, pp. 104-113.

22. Folias, E.S., "On the Prediction of Catastrophic Failures in Pressurized Vessels," *Prospects of Fracture Mechanics*, Edited by

G.C. Sih, H.C. van Elst, and D. Broek, Nordhoff International, Leiden, the Netherlands, 1974, pp. 405-418.

23. Folias, E.S., "A Finite Line Crack in a Pressurized Spherical Shell," *International Journal of Fracture Mechanics*, Vol.1, No.1, 1965, pp. 20-46.

24. Folias, E.S., "A Circumferential Crack in a Pressurized Cylindrical Shell," *International Journal of Fracture Mechanics*, Vol. 3, No. 1, 1967, pp. 1-11.

25. Krenk, S., "Influence of Transverse Shear on an Axial Crack in a Cylindrical Shell," *International Journal of Fracture*, Vol. 14, No. 2, April 1978, pp. 123-143.

26. Rogers, J.D., "An Investigation of the Damage Tolerance Characteristics of Graphite/Epoxy Pressure Vessels," TELAC Report 81-12, Department of Aeronautics and Astronautics, Massachusetts Institute of Technology, Cambridge, MA, September 1981.

27. Whitney, J.M., "Biaxial Testing of Graphite/Epoxy Composites Containing Stress Concentrations - Part II," Technical Report AFML-TR-76-244, Part II, June 1977.

28. Kageyama, M., "The Effect of Delaminations on the Failure of Pressurized Graphite/Epoxy Cylinders," TELAC Report 86-18, Department of Aeronautics and Astronautics, Massachusetts Institute of Technology, Cambridge, MA, May 1986.

29. Ranniger, C., "Effect of Cylinder Diameter on the Damage Tolerance of Graphite/Epoxy Cylinders with Axial Notches," TELAC Report 91-10, Department of Aeronautics and Astronautics, Massachusetts Institute of Technology, Cambridge, MA, May 1991.

30. Emery, A.F., Love, W.J., and Kobayashi, A.S., "Elastic Crack Propagation Along a Pressurized Pipe," *Journal of Pressure Vessel Technology*, Vol. 98, no.1, February 1976, pp. 2-7.

31. McGuire, P.A., Sampath, S.G., Popelar, C.H., and Kanninen, M.F., "A Theoretical Model for Crack Propagation and Crack Arrest in Pressurized pipelines," *Crack Arrest Methodology and Applications*, *ASTM STP 711*, American Society for Testing and Materials, 1980, pp. 341-357.

32. Jozavi, H., Dupuis, C.W., and Sancaktar, E., "An Investigation of the Fracture Behavior of a Composite Crack Arrestor," *Journal of Composite Materials*, Vol. 22, No.5, May 1988, pp. 427-446.

33. Kanninen, M., Mills, E., Hahn, G. et al, "A Study of Ship Hull Crack Arrester Systems," Technical Report SSC-265, Naval Systems Command, Department of the Navy, 1976.

34. Bhatia, N.M. and Verette, R.M., "Crack Arrest of Laminated Composites," *Fracture Mechanics of Composites, ASTM STP 593*, American Society for Testing and Materials, 1975, pp. 200-214.

35. Sendeckyj, G.P., "Concepts for Crack Arrestment in Composites," *Fracture Mechanics of Composites, ASTM STP 593*, American Society for Testing and Materials, 1975, pp. 215-226.

36. Lagace, P.A., Brewer, J.C., and Varnerin, C.F., "TELAC Manufacturing Course Class Notes," TELAC Report 88-4, Department of Aeronautics and Astronautics, Massachusetts Institute of Technology, Cambridge, MA, May 1988.

37. Ranniger, C., and Forbes, K. "Air Bladder Manufacturing Process for Cylindrical Graphite/Epoxy Pressure Vessels," Internal TELAC Document, Department of Aeronautics and Astronautics, Massachusetts Institute of Technology, Cambridge, MA, October 1990.

38. Harris, C.E., and Morris, D.H., "A Fractographic Investigation of the Influence of Stacking Sequence on the Strength of Notched Laminated Composites," *Fractography of Modern Engineering Materials: Composites and Metals, ASTM STP 948*, American Society of Testing and Materials, 1987, pp. 154-173.

Appendix A

Table A.1 [90/0/±45]$_s$ Coupon Parameters

Slit Length [mm]	Average Width [mm]	Average Thickness [mm]	Failure Stress [MPa]	H$_c$ [MPa*mm^m]
0.0	70.3	1.10	697	--
0.0	68.6	1.06	582	--
0.0	66.2	1.05	584	--
9.5	70.4	1.08	319	600
9.5	70.5	1.11	342	643
9.5	70.2	1.11	355	667
9.5	70.3	1.10	352	662
12.7	70.5	1.09	334	680
12.7	70.5	1.11	339	691
12.7	70.3	1.09	330	672
12.7	70.3	1.11	332	676
15.9	70.5	1.09	326	707
15.9	70.5	1.12	310	672
15.9	70.3	1.11	312	677
15.9	70.3	1.10	307	666
19.1	70.5	1.09	300	685
19.1	70.3	1.09	267	609
19.1	70.3	1.09	293	669
19.1	70.3	1.10	285	650

Table A.2 [±45/0]$_s$ Coupon Parameters

Slit Length [mm]	Average Width [mm]	Average Thickness [mm]	Failure Stress [MPa]	H$_c$ [MPa*mm^m]
0.0	70.2	0.84	679	--
0.0	70.1	0.84	604	--
0.0	70.1	0.83	662	--
0.0	70.1	0.83	870	--
0.0	70.0	0.83	678	--
0.0	70.0	0.84	856	--
0.0	70.1	0.82	796	--
0.0	70.1	0.83	802	--
9.5	70.1	0.83	386	726
10.3	70.0	0.84	411	790
10.3	70.0	0.85	373	716
11.1	70.1	0.85	399	783
12.7	70.1	0.85	354	721
14.3	70.0	0.85	353	719
13.5	70.1	0.84	325	684
12.7	70.1	0.83	344	713
15.9	70.1	0.84	320	694
15.9	70.0	0.84	324	703
16.7	70.1	0.82	281	618
16.7	70.1	0.82	320	704
19.1	70.0	0.85	329	751
19.1	70.1	0.86	322	735
19.8	70.0	0.84	300	693
19.8	70.0	0.84	300	693

Table A.3 [±45/90]ₛ Coupon Parameters

Slit Length [mm]	Average Width [mm]	Average Thickness [mm]	Failure Stress [MPa]	H_c [MPa*mm^m]
0.0	70.4	0.86	241	--
0.0	70.2	0.84	224	--
0.0	70.3	0.86	229	--
0.0	70.4	0.84	215	--
0.0	70.4	0.85	216	--
0.0	70.3	0.87	217	--
0.0	70.4	0.85	229	--
0.0	70.4	0.82	224	--
9.5	70.3	0.86	208	391
10.3	70.4	0.88	226	425
9.5	70.4	0.84	219	412
9.5	70.4	0.85	217	417
13.5	70.2	0.87	200	407
13.5	70.4	0.85	195	397
12.7	70.1	0.86	214	443
12.7	70.4	0.83	210	435
15.9	70.4	0.83	202	432
15.1	70.3	0.84	206	447
15.9	70.0	0.85	194	421
15.9	70.2	0.86	187	406
19.1	70.0	0.85	198	452
19.1	70.3	0.84	181	413
19.1	70.2	0.84	187	427

Table A.4 Nominal and Average Cylinder Thicknesses

Laminate	Slit Size [mm]	Nominal Thickness [mm]	Average Thickness [mm]
[±45/90]$_s$	63.5	0.804	0.88
	50.8		0.91
	38.1		0.86
	25.4		*
	12.7		0.82
[±45/0]$_s$	63.5	0.804	0.85
	50.8		0.88
	38.1		0.88
	25.4		0.84
	12.7		0.82
[90/0/±45]$_s$	50.8	1.07	1.08
	38.1		1.09
	25.4		1.09
	12.7		1.10
[0$_f$/45$_f$]$_s$	12.7	1.40	--[a]

[a]thickness not measured

Table A.5 Unnotched [90/0/±45]$_s$ Coupon Stiffness Data

Fracture Stress [MPa]	Longitudinal Modulus [GPa]	Major Poisson's Ratio
584	50.1	0.28
582	-- [a]	-- [a]
697	54.5	0.31

[a] strain data lost during test

Table A.6 Unnotched [±45/0]ₛ Coupon Stiffness Data

Fracture Stress [MPa]	Longitudinal Modulus [GPa]	Major Poisson's Ratio
679	58.5	0.73
604	58.1	0.71
662	63.5	0.67
870	62.1	0.62
678	63.1	0.72
856	61.1	0.70
796	60.2	0.70
802	65.3	0.69

Table A.7 Unnotched [±45/90]ₛ Coupon Stiffness Data

Fracture Stress [MPa]	Longitudinal Modulus [GPa]	Major Poisson's Ratio
241	27.0	0.29
224	25.9	0.27
229	26.5	0.25
215	28.0	0.30
216	27.3	0.31
217	27.5	0.30
229	26.5	0.32
224	26.4	0.29